# *In vivo* Longitudinal Changes in Lamina Cribrosa Microarchitecture and Optic Nerve Head Structure in Experimental Glaucoma

By

Kevin M. Ivers, B.S.

DISSERTATION

In partial satisfaction of the requirements for the degree of

DOCTOR OF PHILOSOPHY

in

PHYSIOLOGICAL OPTICS

Presented to the

Graduate Faculty

of the

College of Optometry
University of Houston

May 2014

Approved:

_____
Jason Porter, Ph.D. (Chair)

_____
J. Crawford Downs, Ph.D.

_____
Ronald S. Harwerth, O.D., Ph.D.

_____
Michael Twa, O.D., Ph.D.

## Dedication

To my family and Steven

## Acknowledgements

The years I have spent as a graduate student at the University of Houston College of Optometry have been the best years of my life. I have grown both personally and professionally and I have several to thank for this achievement.

First, I would like to thank my loved ones: my Mom, Dad, sisters Ashley and Lindsey, my brother Steven, and my partner in life, Renus. Each and every one of these people has kept my head above water, so to speak, during this long and arduous experience and I am so thankful to have had them in my life. A special thanks goes to my identical twin brother, Steven, who I regard as the greatest inspiration in my life. Thank you, Steven, for your support during all of these years. It means the world.

Second, I have to thank Dr. Laura Frishman, who started me on this journey so many years ago. I was a young undergraduate student in 2006 with an itch to do research during the summer after my sophomore year of studying Biomedical Engineering at the University of Houston. Laura was kind enough to allow me to work in her laboratory for a year, where I first learned what conducting research truly meant. She opened my eyes to a future career in science and research that I am excited to embark upon now. The dedication put forth by Laura to each and every graduate student is awe-inspiring and I am honored to call her my first mentor in science.

Third, my biggest and most heartfelt thanks goes to my mentor of seven years, Jason Porter. I first saw Jason speak at a conference at the University of Houston in 2007 and was immediately drawn to his research. His way of presenting his work and teaching to the field is the best I have seen. It is no wonder that he is consistently regarded as a favorite professor in many conversations I have had with Optometry students. His patience, his enthusiasm for science, and his attention to detail in every aspect of conducting research are outstanding. I was extremely fortunate to stumble

upon Jason and learn from him throughout all of these years. Under his tutelage, he has taught me how to do great science, a skill that is necessary and sometimes lost on many people. I will count myself lucky in my career if I am even half as good a scientist and researcher as Jason.

Last, but not least, I would like to thank everyone else who has helped shape my life and academic career these last several years, including my committee members Crawford Downs, Ron Harwerth, and Michael Twa. Each of them brought forth expertise in their respective fields to my dissertation and I am indebted to their constant support and guidance. I would also like to thank my fellow lab mates (Chaohong Li, Nripun Sredar, Amitabha Bhakta, and Gongpu Lan) and all of my fellow graduate students for the help they provided over the last several years. One graduate student in particular, Diana Lozano, I am proud to call a dear friend and one I will have for a lifetime. Having someone like Diana in the graduate program who was trekking through a similar experience to mine has made my years here so much easier. I am excited for her as she embarks upon the next chapter in her life and I know only great things will come. Finally, many thanks goes to the Optometric Glaucoma Society for funding my William C. Ezell Fellowship in 2012 and 2013. I am so honored and privileged to be considered a part of their community.

I would like to finish by acknowledging that these years have been the most rewarding years of my life. Houston has been my home for the past 27 years and the University of Houston has been my home for the last 10 years. I am grateful for every opportunity I have received and I will spend my life working my hardest to live up to the honors bestowed upon me. Most important of all, The University of Houston College of Optometry has been my second home for the past 7 years and I will miss it dearly. To the future.

# *In vivo* Longitudinal Changes in Lamina Cribrosa Microarchitecture and Optic Nerve Head Structure in Experimental Glaucoma

By

Kevin M. Ivers, B.S.

DISSERTATION

In partial satisfaction of the requirements for the degree of

DOCTOR OF PHILOSOPHY

in

PHYSIOLOGICAL OPTICS

Presented to the

Graduate Faculty

of the

College of Optometry
University of Houston

May 2014

## Abstract

**Purpose:** Glaucoma is the second leading cause of blindness worldwide. Substantial evidence supports the idea that retinal ganglion cell axons are initially damaged at the lamina cribrosa in glaucoma. The goal of this dissertation was to better understand early changes in lamina cribrosa microarchitecture and optic nerve head (ONH) structure in experimental glaucoma (EG) and determine whether these changes occur prior to changes in conventional clinical measures of vision loss.

**Methods:** 1) Images of the anterior lamina cribrosa surface (ALCS) were acquired with an adaptive optics scanning laser ophthalmoscope (AOSLO) in 4 or more imaging sessions in 2 normal rhesus monkey eyes and 3 normal human eyes. Mean ALCS pore area, elongation, and nearest neighbor distance [NND] were quantified in each imaging session and measurement repeatability was assessed. 2) Spectral domain optical coherence tomography (SDOCT) imaging was used to acquire radial B-scan images of the ONH and quantify Bruch's Membrane Opening (BMO) area, mean ALCS depth (ALCSD), and mean minimum rim width (MRW) in 6 normal rhesus monkeys. ALCS pore geometry was quantified globally, within 60° sectors, and in central and peripheral regions from AOSLO images acquired in the same eyes. Inter-eye differences in pore geometry and ONH structure were quantified. 3) SDOCT and AOSLO images of the ONH and ALCS were acquired before and approximately every 2 weeks after inducing unilateral EG in 7 rhesus monkeys. Mean ALCSD, ALCS radius of curvature, and MRW were quantified from SDOCT B-scans. Retinal nerve fiber layer thickness (RNFLT) was quantified from 12° SDOCT circular scans centered on the ONH. Mean pore geometry was quantified globally, sectorally, and regionally in 3D transformed AOSLO images. Longitudinal changes in ONH structure, ALCS pore geometry, and RNFLT were

examined. 4) Finally, functional measures of vision loss [multifocal electroretinogram (mfERG) and standard automated perimetry (SAP)] were also recorded longitudinally in 3 EG monkeys. Onsets of mfERG-measured reductions in the multifocal photopic negative response (mfPhNR) and SAP-measured losses in visual field sensitivity were compared to onsets of change in ONH and ALCS parameters.

**Results:** 1) Pore areas ranged from 90 to 4,365 $\mu m^2$ across monkeys and 154 to 6,637 $\mu m^2$ across humans. Intersession variability in measuring pore geometry was small in normal monkey and human eyes: 6.1% and 8.3% for pore area, 6.7% and 7.7% for pore elongation, and 5.2% and 4.1% for pore NND, respectively ($P$>.05). 2) Mean differences in BMO area, ALCSD, and MRW between fellow, normal eyes were small: 0.07 ± 0.05 $mm^2$, 10.0 ± 6.9 µm, and 7.9 ± 6.7 µm, respectively ($P$>.05). Inter-eye differences in mean global pore area, elongation, and NND were not significant in 4/6 monkeys, 6/6 monkeys, and 3/6 monkeys, respectively ($P$>.05). Inter-eye differences in mean pore area and NND were measured between superotemporal sectors in 2 monkeys and temporal sectors in 2 monkeys ($P$<.05). 3) Mean ALCSD was the first parameter to change in 6/7 EG eyes. Mean MRW changed first in one EG eye. RNFLT changed last in 5/7 EG eyes. Changes in mean global and local pore geometry were the first or second changes detected in 4/7 EG eyes. At the first time-point of change in pore geometry, mean pore area increased globally (+24.7%), centrally (+23.6%), peripherally (+29.9%), and temporally (+35.5%) ($P$<.05). Mean pore NND increased globally (+13.3%) and in all sectors and regions (mean of +16.1%) ($P$<.05), except inferotemporally. Local changes in pore parameters were measured prior to a global change in the same parameter in 3 monkeys. 4) Mean ALCSD was the first significant structural or functional change in 2/3 EG eyes, while a reduction in mfPhNR amplitude was measured first in 1 EG eye. mfPhNR amplitude changed prior to laminar pore

microarchitecture in 2/3 EG eyes, while simultaneous changes in these parameters occurred in 1 EG eye. RNFLT and visual field sensitivity were the last parameters to initially change in all monkeys.

**Conclusions:** Structural changes in ALCS position (mean ALCSD) and microarchitecture occurred prior to significant losses in RNFLT suggesting early laminar remodeling in response to chronically elevated intraocular pressure in experimental glaucoma. AOSLO and SDOCT structural imaging and mfERG functional recording provide the opportunity to earlier detect glaucomatous damage than current clinical tests.

## Table of Contents

## List of Figures

## List of Tables

# CHAPTER 1

## General Introduction

## 1.1 Introduction

Glaucoma is a complex group of eye diseases that results in the death of retinal ganglion cells (RGCs), the degeneration of their axons, and irreversible losses in vision. It is currently the second leading cause of blindness worldwide (Quigley & Broman, 2006). A large body of work has implicated the lamina cribrosa in the optic nerve head (ONH) as the initial site of damage to RGC axons in glaucoma (Bellezza et al, 2003; Burgoyne et al, 2004; Gaasterland et al, 1978; Minckler et al, 1977; Quigley et al, 1981; Quigley & Green, 1979). The work in this dissertation begins by quantifying the reproducibility of measuring lamina cribrosa microarchitecture *in vivo* in normal human and non-human primates using an adaptive optics scanning laser ophthalmoscope (AOSLO) (Ivers et al, 2011). Next, the dissertation examines the inter-eye differences in lamina cribrosa and ONH structure *in vivo* in normal non-human primates, followed by a longitudinal characterization of changes in anterior lamina cribrosa microarchitecture, ONH structure, and retinal nerve fiber layer (RNFL) thickness *in vivo* in non-human primates with experimental glaucoma. The dissertation concludes with a comparison of structural changes in the ONH and lamina cribrosa microarchitecture with functional measures of vision loss assessed using standard automated perimetry (SAP) and multifocal electroretinography (mfERG) in non-human primates with early experimental glaucoma.

## 1.2 The normal optic nerve head (ONH)

Approximately one million RGC axons exit the retina and pass through the ONH to the lateral geniculate nucleus (LGN) to transmit visual signals to the brain (Balazsi et al, 1984; Jonas et al, 1990; Jonas et al, 1992; Mikelberg et al, 1989; Potts et al, 1972; Sanchez et al, 1986). In humans and non-human primates, there is large variability in the size and shape of the physiologically normal ONH (Quigley et al, 1990; Yang et al,

2009). Quigley et al. calculated a mean optic disc vertical length of 1.87 ± 0.17 mm and horizontal length of 1.76 ± 0.19 mm in 60 adult human donor eyes, with a mean aspect ratio of 1.06 and a mean disc area of 2.58 $mm^2$. In general, the human ONH tends to be more circularly shaped (i.e., an aspect ratio closer to 1) than the monkey ONH. Yang et al. calculated mean optic disc vertical and horizontal lengths of 1.48 ± 94.57 mm and 1.07 ± 67.80 mm, respectively, in 12 eyes of 6 normal monkeys, with a mean aspect ratio of 1.38 ± 0.04 and a mean disc area of 1.25 ± 0.16 $mm^2$ (Yang et al, 2009).

The ONH is primarily composed of the central retinal artery and vein, nerve fiber layer, and the prelaminar, laminar, and retrolaminar regions (Fig. 1-1) (Trivino et al, 1996). The prelaminar region largely consists of columns of glial tissue that surround the RGC axons as they begin to exit the eye. In normal rhesus monkey eyes, the mean thickness and volume of the prelaminar tissue is ~160 µm (range: 95 µm to 193 µm) and 0.23 $mm^3$ (range: 0.17 $mm^3$ to 0.25 $mm^3$), respectively (Yang et al, 2009). Inter-eye percent differences in prelaminar tissue thickness and volume range from 0.5% to 8.9% and 3.8% to 18.1%, respectively, indicating a high degree of symmetry between fellow normal eyes (Yang et al, 2009). After passing through the prelaminar region, axons next pass through the laminar region, which primarily consists of collagenous beams, capillaries, and astrocytes (discussed further in Section 1.3). RGC axons become myelinated in the retrolaminar region and remain myelinated throughout the remainder of the optic nerve (Hayreh, 2011).

Strouthidis et al. were the first to examine ONH structures *in vivo* with optical coherence tomography (OCT) and compare these measurements with the same structures imaged *ex vivo* in the same normal rhesus monkey eye with light microscopy (Strouthidis et al, 2010) (Fig. 1-2). This study marked an important step in being

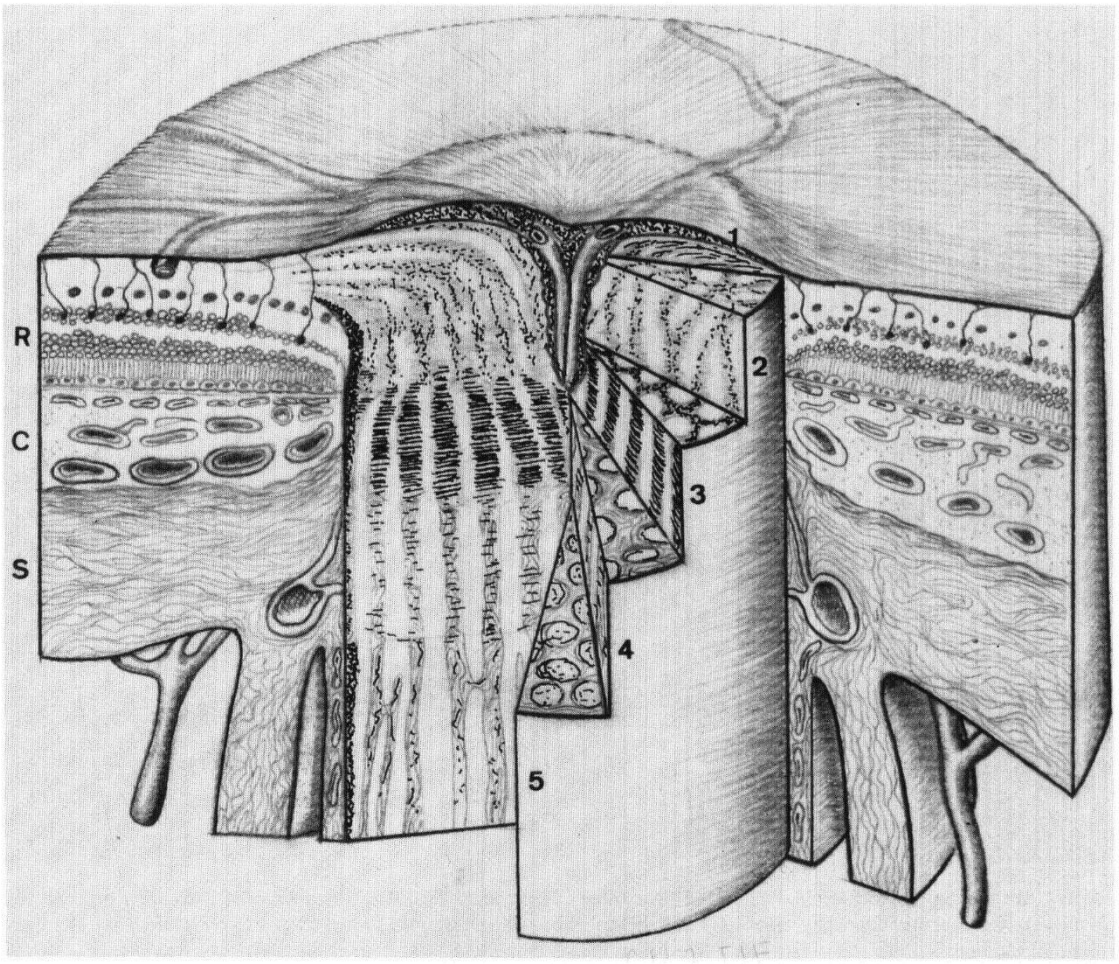


**Figure 1-1.** Cross-section through the ONH that illustrates the pathway of RGC axons through the nerve fiber layer (1), and prelaminar (2 and 3), laminar (4), and retrolaminar (5) regions. R: retina; C: choroid; S: sclera. Reprinted with permission (Trivino et al, 1996).

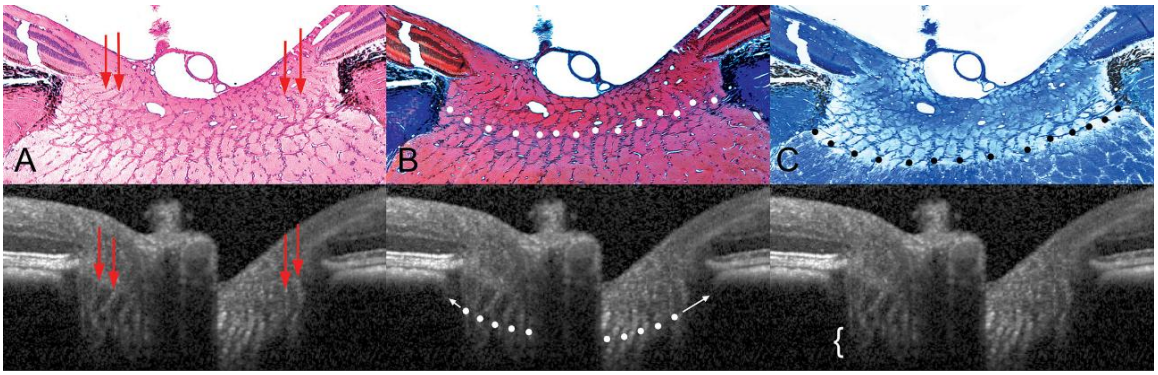


**Figure 1-2.** The anterior lamina cribrosa surface (ALCS) is viewed *ex vivo* with light microscopy (top row) and *in vivo* in the same eye using SDOCT (bottom row). The ALCS is marked with white dots in both the histologic section and the *in vivo* image (b, top and bottom rows), while the posterior lamina cribrosa surface is marked with black dots in the post-mortem image in (c). These results suggest that some ONH structures can be visualized and compared between *in vivo* and post-mortem images from the same eye. Reprinted with permission (Strouthidis et al, 2010).

able to characterize lamina cribrosa structure *in vivo* in normal human and monkey eyes, as well as in glaucomatous human eyes and monkey eyes with experimental glaucoma.

### 1.3 Structure of the normal lamina cribrosa

The lamina cribrosa is a three-dimensional meshwork (or sieve-like structure) that provides structural and functional support to RGC axons as they exit the eye. Kotecha et al. measured a mean lamina cribrosa thickness of 451.3 µm (range: 345.4 µm to 555.9 µm) in 27 human eyes (Kotecha et al, 2006). Yang et al. measured a mean lamina cribrosa thickness of 104 µm (range: 81 µm to 136 µm) in 6 normal monkey eyes (Yang et al, 2009), which is thinner compared to the laminar thickness measured in human eyes. Differences in laminar thickness amongst fellow monkey eyes ranged between 0.7% and 18% (Yang et al, 2009). Additionally, the lamina cribrosa consists of beams and pores through which RGC axons traverse. Laminar beams are largely composed of collagen fibers, contain capillaries, and are lined with astrocytes. Blood flow to the lamina cribrosa is supplied by centripetal branches from the short posterior ciliary arteries. This supply from the ciliary arteries is either by the arterial circle of Zinn and Haller or by direct branches from the short posterior ciliary arteries (Hayreh, 2011) (Fig. 1-3). The laminar capillaries, which deliver oxygen and nutrients to the axons pass through the laminar extracellular matrix (ECM), across surrounding astrocytes, and into peripheral and central axons in each axon bundle (Anderson, 1969). Astrocytes are the primary cell type in the prelaminar and laminar regions (the unmyelinated regions) of the ONH and encase the collagen beams. Astrocytes provide cellular transport functions to the axons and act as the boundary between connective tissue components and the surrounding blood vessels (Hernandez, 2000; Hernandez et al, 2008).

In humans and non-human primates, the lamina cribrosa develops embryologically from central nervous system (CNS)-derived fibroblasts after axons have

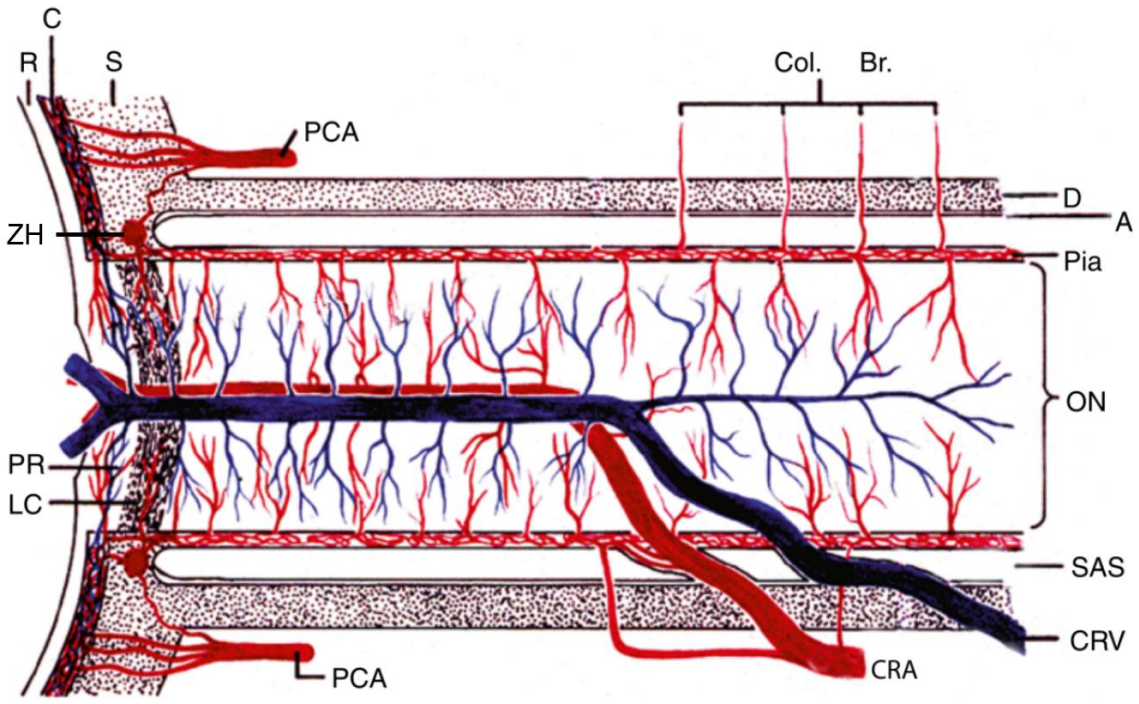


**Figure 1-3.** Blood supply to the ONH. Short posterior ciliary arteries (PCA, red) provide nourishment to the lamina cribrosa (LC). R: retina; S: sclera; C: choroid; CRA: central retinal artery; CRV: central retinal vein; ZH: arterial circle of Zinn and Haller; Col. Br.: collateral branches; D: dura; ON: optic nerve; PR: prelaminar region; A: arachnoid; SAS: subarachnoid space. Reprinted and adapted with permission (Hayreh, 2011).

grown into the ONH (Hernandez & Neufeld, 1991). Collagenization of the lamina cribrosa increases with age and continues into adulthood. Hundreds of axon bundles (mean ± standard error: 550 ± 47 axon bundles), each containing hundreds to thousands of axons, traverse through holes (or pores) in the lamina cribrosa (Ogden et al, 1988). In post-mortem studies, Quigley and Addicks found the normal human lamina to consist of approximately 200-400 pores with diameters that normally range between 10 µm and 100 µm (and some pores with diameters larger than 100 µm) (Quigley & Addicks, 1981). Figure 1-4 illustrates the dramatic change in laminar beams and pores that can take place throughout the depth of the lamina and highlights the fact that pores do not typically extend straight through the lamina. Quigley et al. reported that while some pores pass directly through the lamina, the majority are angled at various degrees and subdivide throughout their course in the lamina (Quigley & Addicks, 1981). Consequently, additional stress from increases in intraocular pressure (IOP) can strain or deform the lamina and directly or indirectly damage axons as they delicately weave their way through this complex laminar structure.

Early studies describing the structure of the lamina cribrosa that were largely carried out in post-mortem eyes of humans and non-human primates found that regional differences in laminar beams and pores exist in normal eyes. Quigley and Addicks found larger amounts of connective tissue in the nasal and temporal sectors of the lamina cribrosa compared to the superior and inferior sectors (Quigley & Addicks, 1981). Additionally, larger amounts of connective tissue were found in the central region of the lamina cribrosa compared to the peripheral region (Quigley & Addicks, 1981). Based on these findings, Quigley and Addicks put forth the notion that the reason the RGC axons that pass through the superior and inferior lamina cribrosa are normally damaged first in glaucoma is potentially due to decreased functional and structural support from a decreased density of connective tissue (or laminar beams) in these regions

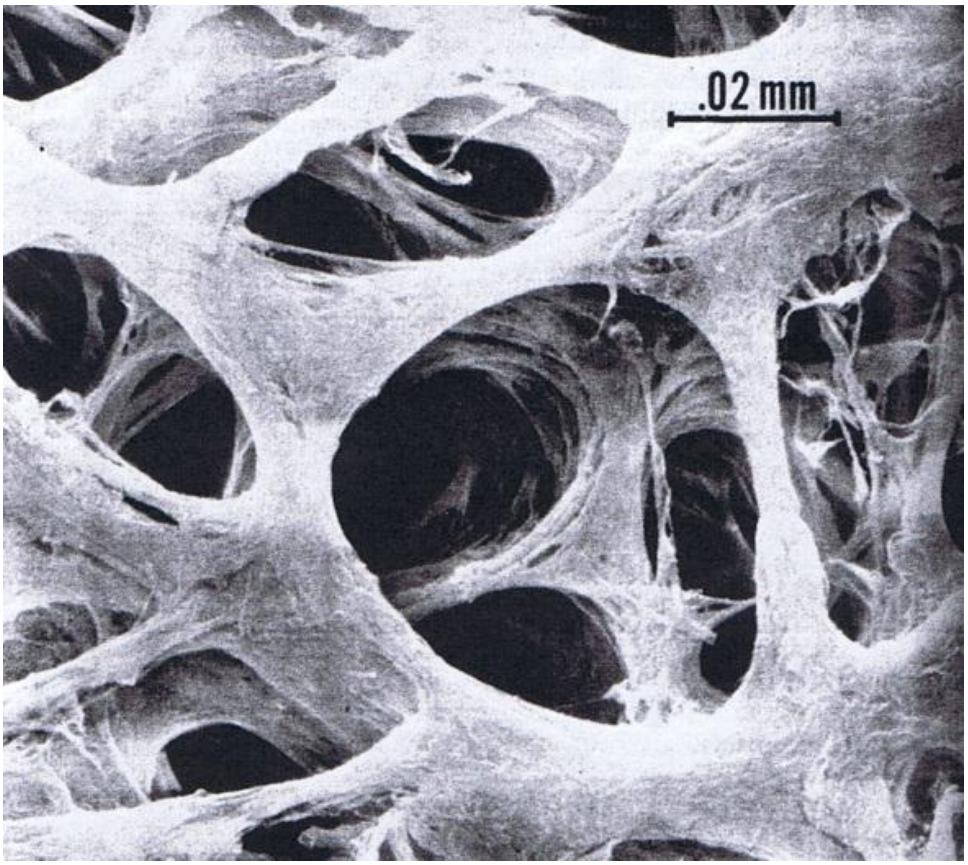


**Figure 1-4.** Representative image of normal laminar beam and pore structure acquired using scanning electron microscopy. As the RGC axons travel further into the lamina, pores branch and create a complex path for axon bundles to traverse as they exit the eye. Reprinted with permission (Emery et al, 1974).

(Quigley & Addicks, 1981). Therefore, increases in IOP could potentially impact these sectors of lower connective tissue density first and result in damage to the corresponding arcuate axons that are typically lost early in glaucoma. In slight contrast to this human data, Roberts et al. found larger amounts of connective tissue in the superior sector and central region of the lamina cribrosa in normal eyes of non-human primates (Roberts et al, 2009).

In conjunction with examining connective tissue characteristics in laminar structure, laminar pore properties have also been investigated in normal eyes. Several studies have shown smaller pores tend to exist in the temporal and nasal sectors (i.e., regions with higher connective tissue density) while larger pores typically predominate in the superior and inferior sectors (i.e., regions with lower connective tissue density) (Dandona et al, 1990; Quigley & Addicks, 1981). Additionally, pores are typically larger in the peripheral lamina (less connective tissue) compared to the central lamina (more connective tissue) (Dandona et al, 1990; Ogden et al, 1988). Similarly, Jonas et al. found that mean pore area was larger in the superior and inferior sectors compared to the temporal sectors and that pore size increased as a function of distance from the ONH center (i.e., larger pores in the periphery) (Jonas et al, 1991). We report pore data from normal eyes in humans and non-human primates in Chapters 2 and 3.

### 1.4 Glaucoma

Glaucoma is often a bilateral and asymmetric disease (i.e., more vision loss in one eye than the other), making it rare for a patient to go blind in both eyes even when no treatment is prescribed (Leske et al, 2001; Mukesh et al, 2002). However, glaucoma is undiagnosed in 90% of affected people worldwide and in 50% of affected people in developed countries (Quigley & Broman, 2006). Therefore, the high prevalence of glaucoma, including primary open angle glaucoma (POAG) and angle-closure glaucoma,

makes it a leading cause of blindness worldwide (second only to cataracts) (Resnikoff et al, 2004). Moreover, these diseases are challenging to study in humans as they slowly progress over months to years (Heijl et al, 2009).

Primary open angle glaucoma and angle-closure glaucoma are characterized clinically by structural abnormalities in the ONH (i.e., changes in cupping and RNFL thickness) and decreased visual function (i.e., perimetry) (Quigley, 2011). The first sign of visual field loss typically occurs in an arcuate area between 5° and 25° from fixation (Aulhorn, 1978), corresponding to a loss of RGC axons that pass through the superior and inferior poles of the ONH. The central and temporal visual fields usually show losses in sensitivity towards the end-stage of disease.

### *1.4.1 Risk factors and treatments*

Major risk factors for glaucoma include elevated intraocular pressure (IOP), age, race/ethnicity, and family history (Giangiacomo & Coleman, 2009). High IOP is often defined clinically as an IOP greater than 21 mmHg, but this number is somewhat arbitrary as patients can develop glaucoma while having “normal” levels of IOP (or normal-tension glaucoma). Conversely, it is also possible for a patient to have a sustained IOP greater than 21 mmHg (ocular hypertension) and never develop glaucoma. As a result, IOP should be continuously monitored in patients with and without glaucoma (Quigley, 2011). The wide range of IOP between patients makes it increasingly difficult to detect and understand the disease processes associated with glaucoma development and progression. In addition, a family history of glaucoma is a risk factor for glaucoma. Having an immediate family member with glaucoma increases one’s chance of acquiring the disease 10-fold (Quigley, 2011). Individuals of African and Hispanic descent also have a higher chance of developing glaucoma compared with those of European or Asian descent (Quigley, 2011; Quigley et al, 2001). Finally, age is

a known risk factor as the mean age of onset is greater than 60 years of age and the frequency of disease increases with increasing age (Leske et al, 2001; Mukesh et al, 2002).

Several therapeutic interventions are currently used to treat glaucoma. The most prevalent approach is to lower IOP using daily eye drops in patients with POAG. Typically, when the pressure is lowered by 20-40%, the progression rate of visual field loss is reduced by a factor of 2 (Quigley, 2011). However, patients with glaucoma use only 60-70% of the doses prescribed by their clinician (Quigley, 2011). Laser treatment of the trabecular meshwork (i.e., trabeculoplasty) is another form of treatment that produces the lowest rate of side-effects. Furthermore, the most common surgical procedure in glaucoma patients is a trabeculectomy which creates a controlled leakage area for the aqueous humour to exit the anterior chamber into a zone in the upper eye over the sclera (called a bleb region). Side effects for this procedure can include bacterial infections and cataract formation (Quigley, 2011). Other surgical procedures (e.g., delivery of an artificial tube-reservoir into the anterior chamber) have side effects that are not optimal for the patient. Earlier disease diagnosis could alleviate the severity of symptoms and allow for less severe treatments that are more manageable (Ederer et al, 2004; Lichter et al, 2001).

### *1.4.2 Early evidence implicating the lamina cribrosa in glaucoma*

The lamina cribrosa has been suggested as the initial site of damage to RGC axons in glaucoma and is likely to be central to the disease process (Bellezza et al, 2003; Burgoyne et al, 2004; Gaasterland et al, 1978; Minckler et al, 1977; Quigley et al, 1981; Quigley & Green, 1979). Early studies showed that an elevation in IOP led to a blockade of axonal transport at the level of the lamina cribrosa in the ONH. Many of these experiments used autoradiography and scintillation counting to track radioactively

labeled proteins (e.g., leucine and proline) as they traveled through RGC axons to the LGN in non-human primates after elevating IOP (Anderson & Hendrickson, 1974; Gaasterland et al, 1978; Lampert, 1967; Minckler et al, 1977; Minckler et al, 1978; Minckler et al, 1976; Quigley & Anderson, 1976). For example, Anderson and Hendrickson found the labeled protein to exist in RGC axons at all locations between the retina and LGN in normal monkeys with normal levels of IOP (Anderson & Hendrickson, 1974). At moderate levels of IOP, axonal transport became obstructed at the level of the lamina cribrosa, although some labeled protein did reach the LGN after approximately 8 hours. At higher levels of IOP, however, there was complete obstruction of axonal transport at the lamina, as no labeled protein reached the LGN (Anderson & Hendrickson, 1974). Minckler et al. found that the axonal transport blockade was most prevalent in the temporal quadrants of the ONH in non-human primates with moderate elevations in IOP (25 to 50 mmHg) (Minckler et al, 1977). Gaasterland noted an increase in axoplasm, dense bodies, and organelles (i.e., mitochondria) in ONHs of non-human primates 3 to 11 weeks after sustained elevations in IOP greater than 20 mmHg (Gaasterland et al, 1978). Consequently, multiple investigators believed that the primary cause of axonal damage in non-human primates with experimental glaucoma and chronically elevated IOP was a mechanical compression of axons within the lamina cribrosa that led to an obstruction of axonal transport and, secondarily, to a reduction in blood flow (Anderson, 1969; Anderson & Hendrickson, 1974; Anderson & Hendrickson, 1977; Burgoyne et al, 2005; Quigley & Anderson, 1976; Quigley & Addicks, 1980; Quigley & Anderson, 1977; Quigley et al, 1979).

### *1.4.3 Potential mechanisms*

The mechanisms of glaucomatous damage are not fully understood; many factors (e.g., mechanical, vascular, and glial) likely contribute to RGC death. Mechanical theories

suggest that stress from increased IOP can strain and deform the lamina, resulting in biomechanical alterations to the load-bearing laminar beams, changes in laminar beam and pore geometry, and mechanical alterations (e.g., compression and shearing) of RGC axons (Bellezza et al, 2000; Bellezza et al, 2003; Burgoyne et al, 2005; Downs et al, 2008; Fechtner & Weinreb, 1994; Roberts et al, 2010; Sigal et al, 2004; Vilupuru et al, 2007). Vascular theories propose that increases in IOP result in perfusion instabilities in the ONH, producing alterations in ocular blood flow and a reduced blood supply to laminar capillaries that lead to axonal damage (Burgoyne et al, 2005; Farquhar, 1991; Fechtner & Weinreb, 1994; Hernandez & Gong, 1996). Glial theories suggest that increases in IOP result in an activation of astrocytes and glial cells that could potentially reduce neurotrophic support to RGC axons and create a harmful, neurotoxic environment (Hernandez, 2000; Neufeld, 1999a; Neufeld, 1999b; Neufeld et al, 1997). However, it is important to note that these theories likely occur simultaneously, making it challenging to isolate individual mechanisms of glaucoma onset and progression.

#### *1.4.3.1 Mechanical hypothesis*

The ONH can be considered as a biomechanical structure that is vulnerable to normal and increased levels of IOP (Burgoyne et al, 2005). Increases and fluctuations in IOP can impart a stress on the ONH and load bearing laminar beams, resulting in subsequent biomechanical alterations in glaucoma. Stresses acting on the ONH can be defined by two primary forces: (1) a force normal to the ONH surface that acts to posteriorly deform the lamina, and (2) a radial force that leads to expansion of the scleral canal (which pulls the lamina taut, closer to its normal physiological position in the ONH) (Downs et al, 2008; Fechtner & Weinreb, 1994). The stresses exerted by increases in IOP can strain or deform the lamina beyond normal limits (Bellezza et al, 2000; Roberts et al, 2010; Sigal et al, 2004), leading to permanent biomechanical changes in laminar

beams (Bellezza et al, 2003; Downs et al, 2008) and pores (Vilupuru et al, 2007). For example, IOP-induced changes in lamina cribrosa geometry have been shown to include a change in orientation, shape, size, and spacing of laminar beams and pores (Bellezza et al, 2003; Downs et al, 2008; Vilupuru et al, 2007). Figure 1-5 illustrates changes in ONH structure at different stages of experimental glaucoma based on data acquired from 3D histomorphometric reconstructions (Burgoyne & Downs, 2008). As shown in Fig. 1-5b, the lamina thickens and bows posteriorly while the scleral canal expands (arrowheads) in response to chronically elevated IOP in early experimental glaucoma. Consequently, these biomechanical changes likely alter laminar beam and pore geometry compared to the original, baseline geometry (Fig. 1-5a). Lateral and axial changes in beams and pores can mechanically damage RGC axons passing through the new, biomechanically altered pore morphology (Fechtner & Weinreb, 1994). In addition, conformational changes in laminar beams and pores can also lead to secondary effects that compromise blood flow (Burgoyne et al, 2005) and astrocyte function (Hernandez, 2000a), thereby hindering axonal health and performance (Anderson, 1969; Anderson & Hendrickson, 1974; Anderson & Hendrickson, 1977; Quigley & Anderson, 1976; Quigley & Addicks, 1980; Quigley & Anderson, 1977; Quigley et al, 1979).

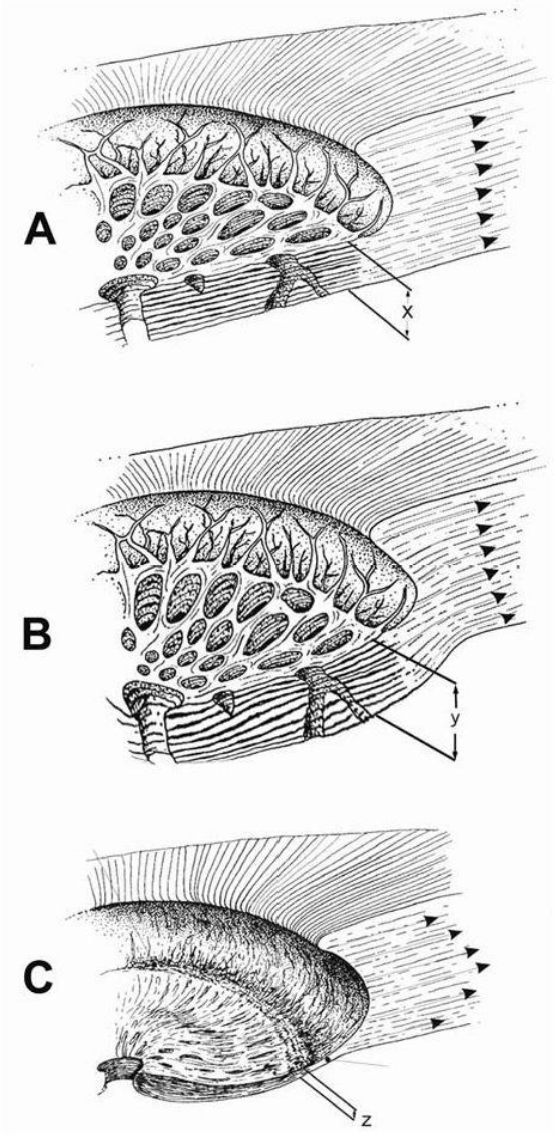


**Figure 1-5.** In early experimental glaucoma, an increase in IOP imparts a stress that strains or deforms the lamina cribrosa, resulting in (b) an initial backward bowing and thickening of the lamina compared to (a) its normal laminar structure and geometry. This change could subsequently alter beam and pore structure and orientation, in which pores become larger and more elongated. (c) Towards end-stage glaucoma, the lamina cribrosa becomes severely thinned and the laminar beams become severely damaged, resulting in profound axonal damage. Reprinted with permission (Burgoyne & Downs, 2008).

### *1.4.3.2 Vascular hypothesis*

The lamina cribrosa's blood supply is provided by the short posterior ciliary artery and laminar capillaries which lie within the collagen beams (Fig. 1-3). Nutrients from the blood supply must first diffuse through the endothelial cell basement membranes of the laminar capillaries, then through the ECM and across the astrocytes (which encase the laminar beams) to the axon bundles. This diffusion of nutrients from the laminar capillaries to the axon bundles can be obstructed due to high levels of IOP even under normal conditions of elastic strain (Fechtner & Weinreb, 1994). For example, a posterior bowing of the lamina resulting from elevated IOP may strain collagen beams and affect the capillaries within the beams that deliver nutrients to the axon bundles (Burgoyne et al, 2005). Nutrient diffusion to the axons might also reduce due to capillary thickening and a stiffening of the laminar ECM, making it more difficult for the nutrients to diffuse across these structures (Farquhar, 1991; Hernandez & Gong, 1996).

### *1.4.3.3 Glial hypothesis*

The major glial cell type in humans and non-human primates is the astrocyte (Hernandez, 2000). Astrocytes provide cellular transport functions to the axons, synthesize ECM macromolecules, and form lamellae that are oriented perpendicular to axons in the lamina cribrosa. The basement membrane of these astrocytes separates them from underlying collagen and elastin.

Multiple types of glial cells exist in the ONH. Type 1A astrocytes express glial fibrillary acidic protein (GFAP) and are present in prelaminar glial columns and at the edges of laminar beams. Type 1B astrocytes are the largest glial cell population in the ONH. They are found within the prelaminar glial columns and line prelaminar blood vessels and laminar beams. These glial cells express GFAP and neural cell adhesion molecules (NCAMs), and are also the primary source of ECM synthesis in the ONH

during development and throughout life. Lamina cribrosa cells are another major glial cell type that reside inside the ECM of the laminar beams. Unlike astrocytes, however, lamina cribrosa cells do not express GFAP. Lastly, microglia are a subtype of glial cell in the central nervous system and become activated as a result of neuronal injury (Hernandez, 2000). Inactive microglia have been seen in normal ONHs in blood vessel walls and capillary walls in the prelaminar glial columns and lamina cribrosa. Activated microglia have been seen in glaucomatous ONHs in the lamina cribrosa region (Neufeld, 1999a). Once an injury occurs (possibly from an elevation in IOP), reactive astrocytes surround the injury and isolate healthy neural tissues from secondary injuries. Reactive astrocytes also increase synthesis of ECM macromolecules, which, in turn, initiates a remodeling of the microenvironment in the lamina cribrosa. However, this protective mechanism might have adverse effects that lead to axonal damage. For example, recent studies in human glaucoma and in a rat model of elevated IOP suggest that reactive astrocytes induce synthesis of nitric oxide synthase (NOS-2), an enzyme that may be neurotoxic to RGC axons in the ONH (Neufeld, 1999b; Neufeld et al, 1997; Neufeld et al, 1999).

In summary, in the process of being reactivated to reduce neuronal injury, astrocytes may create a remodeled, inhospitable environment for the RGC axons as they pass through the lamina cribrosa. A remodeled environment might result in further damage to axons.

### *1.4.4 Experimental model of glaucoma*

Early damage to the ONH occurs not only in human glaucoma patients and non-human primate models of experimental glaucoma (Bellezza et al, 2003; Burgoyne et al, 2004; Downs et al, 2005; Downs et al, 2007; Yang et al, 2007a; Yang et al, 2007b), but also in mouse (Danias et al, 2003; Filippopoulos et al, 2006; Howell et al, 2007; Jakobs et al,

2005; Schlamp et al, 2006) and rat (Cepurna et al, 2005; Johnson et al, 2000; Johnson et al, 1996) models of experimental glaucoma. Because glaucoma progression occurs slowly in humans, it is challenging to study all stages of the disease longitudinally in human patients. Therefore, it is valuable to explore disease mechanisms in animal models in which glaucomatous neuropathy occurs over the span of months (as opposed to many years in humans). The monkey model of experimental glaucoma has been studied extensively and shows structural and functional changes in cupping, RNFL thickness, and visual field sensitivity that are similar to those seen in human patients with POAG (Gaasterland & Kupfer, 1974; Harwerth et al, 1993; Harwerth et al, 1997; Pederson & Gaasterland, 1984; Quigley & Hohman, 1983). Briefly, argon laser scarring of the trabecular meshwork is performed unilaterally to damage the aqueous outflow pathway and significantly reduce aqueous humour outflow, thereby elevating IOP (Harwerth et al, 1997). The contralateral eye is used as a control.

### 1.5 Structural changes in the optic nerve head (ONH) in glaucoma

ONH tissues have been examined during disease in human glaucomatous eyes and monkey models of experimental glaucoma. In early post-mortem studies of human eyes with glaucoma, scanning electron microscopy images of the lamina cribrosa showed a 0.7 mm displacement of the laminar surface from the sclera and a lateral extension of the lamina cribrosa as a result of scleral expansion (Quigley et al, 1981). Consequently, the lamina was compressed, resulting in a noticeable distortion of the shape of the RGC axon bundles and the pathways they followed through the lamina. Additional *ex vivo* studies in human glaucomatous eyes also revealed a backward bowing of the entire lamina in the upper and lower poles of the ONH (Quigley et al, 1983). Recent studies in early experimental glaucoma have reported an enlargement of the neural canal in parallel with ONH surface change detected using confocal scanning laser tomography

(CSLT), as well as significant changes in prelaminar and laminar tissues (Downs et al, 2007; Yang et al, 2007a). Additional *ex vivo* studies have described an overall thickening of the lamina cribrosa and a posterior deformation of the anterior laminar surface (i.e., increase in anterior lamina cribrosa surface depth [ALCSD]) in early experimental glaucoma eyes compared to fellow, control eyes (Bellezza et al, 2003; Burgoyne et al, 2004; Yang et al, 2007b). With the development of spectral domain optical coherence tomography (SDOCT) image processing techniques (e.g., enhanced depth imaging, blood vessel shadow removal, and contrast enhancement) that provide improved visualization of ONH structures such as the lamina cribrosa (Fujiwara et al, 2009; Girard et al, 2011; Imamura et al, 2011; Spaide et al, 2008), *in vivo* studies have been performed to validate these *ex vivo* results. For example, using SDOCT imaging, increases in mean ALCSD have been measured in monkey eyes with early experimental glaucoma (compared to fellow control eyes) and in human glaucoma patients (compared to normal eyes) (Furlanetto et al, 2013; Strouthidis et al, 2011b).

### 1.6 Structural changes in lamina cribrosa microarchitecture in glaucoma

Early studies that investigated lamina cribrosa microarchitecture in glaucoma were largely carried out on post-mortem tissue from excised eyes. Using stereo scanning electron microscopy, Emery et al. imaged the post-mortem anterior lamina cribrosa in 24 normal eyes and 6 eyes with acute or chronic glaucoma and noted that pores ranged from 10 µm to 50 µm in diameter in normal eyes (Emery et al, 1974). However, in eyes with moderately advanced chronic glaucoma, pores became more difficult to visualize on the anterior laminar surface. Moreover, an increased elongation of laminar pores was noted near the disc rim in eyes with advanced glaucoma (compared to normal eyes).

The microarchitecture of laminar connective tissues has more recently been examined in normal monkey eyes and monkey eyes induced with unilateral early

experimental glaucoma (Roberts et al, 2009). Based on 3D histomorphometric reconstructions of the ONH, lamina cribrosa connective tissue was found to be most dense in central and superior regions of the ONH and laminar beams tended to be radially oriented along the periphery of the ONH in normal eyes. However, connective tissue volume was larger in eyes with experimental glaucoma (compared to fellow control eyes) and an increased number of beams were discovered throughout the thickness of the lamina. In addition, no differences in laminar beam orientation were noted in the early experimental glaucoma eyes (Roberts et al, 2009).

Building on early histological reports of laminar microarchitecture in glaucomatous eyes, subsequent investigations examined anterior laminar pores *in vivo* in human glaucomatous eyes using optic disc photography (Miller & Quigley, 1988; Susanna, 1983) and reported qualitative differences in pore geometry (e.g., increasing pore elongation with disease). Bhandari et al. reported data detailing the repeatability and reproducibility of measuring lamina cribrosa pores *in vivo* in 10 eyes using confocal scanning laser ophthalmoscope (SLO) imaging (Bhandari et al, 1997). Fontana et al. used this modified confocal SLO to measure laminar pore geometry (in units of pixels) in human glaucomatous eyes and found pore area and elongation increased with increasing visual field loss (Fontana et al, 1998). Subsequently, Tezel et al. examined laminar pores from color disc photographs in human glaucomatous eyes and found that pores became smaller between baseline and follow up time-points, whereas pore elongation did not change significantly (Tezel et al, 2004). These *in vivo* experiments suggested a need to conduct *in vivo* imaging of structural changes in the lamina cribrosa in the same eyes over time to resolve contradictory evidence.

Despite providing an important step forward, image resolution in these early *in vivo* studies was restricted by the wide field of view of the imaging technique (i.e., confocal SLO, disc photography) and the presence of optical aberrations in the patient's

eyes. These factors limited the number of subjects in which laminar pores could be visualized, as well as the minimum size of pores that could be accurately quantified. Moreover, pore parameters were not adjusted for each eye's axial length and anterior laminar surface curvature. Vilupuru et al. used *in vivo* confocal adaptive optics scanning laser ophthalmoscopy (AOSLO) imaging to correct the eye's aberrations and noninvasively achieve high-resolution, high-contrast images of anterior lamina cribrosa surface (ALCS) beams and pores (Fig. 1-6). They showed laminar pore areas were larger in all monkey eyes with experimental glaucoma (compared to fellow control eyes). Laminar pore elongation was significantly larger in 1 of 3 experimental glaucoma eyes while laminar pore nearest neighbor distance (NND) was significantly greater in 2 of 3 experimental glaucoma eyes (relative to fellow control eyes). However, longitudinal changes in pore geometry with disease progression were not reported (Vilupuru et al, 2007). Chapters 2, 3, and 4 in this dissertation discuss the repeatability and variability in normal eyes as well longitudinal changes in lamina cribrosa microarchitecture using AOSLO imaging.

Furthermore, the excellent lateral resolution afforded by adaptive optics has recently been paired with the high axial resolution inherent in OCT to obtain high-resolution images of the lamina cribrosa in three dimensions (Nadler et al, 2013; Torti et al, 2009; Wang et al, 2013). Torti et al. acquired some of the first high-resolution images of the lamina using AOOCT, but quantitative data on the laminar microarchitecture was not reported (Torti et al, 2009).

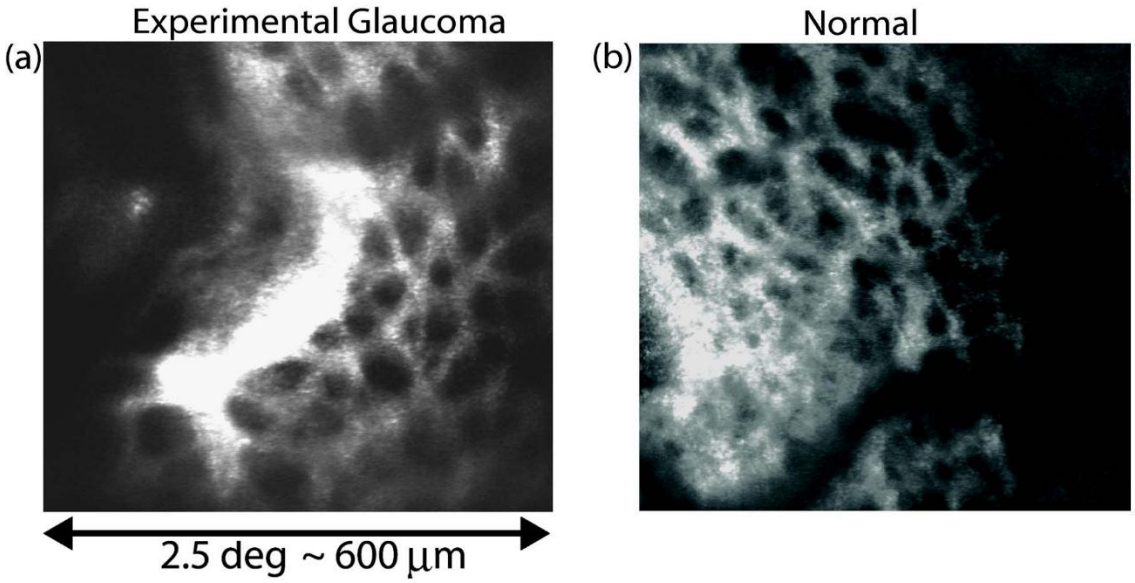


**Figure 1-6.** AOSLO images of anterior laminar surface pores in (a) the experimental glaucoma and (b) fellow normal control eyes of the same monkey. Mean pore area and nearest neighbor distance (NND) were significantly larger in the experimental glaucoma eye compared to the control eye. Reprinted with permission (Vilupuru et al, 2007).

More recently, Nadler et al. and Wang et al. used swept-source OCT (SSOCT) and AOOCT imaging to acquire and quantify laminar microarchitecture in volumetric images from normal healthy and glaucomatous human eyes (Nadler et al, 2013; Wang et al, 2013). They found that eyes with worsening visual sensitivity had significantly decreased pore diameter and significantly increased beam thickness. In summary, combining adaptive optics with OCT or SLO imaging techniques allows for *in vivo* visualization of microscopic structures that previously could only have been seen via histology.

### 1.7 Structure-function changes in glaucoma

Conventional structural and functional measures used clinically to diagnose glaucoma and assess its progression include structural alterations in the ONH (often characterized by cupping), decreases in RNFL thickness (RNFLT), and losses in visual function (often in characteristic patterns and severity) (Anton et al, 2007; Budenz et al, 2005; Harwerth, 2010; Nouri-Mahdavi et al, 2004; Quigley, 2005; Schuman et al, 1995; Sihota et al, 2006; Wollstein et al, 2005). However, it is estimated that 40-50% of retinal ganglion cells (RGCs) are non-functional by the time visual field testing, as measured via standard automated perimetry (SAP), reliably detects vision loss (Harwerth et al, 1999). Consequently, a change in RNFLT (measured via OCT) has been shown to be a more sensitive metric for detecting early changes in glaucoma compared to SAP measures of visual field loss (Harwerth et al, 2007). While RNFLT has become a prevalent clinical measure on axonal integrity in glaucoma, recent work has shown that 10-15% of RGC axons are already lost when a first change in RNFLT is reliably detected with spectral domain optical coherence tomography (SDOCT) (Cull et al, 2012). Furthermore, other structural changes (e.g., ONH surface change as measured by CSLT) and functional changes (e.g., decrease in RGC activity as measured by the multifocal electroretinogram

[mfERG]) have recently been reported to occur earlier than RNFLT changes in non-human primates with experimental glaucoma (Fortune et al, 2012).

These studies substantiate the need for exploring earlier markers of disease onset and progression as the most widely used functional marker (visual field loss measured using SAP) and structural markers (ONH cupping and losses in RNFLT) do not appear to measure the earliest changes in glaucoma. It is crucial to develop earlier markers for detecting glaucomatous damage that allow for more informed clinical decision-making about treatment. Therefore, the work presented in this dissertation aims to shed light on early structural changes that occur in the ONH and lamina cribrosa microarchitecture and on early functional changes (measured using the mfERG), as well as conventional clinical changes used to detect structural and functional loss (i.e., RNFL thickness and perimetry, respectively) in glaucoma.

### 1.8 Specific aims

#### 1.8.1 Quantify reproducibility of measuring lamina cribrosa pore geometry *in vivo* in normal human and non-human primates using an AOSLO (Published in IOVS; Ivers et al., 2011).

The ability to consistently resolve lamina cribrosa pores *in vivo* has applications in the study of ONH disease mechanisms. We have assessed the repeatability in imaging and quantifying laminar pores *in vivo* in normal human and non-human primate eyes using an AOSLO at different time points. This study provides an important first step in understanding the feasibility of using *in vivo* AOSLO imaging to assess laminar structure in normal human and monkey eyes, human glaucomatous patients and monkey eyes with experimental glaucoma.

### 1.8.2 Characterize inter-eye differences in lamina cribrosa and ONH structure *in vivo* in normal non-human primates.

Differences in lamina cribrosa pore and surface geometry have been observed between monkey eyes with unilateral experimental glaucoma and their fellow control eyes. To ensure that any potential structural differences measured in experimental glaucoma are due to the disease itself and not to the normal variability inherent in these examined parameters between fellow eyes, we assessed differences in anterior lamina cribrosa pore and ONH geometry between fellow eyes of 6 normal monkeys *in vivo* using AOSLO and SDOCT imaging. This study quantifies and provides a better understanding of the variability in ONH geometry and lamina cribrosa microarchitecture between fellow eyes of normal monkeys and will be used for future inter-eye comparisons in non-human primate eyes with unilateral laser-induced experimental glaucoma.

### 1.8.3 Determine whether changes in anterior lamina cribrosa pore microarchitecture and ONH structure precede changes in retinal nerve fiber layer thickness *in vivo* in non-human primates with experimental glaucoma.

It has been suggested that the initial insult to RGC axons occurs at the lamina cribrosa. Based on the working hypothesis that structural alterations in the lamina cribrosa result in axonal degeneration and subsequent RGC death in glaucoma, we longitudinally examined global and local changes *in vivo* in anterior lamina cribrosa pores along with structural changes in the ONH and RNFL to determine whether changes in laminar pore and ONH structure precede changes in RNFLT in non-human primates with unilateral experimental glaucoma. This study provides a better understanding of the time-course of structural changes in the lamina cribrosa, ONH, and RNFL in early stages of glaucoma.

### 1.8.4 Determine whether structural changes in the ONH and lamina cribrosa microarchitecture observed *in vivo* in experimental glaucoma in non-human primates precede changes in visual function.

Although several studies support the idea that axonal insult in glaucoma initially occurs at the lamina cribrosa, there is a lack of evidence that relates longitudinal changes in laminar pore and ONH geometries with vision loss in living diseased eyes. We longitudinally examined and compared early *in vivo* structural changes in the ONH, anterior lamina cribrosa surface microarchitecture, and RNFL with functional changes in SAP (to measure visual field sensitivity) and the mfERG (to measure the light-adapted multi-focal photopic negative response [mfPhNR]) in 3 non-human primates with unilateral experimental glaucoma. This study provides improved understanding of the time-course of structural and functional changes that occur in early experimental glaucoma.

# CHAPTER 2

## Reproducibility of measuring lamina cribrosa pore geometry in human and non-human primates using *in vivo* adaptive optics imaging

**Contributing authors:**

Chaohong Li, PhD, Nimesh B. Patel, OD, PhD, Nripun Sredar, Xunda Luo, PhD, Hope M. Queener, Ronald S. Harwerth, OD, PhD, and Jason Porter, PhD

*This chapter has been published in Investigative Ophthalmology & Visual Science, 2011: 52: 5473-5480.

**Abstract**

**Purpose:** The ability to consistently resolve lamina cribrosa pores *in vivo* has applications in the study of optic nerve head and retinal disease mechanisms. We assessed the repeatability in imaging laminar pores in normal living eyes using a confocal adaptive optics scanning laser ophthalmoscope (AOSLO).

**Methods:** Reflectance images (840 nm) of the anterior lamina cribrosa were acquired using the AOSLO in ≥ 4 different sessions in 2 normal rhesus monkey eyes and 3 normal human eyes. Laminar pore areas, elongations (ratio of major to minor axes of the best-fit ellipse), and nearest neighbor distances were calculated for each session. Measurement repeatability was assessed across sessions.

**Results:** Pore areas ranged from 90 to 4,365 $\mu m^2$ in monkeys and 154 to 6,637 $\mu m^2$ in humans. Mean variabilities in measuring pore area and elongation (i.e., mean of the standard deviation of measurements made across sessions for the same pores) were 50 $\mu m^2$ (6.1%) and 0.13 (6.7%), respectively, in monkeys, and 113 $\mu m^2$ (8.3%) and 0.17 (7.7%), respectively, in humans. Mean variabilities in measuring nearest neighbor distances were 1.93 µm (5.2%) in monkeys and 2.79 µm (4.1%) in humans. There were no statistically significant differences in any pore parameters across sessions (ANOVA, $P>.05$).

**Conclusions:** The anterior lamina cribrosa was consistently imaged *in vivo* in normal monkey and human eyes. Small intersession variability in normal pore geometry suggests that AOSLO imaging could potentially be used to measure and track changes in laminar pores *in vivo* during glaucomatous progression.

## 2.1 Introduction

Glaucoma is a multifaceted group of eye diseases that results in the degeneration of retinal ganglion cell axons and the death of retinal ganglion cells (RGCs). The mechanisms of glaucomatous damage (e.g., mechanical, vascular, glial, etc.) are not fully understood. While several of these factors likely contribute to RGC death, substantial evidence suggests that the initial site of axonal injury likely occurs at the level of the lamina cribrosa in the optic nerve head (Anderson & Hendrickson, 1974; Anderson & Hendrickson, 1977; Howell et al, 2007; Minckler & Spaeth, 1981; Quigley & Addicks, 1980; Quigley et al, 1982; Quigley & Anderson, 1976; Quigley & Anderson, 1977; Quigley et al, 1980; Quigley et al, 1979; Quigley et al, 1983). In humans and non-human primates, the lamina cribrosa is a three-dimensional porous structure consisting of flexible beams of collagenous tissue that support and nourish the RGC axons passing through it from the retina to the brain. Increases in intraocular pressure (IOP) impart stress and strain on the lamina (Bellezza, 2000; Roberts et al, 2010; Sigal et al, 2004), resulting in a posterior bowing and stretching of the load-bearing laminar beams (Bellezza et al, 2003; Downs et al, 2008) and potential increases in laminar pore area and elongation (or more elliptically shaped pores). Stretching and deformation of the laminar beams (and associated pores) could shear or damage encompassed axons and laminar capillaries, thereby hampering axonal transport, blood flow, and the diffusion of nutrients (Anderson, 1969), and/or the neurotrophic support provided to the axons due to alterations in glial cells (Hernandez, 2000).

Optic nerve head tissues have been examined in human glaucomatous eyes and non-human primate models of experimental glaucoma. Postmortem histological studies have shown significant changes in prelaminar and laminar tissues within the ONH in early experimental glaucoma (Bellezza et al, 2003; Roberts et al, 2009; Yang et al, 2007a). Additional *ex vivo* studies in glaucomatous human and non-human primate eyes

have described early changes in laminar morphology and position (Bellezza et al, 2003; Quigley & Addicks, 1981), laminar pore geometry (Emery et al, 1974), and the composition and architecture of laminar connective tissues (Hernandez et al, 1990; Roberts et al, 2009). In light of this work, there is growing consensus that *in vivo* studies are necessary to validate *ex vivo* results and examine longitudinal changes during glaucoma (Walsh & Quigley, 2008; Yang et al, 2010).

The lamina cribrosa has been examined *in vivo.* Fontana et al. imaged anterior laminar pores in living human glaucomatous eyes using a modified confocal scanning laser ophthalmoscope (SLO) and showed that pore area and elongation were larger in eyes with more severe glaucoma (Fontana et al, 1998). However, images were taken using a wide field-of-view (20°) and were not of high resolution due to the presence of ocular aberrations. Therefore, the size and total number of pores that could be resolved and the number of subjects in which laminar pores could be successfully imaged were limited. Vilupuru et al. used a confocal adaptive optics scanning laser ophthalmoscope (AOSLO), an instrument that noninvasively provides cellular-level images through a correction of the eye's aberrations, to improve the resolution and contrast of laminar images *in vivo* in non-human primates with experimental glaucoma (Vilupuru et al, 2007). This study quantified laminar pore geometries in 3 diseased monkey eyes, each at a single time-point. However, changes in pore geometry with disease were not investigated. Recent studies have combined adaptive optics with optical coherence tomography (OCT) to image the human lamina cribrosa in three spatial dimensions (Torti et al, 2009; Zawadzki et al, 2009), but a quantitative analysis of laminar geometry and pore structure has not been reported.

We have assessed the repeatability of imaging and quantifying laminar pores *in vivo* in two normal macaque and three normal human eyes using an AOSLO at different time-points. Statistical tests were performed to investigate whether significant

differences were present in any analyzed laminar pore parameters within and across imaging sessions. This study provides an important first step in understanding the feasibility of using *in vivo* AOSLO imaging to assess laminar structure in normal eyes, human glaucomatous eyes, and non-human primate eyes with experimentally-induced glaucoma.

### 2.2 Methods

All animal care experimental procedures were approved by the University of Houston's Institutional Animal Care and Use Committee, and adhered to the ARVO statement for the Use of Animals in Ophthalmic and Vision Research. All human subjects research adhered to the tenets of the Declaration of Helsinki and the study protocol was approved by the University of Houston's Committee for the Protection of Human Subjects. An informed consent was obtained for each human subject.

The anterior lamina cribrosa was examined *in vivo* in two normal rhesus monkeys (*Macaca mulatta*), aged 1.5 (M036) and 7 years (M057), and three normal humans: a 24 y.o. female of Indian descent (H058), a 31 y.o. male of Indian descent (H030), and a 47 y.o. Caucasian male (H055). All human eyes had $\leq$ -1.50 D of spherical refractive error and $\leq$ -1.00 D of cylinder. Monkeys were anesthetized with 20-25 mg/kg ketamine, 0.8-0.9 mg/kg xylazine, and 0.04 mg/kg atropine sulfate to minimize eye movements during *in vivo* imaging (Frishman et al, 1996). Monkeys and humans were dilated with 2.5% phenylephrine and 1% tropicamide. A speculum was used to hold the monkey eyelid open and a contact lens was placed on the monkey eye to prevent corneal dehydration during imaging.

### *2.2.1 Fundus Imaging*

Prior to AOSLO imaging, monkey and human eyes were imaged with the Spectralis HRA+OCT (Heidelberg Engineering, Germany) to acquire wide-field SLO fundus images of the ONH. The wide-field images (15°, 20°, or 30° in extent) were useful during AOSLO imaging sessions for navigating throughout the retina as the AOSLO imaging field was small (1.5°). Landmarks in the fundus images, such as vasculature, were easy to recognize and relocate across separate imaging sessions.

### *2.2.2 Biometric measurements and image scaling*

Axial length, anterior chamber depth, and anterior corneal curvature were measured in all human and monkey eyes using the IOLMaster (Carl Zeiss Meditec, Germany). These biometric measurements were incorporated into a model eye to convert visual angle (in degrees) to retinal size (in micrometers). For monkeys, we generated a 3-surface model eye which incorporated the IOLMaster measurements and previously published measurements of lens thickness and curvatures corresponding to each monkey's age (Qiao-Grider et al, 2007). For humans, IOLMaster measurements were incorporated into a 4-surface model eye as described by Li et al (Li et al, 2010b). In both models, the location of the secondary nodal point (N') was calculated and retinal size (x) was determined using the equation:

$$\tan\theta = \frac{x}{N'R} \tag{1}$$

where $\theta$ is the visual angle and N'R is the distance from N' to the retina.

### *2.2.3 Adaptive optics scanning laser ophthalmoscope (AOSLO) imaging and analysis*

The monkey's head was stabilized for imaging using a head mount attached to an XYZ

translation stage. The tip, tilt, and rotation capabilities of the head mount allowed the head to be positioned for imaging the optic disc and lamina cribrosa. The translation stage was used to center the eye's pupil on the AOSLO system. Human eyes were stabilized and positioned using a custom-made bite bar attached to an XYZ translation stage. Subjects fixated on a laser pointer projected on to a fixation target. The pointer was moved until the optic nerve head could be visualized in each subject.

An 840 nm superluminescent diode (Superlum, Ireland) was used for wavefront sensing and reflectance imaging. The power of this source at the corneal plane was ~300 μW (which is greater than 10 times below the maximum permissible exposure dictated by the ANSI standards for a 1.5° field size, 1.5 hour exposure, and wavelength of 840 nm) (ANSI, 2000; Delori et al, 2007). Aberrations were measured and corrected (10 Hz) over a dilated pupil (typically ~8 mm) using a Shack-Hartmann wavefront sensor and two deformable mirrors (or a woofer-tweeter system) (Li et al, 2010a). A high-stroke deformable mirror (Mirao 52-e, Imagine Eyes, Inc., France) corrected large amplitude, lower order aberrations, while a lower-stroke deformable mirror (Multi-DM MEMS, Boston Micromachines, Inc., Cambridge, MA) corrected low amplitude, higher order aberrations.

Following adaptive optics correction, retinal videos were captured over a 1.5° field at a rate of 25 Hz. Through-focus images were acquired at different depths in the ONH to determine the plane of best-focus of the anterior laminar surface (Fig. 2-1). The plane of best-focus corresponded to the location where the edges of the anterior laminar pores first became sharpest and image brightness and contrast were optimal (Fig. 2-1e). When focused above the anterior surface of the lamina, vasculature was in focus (Fig. 2-1a,b). When focused below the anterior surface, image brightness, contrast, and resolution decreased (Fig. 2-1k,l), likely due to increased light scatter and optical defocus. It was not possible to visualize the entire anterior laminar surface as some

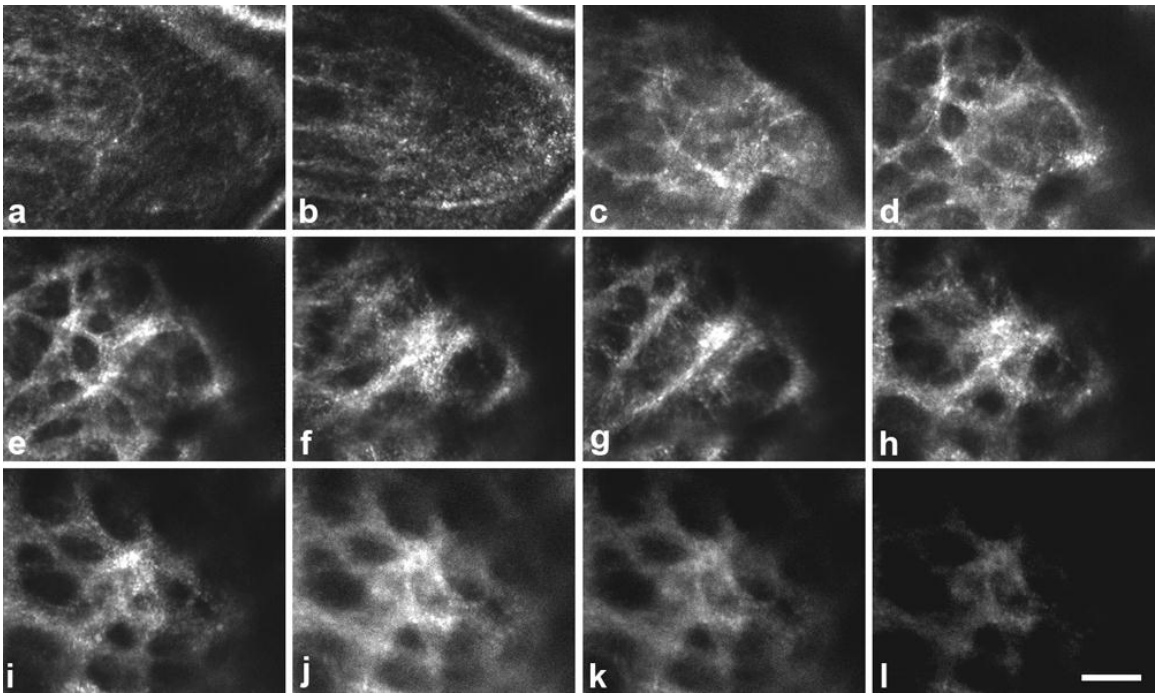


**Figure 2-1.** Through-focus images of the macaque (M036) lamina cribrosa shown in an (a) anterior to (l) posterior direction. Vasculature was in focus in the most anterior sections. As the focal plane was moved posteriorly, the lamina gradually came in to and went out of focus. The anterior laminar surface was judged to be in best-focus when pore edges first became sharpest and image brightness and contrast were optimal (e). Scale bar: 50 μm.

regions were obstructed by overlying vasculature. Therefore, we imaged as much of the lamina as possible in each session. A maximum of 30 minutes was typically required to image the lamina cribrosa in a given eye. Monkeys and humans were imaged on at least 4 different occasions, each separated by a minimum of one week.

### *2.2.4 Image processing and analysis*

AOSLO videos were processed off-line using a customized MATLAB program (The MathWorks, Inc., Natick, MA) to remove image distortions caused by eye movements that occurred during video acquisition. Individual frames were first registered using a normalized cross-correlation technique. Several frames were then averaged to yield a single, high signal-to-noise registered image (Fig. 2-2). Montages of the lamina cribrosa were generated from the individual registered images using Adobe Photoshop (Adobe Systems, San Jose, CA).

For each montage of the anterior lamina cribrosa, individual laminar pores were identified and four pore parameters (previously used to assess pore geometry) were calculated: pore area, elongation (ratio of major to minor axes of an ellipse best-fit to each pore), centroid location, and nearest neighbor distance (Fontana et al, 1998; Vilupuru et al, 2007). Each pore was identified manually in Adobe Photoshop by drawing a polygon about its edge (or boundary). For cases in which it was challenging to determine (from the registered image) whether a large pore actually consisted of smaller pores, the through-focus videos were used to examine laminar beam orientation about the plane of best-focus and make a decision. For example, pores marked with an "∗" in Fig. 2-2c represent pores that were deemed to be a single pore (rather than a collection of smaller pores) after watching the videos. Once the pores were demarcated, the image was binarized such that the laminar pores were filled white

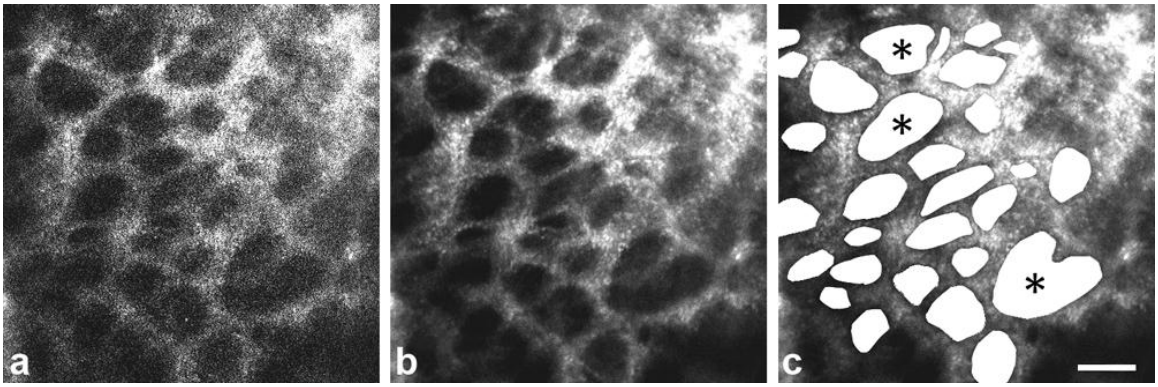


**Figure 2-2.** (a) Single frame from an AOSLO video of a macaque (M057) lamina cribrosa. While laminar pores can be seen, their edges are poorly defined. (b) Registering and averaging several frames (30 frames in this example) increased the signal-to-noise ratio. Edges and contrast of pores are greatly improved. (c) Individual pores were identified throughout the lamina and pore parameters were calculated. Pores marked with an "∗" represent pores that were deemed to be a single pore (rather than a collection of smaller pores) after examining the through-focus videos. Scale bar: 50 μm.

and the image background was black. The resultant image was imported into ImageJ (National Institutes of Health, Bethesda, MD) where the area, centroid location, and major and minor axes of the best-fitted ellipse were quantified for each pore. Pore elongation was calculated by taking the ratio of the major to minor axes of the best-fitted ellipse. The nearest neighbor distance (NND) of each pore was calculated as the minimum Euclidean distance between the centroid position of a given pore and that of its immediately surrounding neighbors.

This pore identification and quantification method was applied to montages of the anterior lamina cribrosa acquired in each imaging session. Two independent observers analyzed the same laminar pores in a single montage from a randomly selected time-point in each human and monkey eye to assess the inter-observer reproducibility of our pore identification and measurement method. Intraclass correlation coefficients accounting for two-way random effects for single measures, ICC(2,1), were calculated for each analyzed pore parameter (Shrout and Fleiss 1979). Pore parameters were also compared within the same eyes across imaging sessions. For each pore, the standard deviation of the mean value of each parameter across sessions was calculated to determine the variability in our imaging and measurement technique. Analysis of variance (ANOVA) tests for repeated measures were performed in order to compare pore parameters in each eye across all sessions. Only pores that could be imaged and quantified in all imaging sessions for each eye were included in the ANOVA analysis. To assess our intrasession variability, our identification and quantification process was repeated three separate times on the same montage acquired in a single imaging session. Pores were identified in a random sequence in each analysis and pore parameters were calculated and compared across analyses.

## 2.3 Results

Adaptive optics significantly improved the image quality of the lamina cribrosa *in vivo* in humans and macaques. Figure 2-3 compares Spectralis SLO fundus images of a monkey (M057) and human (H055) ONH when best-focused at the level of the lamina cribrosa (Fig. 3a,c) with an overlaid AOSLO montage of the anterior lamina cribrosa acquired in the same eyes (Fig. 2-3b,d). Even when best-focused at the level of the lamina, it is not possible to unambiguously resolve and quantify the majority of laminar pores using a high-quality, conventional SLO (Fig. 2-3a,c). Following a correction of the eye's aberrations, AOSLO imaging provides increased resolution and contrast of the pores (Fig. 2-3b,d), particularly along their boundaries, allowing for their identification and quantification.

Figure 2-4 shows montages of the anterior lamina cribrosa acquired in 2 normal monkey eyes and 3 normal human eyes. Laminar pores were identified in these montages and mean pore area, elongation, and NND were calculated for each individual eye and across species. The Intraclass Correlation Coefficients (ICCs) for laminar pore area, elongation, and NND in monkey eyes were 0.87, 0.83, and 0.97, respectively. The ICCs for pore area, elongation, and NND in human eyes were 0.83, 0.81, and 0.96, respectively. Given this excellent agreement between observers and the length of time typically required to generate a montage, subjectively delineate pore boundaries, and quantify pore geometry, a single investigator examined pores at all time-points in each eye.

Pore geometry results are summarized in Table 2-1a for monkeys and Table 2-1b for humans. Sixty-eight and 87 anterior laminar pores were analyzed in monkey eyes M036 and M057, respectively, while 18, 23, and 53 pores were analyzed in human eyes H058, H030, and H055, respectively. On average, mean pore parameters were larger in our human subjects compared to macaques. The mean pore

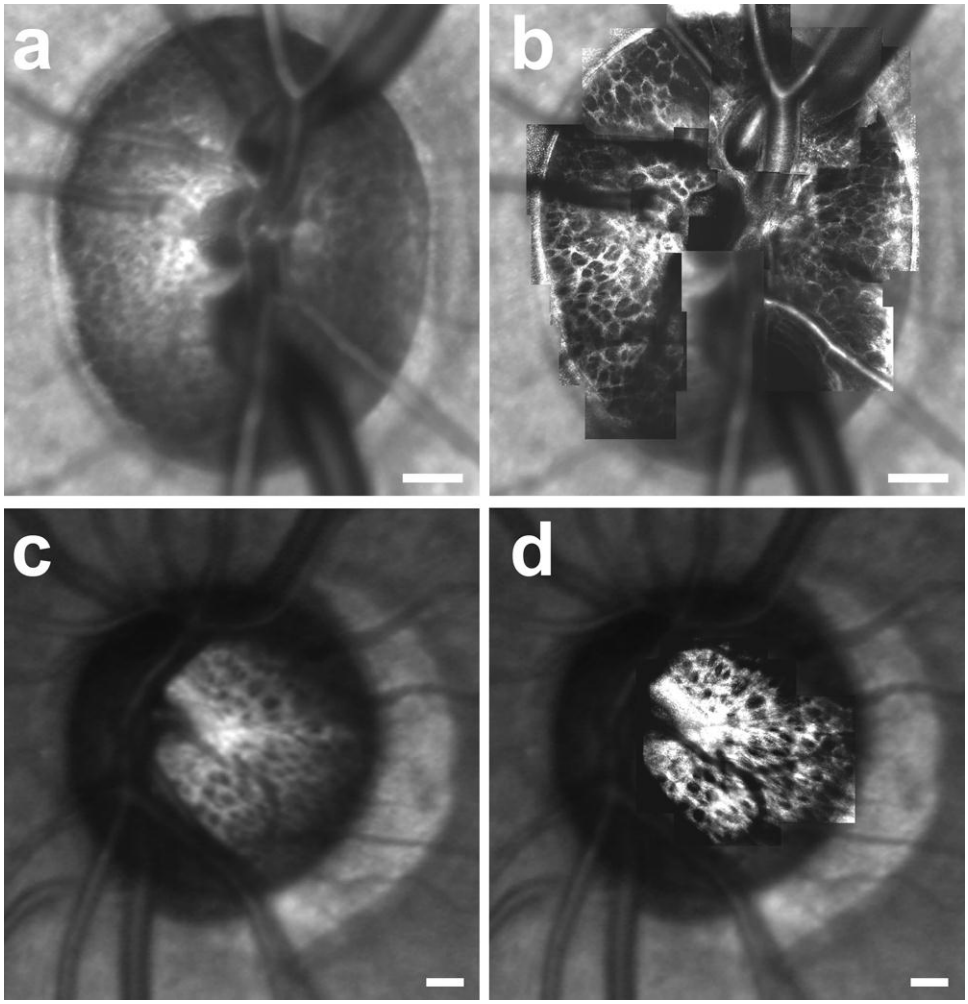


**Figure 2-3.** Spectralis SLO images of the (a) primate ONH (M057) and (c) human ONH (H055) when best-focused on the lamina. (b,d) Same Spectralis SLO images as on the left, but with the corresponding AOSLO montage overlaid on top. Resolution and contrast are improved following AO correction. Scale bar: 200 μm.

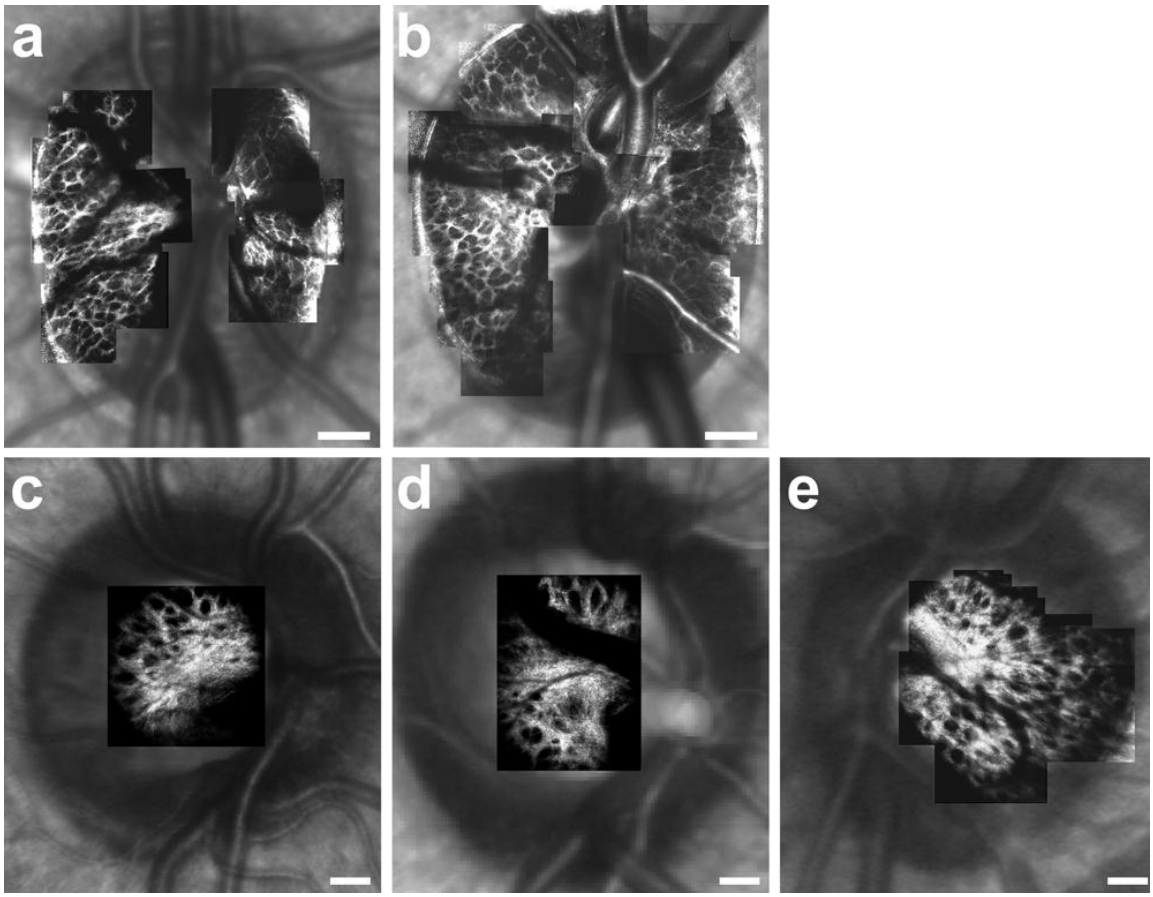


**Figure 2-4.** AOSLO montages of anterior lamina cribrosa overlaid on top of Spectralis SLO images for the (a,b) macaque and (c-e) human eyes analyzed in this study. Images show the typical maximum extent over which the lamina was imaged *in vivo* in each eye. Scale bar: 200 μm.

**Table 2-1a.** Mean values (± SD) and ranges of pore geometry in normal macaque eyes.

| | **Area** (μm$^2$) | | **Elongation** | | **NND** (μm) | |
|---|---|---|---|---|---|---|
| | Mean ± SD | Range | Mean ± SD | Range | Mean ± SD | Range |
| M036 | 870 ± 610 | 90 - 3439 | 1.90 ± 0.77 | 1.10 – 5.28 | 37.9 ± 7.62 | 17.8 – 54.7 |
| M057 | 1055 ± 907 | 122 – 4365 | 1.66 ± 0.54 | 1.06 – 4.79 | 36.0 ± 6.70 | 19.6 – 54.1 |
| All Eyes | 973 ± 794 | 90 - 4365 | 1.77 ± 0.66 | 1.06 – 5.28 | 36.9 ± 7.19 | 17.8 – 54.7 |

**Table 2-1b.** Mean values (± SD) and ranges of pore geometry in normal human eyes.

| | **Area** (μm$^2$) | | **Elongation** | | **NND** (μm) | |
|---|---|---|---|---|---|---|
| | Mean ± SD | Range | Mean ± SD | Range | Mean ± SD | Range |
| H030 | 1603 ± 1481 | 227 - 5568 | 1.85 ± 0.60 | 1.17 – 3.39 | 60.9 ± 17.0 | 29.3 – 94.5 |
| H055 | 1769 ± 1296 | 154 - 5560 | 2.14 ± 0.91 | 1.10 – 4.83 | 68.3 ± 16.9 | 37.1 - 114 |
| H058 | 1732 ± 1642 | 299 - 6637 | 1.88 ± 0.43 | 1.30 – 2.65 | 81.5 ± 25.6 | 52.5 – 125 |
| All Eyes | 1713 ± 1414 | 154 - 6637 | 2.00 ± 0.75 | 1.10 – 4.83 | 69.1 ± 19.8 | 29.3 - 125 |

areas (± 1 standard deviation) in macaques and humans were 973 ± 794 μm$^2$ and 1,713 ± 1,414 μm$^2$, respectively. In macaques, pore areas ranged from 90 to 4,365 μm$^2$, while pore areas ranged from 154 to 6,637 μm$^2$ in humans. Mean elongations (± 1 standard deviation) were 1.77 ± 0.66 and 2.00 ± 0.75 in macaques and humans, respectively, while mean NND (± 1 standard deviation) was 36.9 ± 7.19 μm in monkeys and 69.1 ± 19.8 μm in humans.

Anterior laminar pore geometry was compared across imaging sessions to assess repeatability in imaging and quantifying the same pores at different times. Figure 2-5a-e presents montages of the temporal side of the anterior lamina cribrosa in a normal macaque (M057) from 5 separate imaging sessions that spanned the course of 128 days. Magnified views of the same region of the lamina cribrosa (denoted by the white box in the corresponding montages) are also shown in Fig. 2-5f-j for each session. Montages of the lamina cribrosa acquired in a normal human eye (H055) in four separate imaging sessions (spanning the course of 233 days) are similarly shown in Fig. 2-6. As seen in all of the larger montages and the magnified images, the same pores were clearly visible in each imaging session.

Using the montages acquired at different time-points, laminar pores were identified in each eye and laminar pore parameters were calculated and compared within and across imaging sessions. Table 2-2 summarizes the mean values of the standard deviations in pore area, elongation, and NND calculated after analyzing all pores multiple times within a single imaging session (i.e., intrasession) or after analyzing the same pores across all imaging sessions (i.e., intersession) in macaques and humans. Only pores that could be imaged and quantified at all time-points were included in the calculations of intersession variability. Therefore, 42 and 61 anterior laminar pores were included in monkey eyes M036 and M057, respectively, while 15, 22, and 35 were

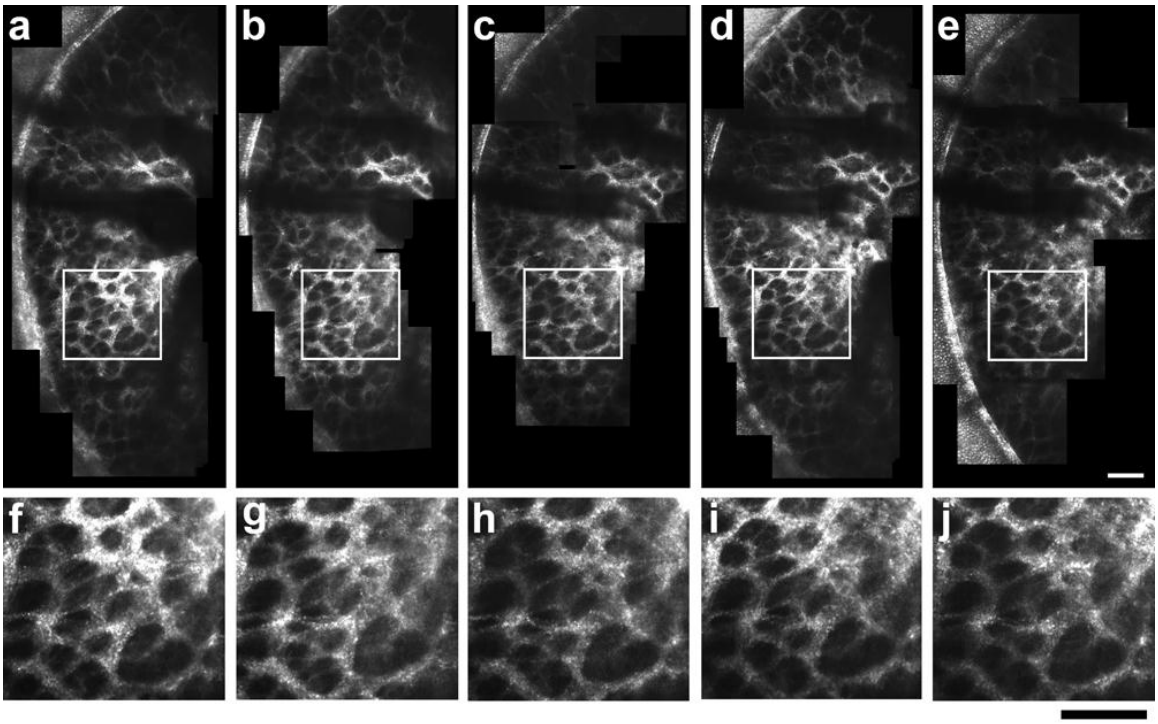


**Figure 2-5.** (a-e) Montages of the temporal side of the anterior lamina cribrosa taken in a normal macaque (M057) over 5 different imaging sessions (spanning 128 days). Vasculature overlying the laminar surface cast shadows on and obstruct the visualization of the underlying laminar pores. (f-j) Magnified images of the same patch of lamina denoted by the white squares in images (a-e). The same laminar pores could be imaged consistently across sessions. Scale bar: 100 μm.

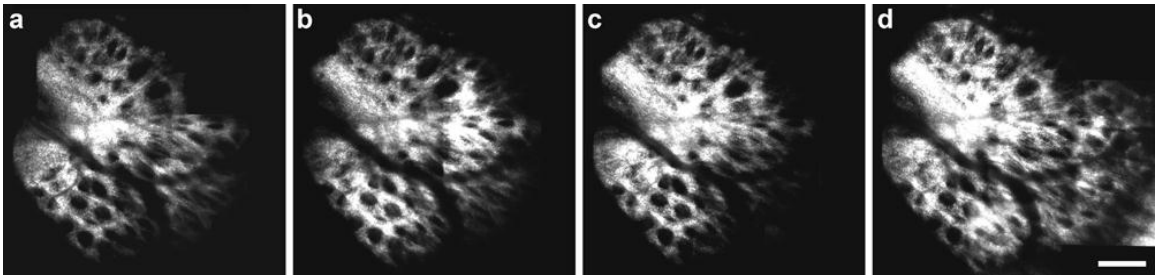


**Figure 2-6.** (a-d) Montages of the anterior lamina cribrosa taken in a normal human eye (H055) over 4 different imaging sessions (spanning 233 days). The same laminar pore structure could be imaged consistently across sessions. A slightly larger laminar area was imaged in (d) due to advances in our imaging methods. Scale bar: 200 μm.

**Table 2-2.** Mean standard deviations (SD) in anterior laminar pore geometry measured in normal macaque and human eyes within (i.e., intrasession) and across (i.e., intersession) imaging sessions.

| | SD of **Area** ($\mu m^2$) | | SD of **Elongation** | | SD of **NND** (μm) | |
|---|---|---|---|---|---|---|
| | Intra-session | Inter-session | Intra-session | Inter-session | Intra-session | Inter-session |
| Macaque | 13 (2.2%) | 50 (6.1%) | 0.04 (1.4%) | 0.13 (6.7%) | 0.10 (0.2%) | 1.93 (5.2%) |
| Human | 22 (0.9%) | 113 (8.3%) | 0.01 (0.5%) | 0.17 (7.7%) | 0.31 (0.2%) | 2.79 (4.1%) |

included in human eyes H058, H030, and H055, respectively. The mean variabilities in calculating nearly all pore parameters within and across sessions were slightly lower in macaques than in humans. The intrasession variability was typically much smaller than the intersession variability for all parameters (Table 2-2), indicating a consistent process for analyzing pore geometry. In macaques, the means of the standard deviations in pore area, elongation, and NND were 50 $\mu m^2$ (6.1% of a given pore's mean area), 0.13 (6.7% of a given pore's mean elongation), and 1.93 μm (5.2% of a given pore's mean NND), respectively. For humans, the means of the standard deviations in pore area, elongation, and NND across sessions were 113 $\mu m^2$ (8.3% of a given pore's mean area), 0.17 (7.7% of a given pore's mean elongation), and 2.79 μm (4.1% of a given pore's mean NND), respectively. There were no statistically significant differences in pore area, elongation, and NND across all imaging sessions for macaques and humans (ANOVA, $P>.05$), demonstrating good imaging and measurement repeatability.

### 2.4 Discussion

The AOSLO provided high-resolution, high-contrast images of the anterior surface of the lamina cribrosa in normal human and macaque eyes. The values of human laminar pore parameters measured *in vivo* in this study are comparable to *in vivo* and *ex vivo* data from previous reports. Mean laminar pore elongation measured using AOSLO imaging in our 3 normal human eyes (2.00 ± 0.75) was similar to that measured *in vivo* by Fontana et al. in 10 normal eyes using a confocal SLO (1.81 ± 0.1) (Fontana et al, 1998). Additionally, the range of human pore areas measured *in vivo* in this study (154 to 6,637 $\mu m^2$) is comparable to that found *ex vivo* by Quigley & Addicks (Quigley & Addicks, 1981) (range in pore diameter from 10 to 100 μm, or in pore area from ~79 to 7,850 $\mu m^2$ assuming circular pores) and by Dandona et al. (Dandona et al, 1990) in 9 normal histological samples sectioned midway between the anterior and posterior

laminar surfaces (range of 410 ± 35 $\mu m^2$ to 5,201 ± 621 $\mu m^2$ for the $10^{th}$ to $90^{th}$ percentiles). However, the range of pore areas we measured *in vivo* was less than that reported *ex vivo* by Ogden et al. (Ogden et al, 1988) (500 to 22,500 $\mu m^2$) and our mean pore area (1,713 ± 1,414 $\mu m^2$) was also less than that measured *ex vivo* by Jonas et al. (4,000 ± 1,000 $\mu m^2$) at the anterior laminar surface in 35 normal eyes (Jonas et al, 1991).

Many factors could account for the discrepancies in the range and mean values of pore areas between our *in vivo* measures in human eyes and the latter two *ex vivo* reports. Several postmortem studies support the idea that human laminar pores tend to be largest in the superior and inferior poles of the optic nerve head and increase in size towards the periphery of the nerve (Ogden et al, 1988; Quigley & Addicks, 1981). As mentioned earlier, it was difficult to image laminar pores *in vivo* at the superior and inferior poles in most eyes as the overlying vasculature (e.g., the central retinal artery and vein) typically obstructs the visualization of these pores. Additionally, the neuroretinal rim can cast shadows on to the anterior laminar surface, prohibiting the visualization of the most peripheral laminar pores in these circumstances. Therefore, it is possible that we did not image the largest laminar pores *in vivo* in all of our human eyes and that our measures of laminar pore area underestimate some of those found *ex vivo*.

Another possible confounding factor is that the *en face* AOSLO images represent a 2-dimensional projection of a potentially curved 3-dimensional anterior laminar surface. Strouthidis et al. recently demonstrated the ability to subjectively identify a contour representing the anterior laminar surface in a primate eye from a cross-sectional image of the ONH acquired using spectral domain OCT (Strouthidis et al, 2010). The position of the anterior laminar surface was not measured in our study eyes. Consequently, our AOSLO pore parameters may not represent the true anatomical shape of laminar pores in eyes with non-planar anterior laminar surfaces. While it is unknown the extent to

which a 3-dimensional transformation will alter our measured pore values, we do expect to see larger differences in eyes with more steeply curved anterior laminar surfaces. Therefore, our measured values could represent a lower bound for the true anatomical sizes imaged *in vivo*. Knowledge of absolute pore geometry may be important for biomechanical modeling of the anterior laminar surface. However, it may not be necessary for detecting changes in laminar pores during early experimental glaucoma in which one may be interested in detecting a relative change in pore structure in relation to the occurrence of changes in other clinical parameters conventionally used to diagnose and assess glaucoma.

Laminar pore parameters measured *in vivo* in our 2 normal non-human primate eyes can also be compared with the same values measured by Vilupuru et al. in 4 living macaque control eyes using a different AOSLO (Vilupuru et al, 2007). While both studies yielded comparable values of mean pore elongation in normal, control eyes (1.77 in the current study vs. ~1.6 in Vilupuru et al.), mean pore area and NND were larger in Vilupuru et al.'s study (~1,950 $\mu m^2$ and ~47 μm, respectively) than in the current study (973 $\mu m^2$ and 37 μm, respectively). The reasons for these discrepancies in pore area and NND are not clear. We do not know whether the resolution and confocality (e.g., pinhole diameter) of the AOSLO used in this study differed from that used by Vilupuru et al., potentially allowing us to better visualize and define the boundaries of smaller pores. Another possibility is that a different number of pores could have been analyzed in each study. Additionally, it is possible that these differences simply represent intersubject variability in laminar pore geometry given the small number of macaques imaged in this study (n=2) and by Vilupuru et al. (n=4). Attempts are currently underway to image anterior laminar pore parameters in a greater number of eyes to better define this issue in the normal macaque.

A main goal of this work was to examine the variability in our laminar pore

measurements over time. Because we wanted to assess the repeatability with which we could quantify the same laminar pores at each imaging time-point, we used a repeated measures ANOVA to assess the statistical variability in our measurements. A limitation of using a repeated measures ANOVA analysis is that one can only include pores that were quantified in all imaging sessions. For example, improvements in our imaging and quantification techniques typically enabled us to examine a greater extent of the laminar surface in a given eye over time, thereby allowing us (in general) to quantify a greater number of pores at the end of the experiment. (Fig. 6d represents an example in which we were able to image a greater extent of the laminar surface due to improved techniques.) However, even though an increased number of pores could often be visualized at later time-points, these additional pores were not included in the repeated measures ANOVA analysis for a given eye if they were not imaged at all earlier time-points. Additionally, while it was possible to measure and track the same laminar pores at multiple time-points, we excluded pores from the ANOVA analysis even if they were quantified in all but one session. As a result, the number of pores that were quantified and used to assess repeatability across all imaging sessions was less than the total number of pores used to generate the global statistics on mean pore area, elongation and NND in a given eye.

This study's method for imaging and quantifying anterior laminar pores using an AOSLO is repeatable in normal eyes. No statistically significant differences in pore geometry were found (ANOVA, $P>.05$) when comparing laminar pore parameters measured in the same eyes imaged over multiple time-points. Intrasession variability was also small (Table 2), demonstrating a consistent means for identifying pores. Mean pore area tended to have the largest measured intersession variability (Table 2, mean standard deviation of 8.3% in humans and 6.1% in macaques). This variability was likely due to small intensity differences between the AOSLO reflectance images acquired

across imaging sessions (potentially caused by slight differences in illumination levels, retinal reflectivity, PMT detector gain, etc.). For example, making only a half-pixel error in the identification of the entire boundary of the pores analyzed in this study would result in a 5.1% and 4.5% difference in mean pore area (on average) in humans and macaques, respectively. These values are not vastly dissimilar from our measured variabilities in mean pore area. Also, despite demonstrating good repeatability, the subjective methods used for demarcating and quantifying laminar pores can be very time-consuming and could be challenging to apply to the analysis of several eyes over short periods of time. We are currently developing algorithms to make this pore analysis method more objective and to decrease the required processing time through the use of semi-automated image processing techniques.

Even though it is possible to acquire excellent *en face* images of the anterior laminar surface in living eyes, AOSLO imaging is limited in its ability to visualize the entire laminar structure in 3 dimensions. Therefore, it will likely not be possible to use this technique to examine changes throughout the entire extent of the lamina in glaucoma. Nevertheless, it is still possible to visualize laminar pores over a finite range in depth behind the anterior laminar surface (Fig. 1) despite the AOSLO's limited axial resolution (Romero-Borja et al, 2005). Additionally, current models propose that changes in laminar thickness and position occur throughout the entire thickness of the lamina in early experimental glaucoma (Burgoyne & Downs, 2008). Therefore, changes in laminar pores should also occur at all depths, including the anterior surface, and be visible using AOSLO imaging.

In conclusion, we have established a repeatable method for relocating the same laminar pores and quantifying their geometries *in vivo* in normal human and non-human primate eyes. The methods presented in this chapter could be extended to assess longitudinal changes in laminar pore structure in glaucomatous neuropathy. These

measurements would contribute to a broader and more detailed understanding of the biomechanical properties of the normal and glaucomatous lamina while also enabling the correlation of laminar pore changes with functional and structural changes conventionally used to diagnose glaucoma.

### 2.5 Acknowledgements

The software used for the adaptive optics system in this research was partially developed by Alfredo Dubra-Suarez, funded by a Career Award from the Burroughs Wellcome Fund, and Kamran Ahmad, funded by NIH grant BRP-EY01437 and the NSF Science and Technology Center for Adaptive Optics. We thank Harold Bedell, Claude Burgoyne, Crawford Downs, Laura Frishman, and Michael Twa for their helpful discussions.

# CHAPTER 3

## *In vivo* comparison of lamina cribrosa microarchitecture and optic nerve head structure between fellow eyes of normal non-human primates

**Contributing authors:**

Nripun Sredar, Nimesh B. Patel, OD, PhD, Hope M. Queener, Michael D. Twa, OD, PhD, Ronald S. Harwerth, OD, PhD, and Jason Porter, PhD

**Abstract**

**Purpose:** To compare anterior lamina cribrosa surface (ALCS) microarchitecture and optic nerve head (ONH) structure *in vivo* between fellow eyes in normal non-human primates.

**Methods:** Bruch's Membrane Opening (BMO) area, mean ALCS depth (ALCSD), and mean minimum rim width (MRW) were calculated from spectral domain optical coherence tomography images of the ONH acquired *in vivo* in fellow eyes of 6 normal rhesus monkeys. Mean ALCS pore parameters were calculated from 3D transformed adaptive optics scanning laser ophthalmoscope images. Laminar pore parameters (calculated globally, within 60° sectors, and centrally versus peripherally) and ONH parameters were compared between fellow eyes.

**Results:** Mean differences in BMO area, ALCSD, and MRW between fellow eyes ($0.07 \pm 0.05$ mm$^2$, $10.0 \pm 6.9$ µm, and $7.9 \pm 6.7$ µm, respectively) were not statistically significant ($P>.05$). There were no significant inter-eye differences in mean global pore area for 4 monkeys, elongation for all monkeys, and nearest neighbor distance (NND) for 3 monkeys ($P>.05$). Inter-eye differences in mean pore area and NND existed between superotemporal sectors in 2 monkeys and between temporal sectors in 2 monkeys. Laminar pores were significantly spatially colocalized based on pore area, elongation, and NND in the majority of eyes ($P<.05$).

**Conclusions:** ONH parameters were similar between fellow eyes of normal monkeys. The few inter-eye differences in pore parameters could be explained by differences in the regions imaged or the number of pores marked between eyes. These values will serve as normative ONH and laminar pore data for future studies in experimental

glaucoma.

### 3.1 Introduction

The lamina cribrosa is a three-dimensional porous structure largely composed of flexible beams of collagenous tissue that support and nourish retinal ganglion cell (RGC) axon bundles passing from the retina toward the brain. Substantial evidence indicates that the first site of axonal injury in glaucoma occurs at the lamina cribrosa in the optic nerve head (ONH) (Anderson & Hendrickson, 1974; Anderson & Hendrickson, 1977; Howell et al, 2007; Minckler & Spaeth, 1981; Quigley & Addicks, 1980; Quigley et al, 1982; Quigley & Anderson, 1976; Quigley & Anderson, 1977; Quigley et al, 1980; Quigley et al, 1979; Quigley et al, 1983). Studies have shown that additional stress from increased intraocular pressure (IOP) can strain or deform the lamina (Bellezza et al, 2000; Roberts et al, 2010; Sigal et al, 2004), resulting in biomechanical alterations to the load-bearing laminar beams (Bellezza et al, 2003; Downs et al, 2008), changes in laminar pore geometry (Vilupuru et al, 2007), and possible damage to laminar capillaries (Burgoyne et al, 2005) and astrocytes (Hernandez, 2000) that could compromise axonal function (Anderson, 1969; Anderson & Hendrickson, 1974; Anderson & Hendrickson, 1977; Quigley & Anderson, 1976; Quigley & Addicks, 1980; Quigley & Anderson, 1977; Quigley et al, 1979).

An increasing number of studies have compared the structure of the ONH and lamina cribrosa between normal and glaucomatous eyes in human patients and between control and experimental glaucoma eyes in non-human primates. Histological data from non-human primates has shown an overall thickening of the lamina cribrosa and a posterior deformation of the laminar surface (i.e., increase in anterior lamina cribrosa surface depth [ALCSD]) in eyes with early experimental glaucoma compared to normal control eyes at the same time point (Bellezza et al, 2003; Burgoyne et al, 2004; Yang et al, 2007b). Similar increases in ALCSD have also been observed *in vivo* in longitudinal studies of non-human primate eyes with early experimental glaucoma relative to fellow

control eyes and in cross-sectional studies of human glaucoma patients relative to normal eyes (Furlanetto et al, 2013; Strouthidis et al, 2011b). In addition, differences in global lamina cribrosa pore geometry have been quantified *in vivo* between non-human primate eyes with experimental glaucoma and their fellow control eyes (e.g., larger pore area in glaucoma eyes), as well as between glaucomatous and normal eyes of human patients in cross-sectional studies (e.g., larger pore diameter standard deviation in glaucoma eyes) (Akagi et al, 2012; Wang et al, 2013). However, an implicit assumption in studies that select one eye from each subject at a single time-point or compare parameters between a diseased eye and its fellow control eye is that the parameters being examined are similar between fellow eyes of the same subject. Therefore, it is important to have a more thorough understanding of the normal variability inherent in these parameters between fellow eyes, particularly when examining subtle changes or differences that occur in the earliest stages of disease.

Few studies have reported the variability in ONH and global lamina cribrosa geometry between normal, fellow eyes. Yang et al. studied inter-eye differences in ONH geometry using histomorphometric reconstructions from six normal monkeys. The physiologic inter-eye percent differences in optic disc area, ONH connective tissue (lamina cribrosa position and thickness), and ONH prelaminar neural tissue (prelaminar tissue thickness and volume) were found to be relatively small (i.e., no more than 3% to 21%, depending on the parameter) (Yang et al, 2009). Roberts et al. reported extensive regional variation in laminar microarchitecture within normal monkey eyes and markedly similar lamina cribrosa connective tissue volume fractions between contralateral eyes of normal monkeys *ex vivo* (Roberts et al, 2009). While the aforementioned studies examined global and regional laminar geometry, there is a general lack of *in vivo* or *ex vivo* data that characterizes the degree of variability inherent in lamina cribrosa beams or pores between fellow normal eyes on global or local spatial scales.

We have assessed differences in anterior lamina cribrosa pore and ONH structure between fellow eyes of six normal non-human primates *in vivo* using adaptive optics scanning laser ophthalmoscope (AOSLO) and spectral domain optical coherence tomography (SDOCT) imaging. Statistical tests were performed to investigate whether significant differences were present in lamina cribrosa pore and ONH structure within individual eyes and between fellow eyes on global and local levels. This study quantifies and provides a better understanding of the variability in ONH geometry and lamina cribrosa microarchitecture between fellow eyes of normal monkeys and will be used for future inter-eye comparisons with non-human primate eyes with unilateral laser-induced experimental glaucoma.

### 3.2 Methods

All animal care experimental procedures were approved by the University of Houston's Institutional Animal Care and Use Committee and adhered to the ARVO Statement for the Use of Animals in Ophthalmic and Vision Research.

The anterior lamina cribrosa and ONH were examined *in vivo* in left and right eyes of 6 normal rhesus monkeys (*Macaca mulatta*) with a mean age of 2.8 ± 0.9 years. Monkeys were anesthetized with 20-25 mg/kg ketamine, 0.8-0.9 mg/kg xylazine, and 0.04 mg/kg atropine sulfate to minimize eye movements during *in vivo* imaging (Frishman et al, 1996). Monkey pupils were dilated with 2.5% phenylephrine and 1% tropicamide. A lid speculum was used to hold the monkey eyelid open and a contact lens was placed on the monkey eye to prevent corneal dehydration during imaging. A head mount with tip, tilt, and rotation capabilities was used to stabilize the monkey's head during SDOCT imaging. The head mount was also attached to an XYZ translation stage to align the eye's pupil with the AOSLO system for laminar imaging.

### *3.2.1 Biometric measurements and image scaling*

An ocular biometer (IOLMaster; Carl Zeiss Meditec, AG, Jena, Germany) was used to measure axial length, anterior chamber depth, and anterior corneal curvature in all eyes. These biometric measurements [along with previously published measurements of lens thickness and curvatures corresponding to each monkey's age (Qiao-Grider et al, 2007)] were incorporated into a three-surface model eye to laterally scale SDOCT and AOSLO images by converting angular units into physical units (i.e., micrometers) (Ivers et al, 2011).

### *3.2.2 Spectral domain optical coherence tomography (SDOCT) imaging and analysis*

Scanning laser ophthalmoscope (SLO) images of the ONH (30° x 30°) were acquired by a clinical instrument based on SDOCT (Spectralis HRA+OCT; Heidelberg Engineering, Heidelberg, Germany). Cross-sectional radial scans (20° field, 48 B-scans) centered on the ONH were acquired in each eye using the same SDOCT instrument. The termination of the retinal pigment epithelium (RPE)/Bruch's membrane (BM) interface and the anterior lamina cribrosa surface (ALCS) were manually marked using a custom program (MATLAB; The MathWorks, Inc., Natick, MA) in as many B-scans as possible (Fig. 3-1) to determine the area of Bruch's membrane opening (BMO; area of an ellipse best fit to the marked RPE/BM termination points) and mean ALCS depth (ALCSD; mean perpendicular distance between a thin-plate spline surface fit to the marked ALCS points and the plane best fit to the BMO) (Fig. 3-2b) for each eye (Sredar et al, 2013). The internal limiting membrane (ILM) was automatically segmented in each B-scan

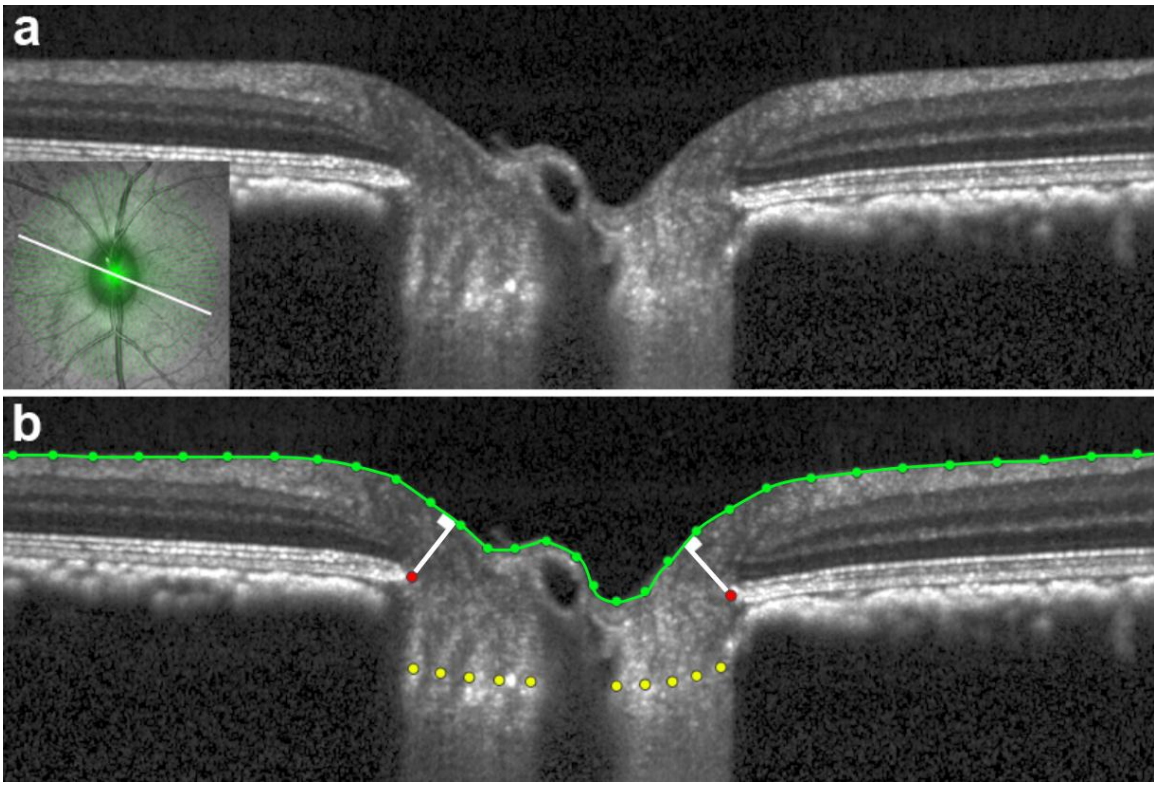


**Figure 3-1.** ONH features were marked in as many B-scans as possible. (a) A single SDOCT radial B-scan of the ONH and lamina cribrosa acquired from the left eye of a normal monkey, M088 (scan location denoted by the bold white line in the inset). The inset (lower left corner) shows the corresponding *en face* SLO image of the ONH and location of all radial B-scans (green lines) acquired in the same eye. (b) The same B-scan as in (a) with manually marked ONH features, including the termination points of the RPE/BM interface (red dots) and ALCS (yellow dots), and the semi-automatically segmented ILM (green dots and green line). The minimum distance from each termination point of the RPE/BM interface to the ILM was calculated on each side of the neural canal opening (white lines) in each B-scan. Mean MRW was computed as the average of all minimum widths across all B-scans.

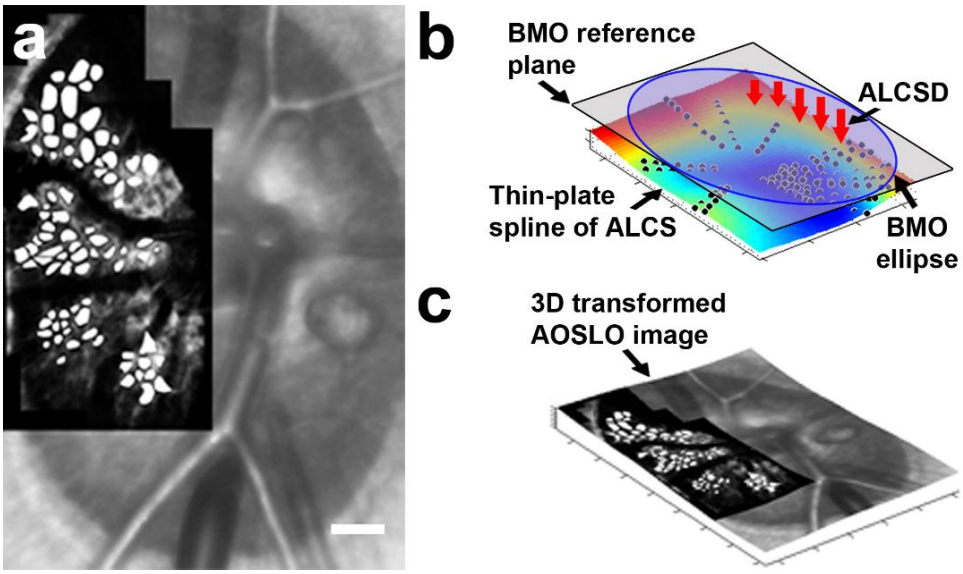


**Figure 3-2.** Laminar pore and ONH geometry were quantified from AOSLO and SDOCT images. (a) A 2D AOSLO image showing marked anterior lamina cribrosa surface pores (white) overlaid on the SLO image from the same normal eye (M067). Scale bar: 150 µm. (b) BMO area was calculated as the area encompassed by the best-fit BMO ellipse (blue line) on the BMO plane (gray). A thin-plate spline surface was fit to the marked ALCS points (black dots) in 3D and used to calculate mean ALCSD (red arrows) from the BMO plane. (c) 3D transformed AOSLO image of the ALCS following registration and projection of the 2D AOSLO image from (a) onto the 3D thin-plate spline surface from (b). Pores were quantified from the 3D transformed images to better represent the physiological laminar surface structure.

using the SDOCT instrument software (Fig. 3-1b) and any inaccuracies were manually corrected. The minimum distances from each RPE/BM termination point to the ILM were calculated in all B-scans (Fig. 3-1b) and averaged to compute the mean minimum rim width (MRW). Mean absolute inter-eye differences in these three parameters were calculated as the average of the absolute differences of each parameter between left and right eyes of all monkeys.

### *3.2.3 Adaptive optics scanning laser ophthalmoscope (AOSLO) imaging and analysis*

The methods used for AOSLO imaging were essentially as described previously (Ivers et al, 2011). In brief, adaptive optics correction and reflectance imaging were performed over a dilated pupil (~8 mm) using an 840 nm superluminescent diode (S-Series Broadlighter, Superlum, Carrigtwohill, Ireland) with a power of ~300 μW at the cornea. Through-focus videos were acquired within the ONH (1.5° field, 25 Hz) to determine the plane at which the ALCS was best-focused. Videos of the ALCS were subsequently recorded at the plane of best-focus throughout as much of the ONH as possible. Registered images were created from each video using a custom MATLAB program and combined to generate a montage of the ALCS in each eye (Fig. 3-2a) (Adobe Photoshop; Adobe Systems, San Jose, CA).

Pores were manually marked (Adobe Photoshop) using previously described methods found to have excellent repeatability and reproducibility (Ivers et al, 2011). The area, elongation (ratio of the major to minor axis of an ellipse best fit to the pore), and nearest neighbor distance (NND) of each marked pore were quantified in each montage. Due to the fact that AOSLO images of the ALCS represent a projected view of the 3D laminar surface, 2D AOSLO images were transformed into their approximate 3D configuration by registering and projecting AOSLO images onto the 3D thin-plate spline

surface fit to the marked ALCS points (Fig. 3-2c) (Sredar et al, 2013). Following 3D transformation, laminar pore parameters were analyzed globally, regionally (central vs. peripheral), and within 60° sectors within each eye and between fellow eyes. Pores were classified as being centrally or peripherally located by dividing the area defined by the BMO ellipse into central and peripheral regions of equal areas. For sector analyses, meridians were constructed at 60° intervals from the major axis of the BMO ellipse. If a pore crossed a sector or central/peripheral dividing boundary, the pore was included in the region which contained its centroid.

### *3.2.4 Statistical analysis*

A paired t-test was used to compare BMO area, mean ALCSD, and mean MRW between fellow eyes. The Mann-Whitney rank sum test, a non-parametric test, was used to compare and assess statistically significant differences in laminar pore parameters within individual eyes and between fellow eyes. Pore area, elongation, and NND were compared globally between fellow eyes. Pore parameters were also compared between regions (central vs. peripheral) and sectors (superotemporal vs. temporal vs. inferotemporal) within individual eyes. In addition, pore parameters were compared between fellow eyes on region-by-region (e.g., central region in one eye vs. central region in the fellow eye) and sector-by-sector (e.g., temporal sector in one eye vs. temporal sector in the fellow eye) bases. If it was not possible to image and mark any pores within a given region or sector, statistical comparisons were not conducted for that particular region or sector in the given eye. *P* values <.05 were taken to represent statistically significant differences for all comparisons.

Cluster analysis and the Moran's I spatial autocorrelation statistical test were performed to compare the spatial arrangement of marked pores within each eye. Pores were clustered into 1 of 3 bin sizes (small, medium, or large) in each eye depending on

the magnitude of the parameter being evaluated (e.g., pore area) (Orange; Bioinformatics Laboratory, University of Ljubljana, Slovenia) (Demsar et al, 2013). The selection of three bins allowed for an optimal separation of the data and best ensured that neither too many pores were grouped into too few bins nor that too few pores were grouped into too many bins. The range of values contained within each bin was determined such that the mean value of the analyzed parameter within a given bin (e.g., large area pores) was maximally separated from the mean value of the next nearest bin (e.g., medium area pores). A Moran's I statistical test was then performed on all marked pores in each eye (R; Institute for Digital Research and Education, University of California Los Angeles, CA) to determine whether a statistically significant local spatial pattern existed for pores based on the values of the examined parameter (e.g., pore area). For example, when examining pore area, pores that were colocated with pores of very similar area would have a high positive correlation (+1 indicates perfect spatial correlation; e.g., all large pores clustered in one region/sector and all small pores clustered in a different region/sector), whereas pores that were adjacent to pores of dissimilar area would result in a more negative Moran's I index value, suggesting increased spatial dispersion (-1 indicates perfect spatial dispersion; e.g., periodic alternation of large, medium, and small sized pores throughout the ALCS) (Moran, 1950). A Moran's I index value near 0 indicates a random spatial arrangement of pore areas where there is no discernable clustering. The cluster analysis and Moran's I test were performed to investigate the spatial arrangement of pores based on all pore parameters (area, elongation, and NND). A *P* value was calculated to determine the statistical significance of the Moran's I index value. *P* values < .05 were taken to represent a significant spatial autocorrelation in pores based on their pore parameter.

### 3.3 Results

Maximum intensity projection images made from all SDOCT B-scans acquired in each eye are shown in Fig. 3-3 for all 6 normal monkeys. Orange dots represent the collection of ALCS points marked in all B-scans while the red lines indicate the locations of the BMO reference plane. The BMO area, mean ALCSD, and mean MRW values calculated from these marked scans were very similar between left and right eyes of each monkey (Table 3-1). Mean absolute inter-eye differences in BMO area, mean ALCSD, and mean MRW across all 6 normal monkeys were 0.07 ± 0.05 $mm^2$ (5.2 ± 3.5 %), 10.0 ± 6.9 µm (5.3 ± 3.8 %), and 7.9 ± 6.7 µm (3.1 ± 2.5 %), respectively. A paired t-test revealed no statistically significant differences in any of these ONH parameters between fellow eyes across all monkeys ($P$>.05).

High-resolution AOSLO images of the anterior lamina cribrosa surface are shown overlaid on the corresponding SLO images in Fig. 3-4 (rows 1, 3, and 5) for all left and right eyes. The pores that were manually marked in each montage are shown in the images directly below each raw AOSLO/SLO image (Fig. 3-4, rows 2, 4, and 6). Mean (± SD) global ALCS pore area, elongation, and NND across all right eyes were 1023 ± 201 $\mu m^2$, 1.65 ± 0.04, and 41.8 ± 3.6 µm, respectively, and 1120 ± 227 $\mu m^2$, 1.68 ± 0.05, and 41.4 ± 4.5 µm, respectively, across all left eyes (Table 3-2). Globally, statistically significant differences in laminar pore parameters were found between fellow eyes in two monkeys (M070 and M072) for pore area, in no monkeys for pore elongation, and in three monkeys (M066, M070, and M072) for pore NND ($P$<.05) (Table 3-3).

In addition to global comparisons, pores were segmented into regions of equal area (central and peripheral) and into 60° sectors in all eyes in order to better compare anterior laminar surface pore parameters on a local level within eyes (Fig. 3-4, rows 2, 4, 6). While mean pore area was smaller centrally vs. peripherally across all right eyes (971 ± 187 $\mu m^2$ vs. 1122 ± 261 $\mu m^2$) and all left eyes (1032 ± 136 $\mu m^2$ vs. 1315 ± 587 $\mu m^2$)

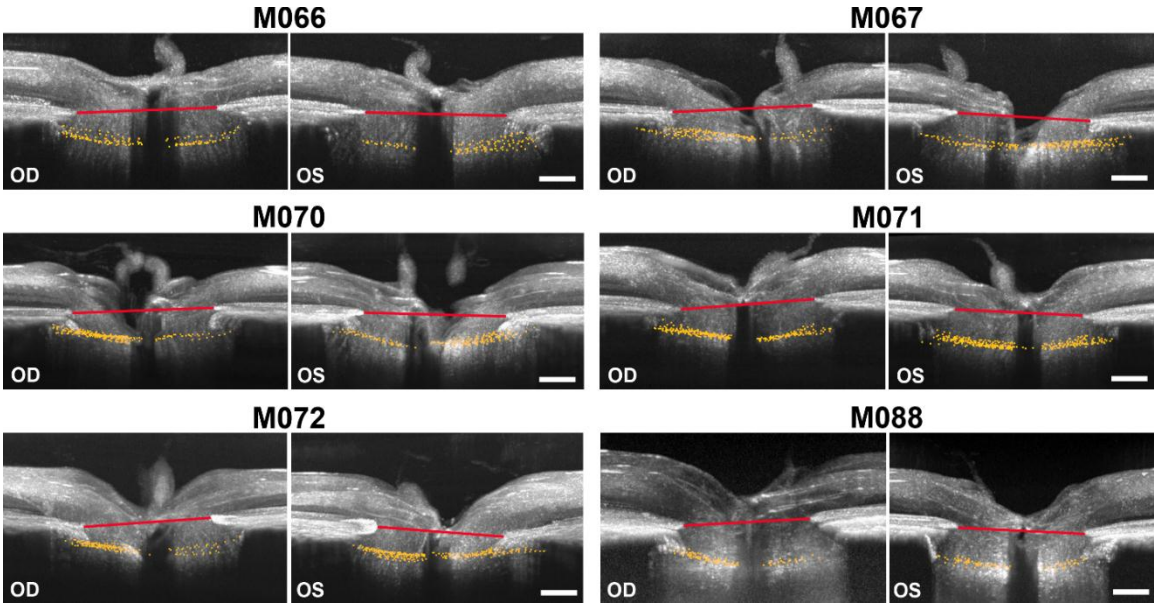


**Figure 3-3.** SDOCT maximum intensity projection images from all B-scans acquired in right and left eyes of 6 normal monkeys. Marked ALCS points from all scans are shown using orange dots and the BMO reference plane is represented using a red line. BMO area and mean ALCSD did not differ significantly between fellow eyes for all 6 monkeys (*P*>.05). Scale bar: 300 µm.

**Table 3-1.** ONH parameters in fellow eyes of normal monkeys and mean intereye differences.

| | BMO Area ($mm^2$) | | Mean ALCSD (μm) | | Mean MRW (μm) | |
|---|---|---|---|---|---|---|
| **Monkey** | **OD** | **OS** | **OD** | **OS** | **OD** | **OS** |
| M066 | 1.58 | 1.61 | 191.6 ± 36.2 | 202.4 ± 29.0 | 281.8 ± 49.8 | 284.5 ± 48.3 |
| M067 | 1.59 | 1.57 | 175.5 ± 32.7 | 193.2 ± 23.0 | 242.8 ± 54.7 | 238.4 ± 45.0 |
| M070 | 1.39 | 1.52 | 177.8 ± 30.9 | 195.2 ± 39.0 | 232.7 ± 58.5 | 222.0 ± 57.2 |
| M071 | 1.35 | 1.31 | 202.0 ± 32.3 | 206.4 ± 24.1 | 249.9 ± 55.3 | 257.1 ± 65.2 |
| M072 | 1.28 | 1.40 | 199.3 ± 53.5 | 190.0 ± 41.8 | 299.1 ± 45.5 | 301.3 ± 66.7 |
| M088 | 1.39 | 1.49 | 206.6 ± 34.6 | 206.1 ± 25.6 | 283.7 ± 55.2 | 263.8 ± 53.3 |
| **Mean** | 1.43 ± 0.13 | 1.48 ± 0.11 | 192.1 ± 13.0 | 198.9 ± 7.0 | 265.0 ± 26.7 | 261.2 ± 29.1 |
| **Mean Intereye Difference** | 0.07 ± 0.05 $mm^2$ (5.2 ± 3.5%) | | 10.0 ± 6.9 μm (5.3 ± 3.8%) | | 7.9 ± 6.7 μm (3.1 ± 2.5%) | |

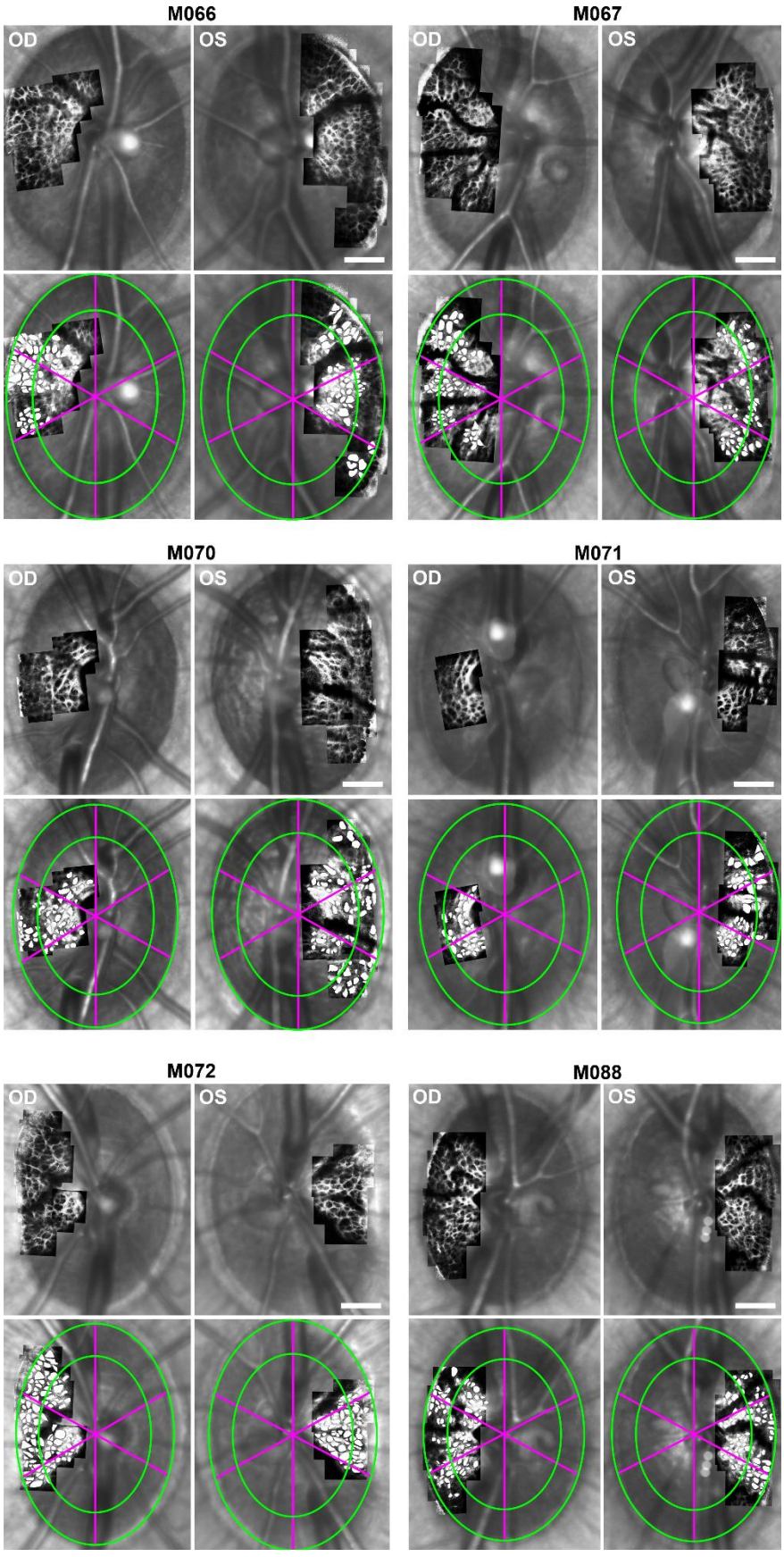
M066
OD
OS
M067
OD
OS
M070
OD
OS
M071
OD
OS
M072
OD
OS
M088
OD
OS

**Figure 3-4.** Laminar pore parameters were analyzed on global and local levels in all eyes. (Rows 1, 3, 5) AOSLO montages of the anterior lamina cribrosa surface scaled, registered, and overlaid on the corresponding SLO images in right and left eyes of 6 normal monkeys. (Rows 2, 4, 6) After manually marking laminar pores (filled in white) in each montage, pores were examined globally, in central and peripheral regions (separated by green boundaries) and in 60° sectors (divided by fuchsia meridians). Scale bar: 100 μm.

**Table 3-2.** Mean (± SD) pore parameters across all eyes of 6 normal monkeys on global, regional, and sector scales.

| | Mean Pore Area (μm²) | | Mean Pore Elongation | | Mean Pore NND (μm) | |
|---|---|---|---|---|---|---|
| | **OD** | **OS** | **OD** | **OS** | **OD** | **OS** |
| Global | 1023 ± 201 | 1120 ± 227 | 1.65 ± 0.04 | 1.68 ± 0.05 | 41.8 ± 3.6 | 41.4 ± 4.5 |
| Central | 971 ± 187 | 1032 ± 136 | 1.64 ± 0.07 | 1.66 ± 0.05 | 40.0 ± 2.5 | 40.6 ± 4.4 |
| Peripheral | 1122 ± 261 | 1315 ± 587 | 1.65 ± 0.10 | 1.74 ± 0.10 | 39.3 ± 4.1 | 44.1 ± 7.2 |
| Superotemporal | 1179 ± 239 | 1122 ± 312 | 1.67 ± 0.09 | 1.66 ± 0.05 | 46.4 ± 8.6 | 43.9 ± 6.0 |
| Temporal | 932 ± 250 | 1147 ± 348 | 1.70 ± 0.06 | 1.76 ± 0.11 | 38.1 ± 3.0 | 40.4 ± 4.4 |
| Inferotemporal | 964 ± 169 | 1229 ± 428 | 1.55 ± 0.12 | 1.55 ± 0.08 | 39.6 ± 1.8 | 42.6 ± 6.8 |

**Table 3-3.** Mean percent differences in ALCS pore parameters between fellow eyes of 6 normal monkeys on global, regional, and sector scales.

| Parameter | Monkey | Global | Central | Peripheral | Supero-temporal | Temporal | Infero-temporal |
|---|---|---|---|---|---|---|---|
| Area | M066 | 8.6% | 2.6% | 23.7% | 5.7% | 9.2% | -- |
| | M067 | 4.2% | 18.2% | 10.5% | 18.3% | 40.0%* | 3.1% |
| | M070 | 42.3%* | 29.3% | 56.0%* | 48.6% | 40.9%* | 39.2% |
| | M071 | 27.2% | 7.0% | -- | 14.7% | 44.8% | 4.8% |
| | M072 | 25.0%* | 12.8% | 64.3%* | 76.3%* | 7.6% | 26.1% |
| | M088 | 4.4% | 3.3% | 1.6% | 11.2% | 12.7% | 10.3% |
| Elongation | M066 | 3.0% | 0.0% | 8.7% | 3.0% | 5.9% | -- |
| | M067 | 6.1% | 11.3% | 2.9% | 6.8% | 1.2% | 15.9% |
| | M070 | 4.3% | 3.6% | 11.6% | 6.8% | 8.6% | 5.3% |
| | M071 | 3.0% | 3.0% | -- | 6.4% | 7.5% | 1.3% |
| | M072 | 0.6% | 2.4% | 11.0% | 5.9% | 1.7% | 11.5% |
| | M088 | 6.1% | 6.8% | 2.4% | 7.4% | 4.3% | 8.5% |
| NND | M066 | 12.4%* | 1.6% | 21.7%* | 10.4% | 6.1% | -- |
| | M067 | 6.2% | 21.1% | 8.5% | 2.9% | 19.3%* | 1.8% |
| | M070 | 15.1%* | 1.0% | 47.7%* | 4.7% | 16.5% | 8.1% |
| | M071 | 3.7% | 2.8% | -- | 32.5%* | 6.3% | 5.5% |
| | M072 | 12.8%* | 11.0% | 12.7% | 27.4%* | 7.5% | 17.6% |
| | M088 | 6.9% | 3.6% | 7.7% | 10.5% | 6.0% | 16.0% |

‘--’ no marked pores in the specified region or sector for inter-eye comparison.

‘*’ statistically significant difference between fellow eyes ($P$<.05).

(Table 3-2), statistically significant differences were found between these two regions in only 2 of 12 eyes (M070, OS; M071, OS) (Mann-Whitney rank sum test, $P<.05$). Pore elongation was not significantly different between central and peripheral regions in all eyes while pore NND was significantly larger in the peripheral region in 2 eyes (M071, OS; M088, OD). On a sector level, pore area was significantly larger in the superotemporal and/or inferotemporal sectors compared to the temporal sector in 4 eyes (M066, OS; M067, OD; M072, OS; M088, OD). Pore NND was also significantly larger in the superotemporal and/or inferotemporal sectors compared to the temporal sector in 6 eyes (M066, OS; M067, OD; M070, OD; M071, OD; M072, OS; M088, OS), while pore elongation was significantly larger in the temporal sector compared to the superotemporal and inferotemporal sectors in 3 eyes (M070, OS; M071, OD and OS).

The mean percent differences in pore area, elongation, and NND between left and right eyes of all 6 normal monkeys are shown in Table 3-3 on global, regional, and sector scales. Overall, few statistically significant differences in anterior laminar pore parameters were measured between left and right eyes on global (5/18 cases), regional (4/33 cases), or sector (6/51 cases) bases. When comparing central regions between fellow eyes in all monkeys, no statistically significant differences were found in any pore parameter ($P>.05$). However, in peripheral regions, pore area and NND were significantly different between fellow eyes in M070, while pore area was significantly different in M072 and pore NND was significantly different in M066 ($P<.05$). When comparing pore parameters in the superotemporal sector between fellow eyes, pore area and NND differed significantly in M072 while pore NND differed significantly in M071. In the temporal sector, pore area and NND differed significantly between fellow eyes in M067 and pore area differed significantly in M070. However, no significant differences in any pore parameters were measured in the inferotemporal sector. Moreover, there were no significant differences in pore elongation between fellow eyes

of all subjects on regional and sector levels.

A cluster analysis was performed in each eye to examine the spatial arrangement of ALCS pores based on their area, elongation, and NND. Figure 3-5 shows a range of distributions of ALCS pores classified as having large (red), medium (blue), and small (yellow) areas in 3 monkey eyes. Mean pore areas for these three clustered bins ranged from 1,183.1 $\mu m^2$ to 4,480.0 $\mu m^2$ for large pores, 532.8 $\mu m^2$ to 2,277.6 $\mu m^2$ for medium pores, and 65.2 $\mu m^2$ to 1,105.6 $\mu m^2$ for small pores across all eyes (Table 3-4). Significant positive spatial autocorrelations in pore area ($P$<.05) were found in 6 of 12 eyes (Table 3-5) where pores of similar area tended to be more spatially clustered (such as monkey M067 in Fig. 3-5c). The remaining 6 eyes had non-significant Moran's I indices that were approximately 0, where pores were more randomly arranged based on their area (such as monkeys M071 and M070 in Figs. 3-5a,b). In addition, 7 of 12 eyes had a significant positive spatial autocorrelation ($P$<.05) based on pore elongation (Table 3-5), indicating that pores of similar shape tended to be more spatially co-located in these eyes. A significant positive spatial autocorrelation ($P$<.05) based on pore NND was found in 11 of 12 eyes (Table 3-5), indicating that pores of similar spacing tended to be more spatially clustered in nearly all eyes.

### 3.4 Discussion

It is important to understand the variability in ONH and lamina cribrosa geometry between normal fellow eyes prior to examining differences in these structures between control and glaucomatous eyes. The values of BMO area and mean ALCSD measured between fellow eyes in this study are similar to those measured *ex vivo* in six normal monkey eyes by Yang et al (Yang et al, 2009). Mean BMO areas measured *in vivo* using SDOCT in right and left eyes of all normal monkeys (1.43 ± 0.13 $mm^2$ and 1.48 ± 0.11 $mm^2$, respectively) and the mean inter-eye difference (0.07 $mm^2$) were

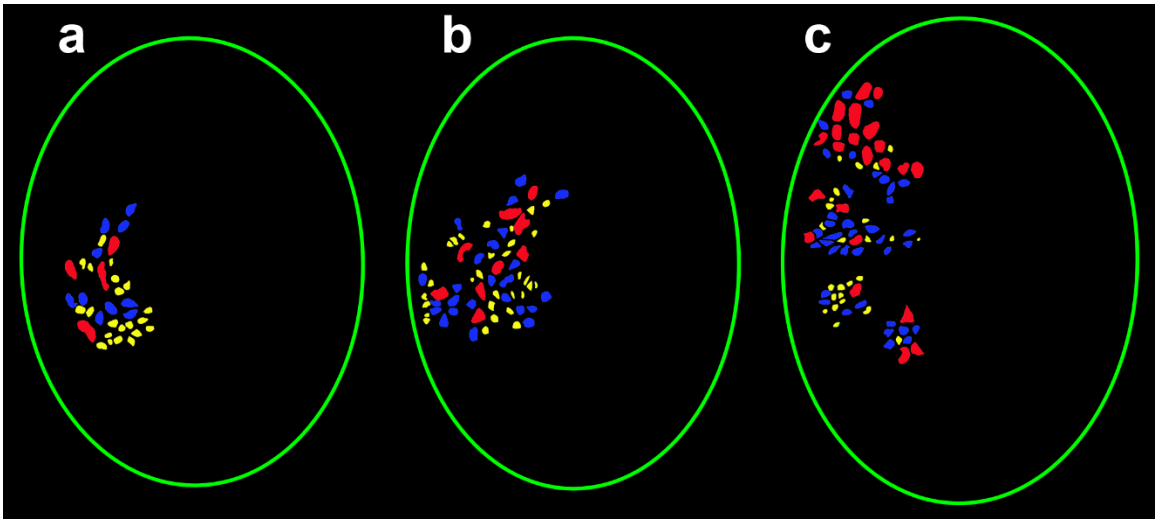


**Figure 3-5.** Images of the spatial arrangements of marked ALCS pores (as classified by their area) in 3 monkey eyes. Green lines represent the BMO ellipse. Pores were classified as having large (red), medium (blue), and small (yellow) areas in each eye via cluster analysis. (a) Pores in the right eye of monkey M071 had the largest negative spatial autocorrelation of all eyes based on pore area, though it was not statistically significant (Moran's I index = -0.02, *P*=.97). (b) Pores in the right eye of monkey M070 had a non-statistically significant negative spatial autocorrelation based on their area (Moran's I index = -0.01, *P*=.54), indicating a slightly more random spatial distribution of pores according to their area. (c) Pores in the right eye of monkey M067 had the largest positive spatial autocorrelation of all eyes based on pore area that was also statistically significant (Moran's I index = 0.11, *P*<.05). A higher degree of spatial clustering of pores with similar area (or color) was observed in this eye.

**Table 3-4.** Range of values for mean pore parameters across all eyes after being clustered into three bin sizes (small, medium, and large).

| | Mean Pore Area ($\mu m^2$) | | | Mean Pore Elongation | | | Mean Pore NND (μm) | | |
|---|---|---|---|---|---|---|---|---|---|
| | **Small** | **Medium** | **Large** | **Small** | **Medium** | **Large** | **Small** | **Medium** | **Large** |
| **Minimum** | 65.2 | 532.8 | 1183.1 | 1.02 | 1.38 | 1.86 | 18.6 | 29.4 | 40.0 |
| **Mean** | 544.5 | 1148.9 | 2163.6 | 1.33 | 1.78 | 2.56 | 31.1 | 43.9 | 55.6 |
| **Maximum** | 1105.6 | 2277.6 | 4480.0 | 1.61 | 2.60 | 4.44 | 44.5 | 74.7 | 146.4 |

**Table 3-5.** Moran's I index values obtained from spatial autocorrelation analyses in both eyes of 6 normal monkeys.

| | Pore Area | | Pore Elongation | | Pore NND | |
|---|---|---|---|---|---|---|
| **Monkey** | **OD** | **OS** | **OD** | **OS** | **OD** | **OS** |
| M066 | 0.01 | 0.08* | 0.02* | 0.01 | 0.04* | 0.06* |
| M067 | 0.11* | -0.02 | 0.03* | 0.01 | 0.20* | 0.01 |
| M070 | -0.01 | 0.01 | 0.05* | 0.01 | 0.13* | 0.06* |
| M071 | -0.02 | 0.09* | 0.03* | 0.04* | 0.09* | 0.04* |
| M072 | 0.01 | 0.04* | 0.02* | -0.02 | 0.05* | 0.03* |
| M088 | 0.05* | 0.03* | 0.00 | 0.02* | 0.08* | 0.11* |

'*' statistically significant spatial autocorrelation ($P<.05$).

comparable to mean BMO areas measured by Yang et al. in right and left eyes (1.37 ± 0.34 $mm^2$ and 1.26 ± 0.17 $mm^2$, respectively) and their mean inter-eye difference (0.02 $mm^2$). In addition, the range of inter-eye differences in mean ALCSD measured *in vivo* in this study (2 to 20 μm) was similar to that reported by Yang et al. (6 to 16 μm) (Yang et al, 2009). Moreover, to our knowledge, we report the first comparison of mean MRW values between fellow eyes of normal monkeys and found no statistically significant inter-eye differences in all monkeys. Understanding the normal variability inherent in mean MRW is important due to the fact that changes in MRW could precede changes in RNFLT in the earliest stages of glaucoma (Chauhan & Burgoyne, 2013; Fortune et al, 2013).

In addition to comparing ONH parameters between fellow eyes, we also report the first *in vivo* comparison of ALCS pore parameters between fellow normal eyes on global and local spatial scales. The mean global laminar pore parameters quantified in this study after 3D transformation (area: 1,072 ± 303 $\mu m^2$, elongation: 1.67 ± 0.06, and NND: 41.6 ± 5.8 μm) are similar to *in vivo* and *ex vivo* data from previous reports (Dandona et al, 1990; Fontana et al, 1998; Ivers et al, 2011; Quigley & Addicks, 1981; Vilupuru et al, 2007). Mean inter-eye percent differences in pore parameters when measured globally were 18.6 ± 15.4%, 3.9 ± 2.1%, and 9.5 ± 4.5% for pore area, elongation, and NND, respectively. The larger inter-eye percent difference in mean global pore area is likely caused by differences in the regions imaged between fellow eyes. Differences in the regions in which ALCS pores can be visualized due to shadows cast by overlying vasculature, prelaminar tissue, and/or the neuroretinal rim could reduce the number of pores that are imaged between eyes and potentially lead to larger inter-eye differences. For example, fewer pores were visualized in the superotemporal and inferotemporal sectors in the left eye (OS) of monkey M072 compared to its fellow eye due to increased overlying vasculature and prelaminar tissue in the left eye

(Fig. 3-4). Similar discrepancies in the regions imaged between right and left eyes can also be seen for monkey M070. Given that pore area has been shown to vary by region and sector (Dandona et al, 1990; Quigley & Addicks, 1981; Roberts et al, 2009), global measures of ALCS pore parameters could be statistically significantly different between fellow eyes of the same subject if the same regions/sectors are not comparably imaged in both eyes. Therefore, it is also important to perform local analyses of pore parameters to better compare ALCS pore geometry between and across eyes.

To better understand normal ALCS pore geometry on a local spatial scale, we also examined pore parameters in regions and sectors in all eyes. On average, mean pore areas were largest in the superotemporal sector and peripheral region across eyes (Table 3-2). Pores also tended to be further separated (i.e., larger NND) in the superotemporal sector. These *in vivo* results are in general agreement with previously reported *ex vivo* data. For example, Dandona et al. (Dandona et al, 1990) and Quigley et al. (Quigley & Addicks, 1981) found that pores located in superior and inferior sectors and peripheral regions in human eyes had larger pore areas, on average, than those located in nasal and temporal sectors and the central region. However, while our finding of larger pores in peripheral regions generally agreed with data from Roberts et al. showing high connective tissue density (or smaller laminar pores) in central regions of the monkey lamina cribrosa, our finding of larger pores in the superotemporal sector oppose their measurements showing that the superior ONH contained the highest density of laminar beams (or smaller laminar pores) (Roberts et al, 2009). This discrepancy could potentially be due to the fact that our pore measurements were confined to the anterior laminar surface while Roberts et al. examined connective tissue density within subvolumes that spanned the entire depth of the lamina. In addition, we found that pores were more elongated in the temporal sector across eyes (Table 3-2). Although not directly measured, previously published *ex vivo* images of the human

lamina cribrosa subjectively showed more elongated (or slit-like) pores along the horizontal meridian in the temporal region of the ONH compared to the superior and inferior poles (in agreement with the results reported in this study) (Quigley & Addicks, 1981).

Few statistically significant inter-eye differences in ALCS pore parameters (10 of 84 cases) were measured between corresponding regions and sectors across monkeys. The majority of these statistically significant cases occurred due to differences in the regions imaged or the number of pores marked between fellow eyes (e.g., the superotemporal sector and peripheral region in the left eye of monkey M072, Fig. 3-4). Calculation of inter-eye differences in laminar pore parameters on a global level can potentially lead to a misunderstanding of the true, physiologic similarities and differences in pore geometry between fellow eyes. For example, no statistically significant inter-eye differences in ALCS pore area, elongation, or NND were found on a global level in monkey M067 (Table 3-3). However, statistically significant inter-eye differences were found in pore area and NND in the temporal sector when pores were examined and compared on a local level. It is important to consider these results when examining early structural changes in laminar pore microarchitecture in experimental glaucoma or in human glaucomatous eyes, as significant changes in laminar beam and pore geometry could occur on a local scale before being detected on a global scale.

Based on previous postmortem studies that reported laminar pore areas to be larger in the superior and inferior poles and in the periphery of the lamina (Dandona et al, 1990; Quigley & Addicks, 1981; Roberts et al, 2009), we performed a cluster analysis on the ALCS pores marked in each eye to examine their spatial distributions according to their area, elongation, and NND. A Moran's I test was also performed on the clustered data sets to investigate whether the spatial arrangement of the pores based on each pore parameter was statistically significant. Half of the eyes had a statistically significant

positive spatial autocorrelation for pore area (in which larger Moran's I values correspond to an increased clustering of pores with similar properties, such as similar pore areas). Statistically significant positive spatial autocorrelations were also found in 58% and 92% of eyes when considering pore elongation and pore NND, respectively. In addition, the results of the cluster analyses often correlated with the results of the aforementioned local analyses performed in each eye. For example, a larger degree of spatial clustering of pores according to their area can be noted in the right eye of monkey M067 (Fig. 3-5c) in which larger area (red) pores are more clumped in the superotemporal portion of the lamina. This increased amount of spatial clustering not only agreed with the high positive Moran's I value of +0.11, but also spatially agreed with the fact that the superotemporal sector contained pores with statistically significantly larger areas and NNDs (compared to the temporal and inferotemporal sectors) in the same eye. Likewise, the local analyses that revealed no statistically significant differences in pore area between any sectors in the right eyes of monkeys M071 and M070 also agreed with the more random distribution of pores in the same eyes according to their area (as reflected by the very low Moran's I values of -0.02 and -0.01, respectively, and depicted in Fig. 3-5a,b, respectively).

In conclusion, *in vivo* measures of anterior lamina cribrosa surface pore geometry and ONH structure were similar between fellow eyes of normal non-human primates. These values will serve as normative data for future studies that examine longitudinal changes in ONH and laminar pore structure during experimental glaucoma. Moreover, the methods used to calculate laminar pore parameters can be extended to examine and track changes in laminar microarchitecture on local and global spatial scales during the onset and progression of glaucomatous neuropathy, potentially allowing for earlier detection of structural changes during disease and a better understanding of the biomechanical mechanisms responsible for glaucoma.

### 3.5 Acknowledgements

The software used for the adaptive optics system in this research was partially developed by Alfredo Dubra-Suarez, funded by a Career Award from the Burroughs Wellcome Fund, and Kamran Ahmad, funded by NIH grant BRP-EY01437 and the NSF Science and Technology Center for Adaptive Optics.

# CHAPTER 4

## *In vivo* changes in lamina cribrosa microarchitecture and optic nerve head structure in early experimental glaucoma

**Contributing authors:**

Nripun Sredar, Nimesh B. Patel, OD, PhD, Lakshmi Rajagopalan, Hope M. Queener, Ronald S. Harwerth, OD, PhD, and Jason Porter, PhD

**Abstract**

**Purpose:** The lamina cribrosa likely plays an important role in retinal ganglion cell axon injury in glaucoma. We sought to better understand the time-course of structural changes in the optic nerve head (ONH), anterior lamina cribrosa surface (ALCS) microarchitecture, and retinal nerve fiber layer thickness (RNFLT) in monkeys with experimental glaucoma (EG).

**Methods:** Spectral domain optical coherence tomography (SDOCT) images centered on the ONH were acquired before and approximately every two weeks after inducing unilateral EG in seven rhesus monkeys. ONH parameters (mean anterior lamina cribrosa surface depth [ALCSD], mean minimum rim width [MRW], and mean radius of curvature [RoC]) and RNFLT were quantified from semi-automatically segmented SDOCT images. Mean ALCS pore parameters were quantified globally, in 60° sectors, and in central and peripheral regions from images acquired at all time-points using an adaptive optics scanning laser ophthalmoscope.

**Results:** An increase in mean ALCSD was the first significant structural change measured in 6 of 7 EG eyes. A decrease in mean MRW simultaneously accompanied this early change in 4 of 6 EG eyes. The first significant structural change in the 7$^{th}$ EG eye was a decrease in mean MRW. Mean ALCS pore parameters were among the first or second changes detected in 4 EG eyes. A significant change in RNFLT and/or mean RoC was typically the last initial change to be measured. At the first time-point of significant change in ALCS pores, mean pore parameters increased globally and locally in the superotemporal and temporal sectors and in the central and peripheral regions. Local changes in one or more pore parameters were measured in 3 EG eyes prior to a globally measured change in the same parameter.

**Conclusions:** Structural changes in mean ALCSD, mean MRW, and ALCS pore geometry occurred prior to significant losses in RNFLT in early EG eyes. The increased sensitivity afforded by a local vs. global quantification of ALCS pores can enable earlier detection of laminar pore change and provide insights on biomechanical remodeling of the laminar microarchitecture in response to chronically elevated intraocular pressure in early EG.

## 4.1 Introduction

Glaucoma is a complex group of eye diseases that results in the death of retinal ganglion cells (RGCs) and the degeneration of their axons, culminating in irreversible losses in vision. The mechanisms responsible for the onset and progression of glaucoma are not well understood. Axonal damage is believed to initially occur in the optic nerve head (ONH) at the level of the lamina cribrosa, a sieve-like structure comprised primarily of a meshwork of collagen beams that provides structural and functional support to RGC axons that pass through the ONH to the brain. Previous work has shown that increased stress from elevated intraocular pressure (IOP) can strain or deform the lamina (Bellezza, 2000; Roberts et al, 2010; Sigal et al, 2004), resulting in biomechanical alterations to the load-bearing laminar beams (Bellezza et al, 2003; Downs et al, 2008) and changes in laminar beam and pore geometry (Vilupuru et al, 2007). Stretching and deformation of these laminar beams (and associated pores) could shear or damage encompassed axons and laminar capillaries, thereby hampering axonal transport (Anderson & Hendrickson, 1974; Anderson & Hendrickson, 1977; Quigley & Anderson, 1976; Quigley & Addicks, 1980; Quigley & Anderson, 1977; Quigley et al, 1979), blood flow and the diffusion of nutrients (Anderson, 1969), and the neurotrophic support provided to the axons due to alterations in the overlying astrocytes (Hernandez, 2000).

Conventional measures used clinically to detect glaucoma focus primarily on assessment of retinal nerve fiber layer thickness (RNFLT) and visual field loss. However, recent work has shown that 10-15% of RGC axons are already lost when a first change in RNFLT is reliably detected (Cull et al, 2012). Therefore, it is important to better understand structural alterations in early stages of glaucoma for earlier detection and diagnosis. Several *ex vivo* studies have shown a posterior displacement of the anterior lamina cribrosa surface (ALCS) in human glaucoma patients (Jonas et al, 2003; Quigley

et al, 1981; Quigley et al, 1983) and in non-human primates with early experimental glaucoma (Bellezza et al, 2003; Burgoyne et al, 2004; Yang et al, 2007b). These histological observations have been confirmed *in vivo* in human glaucoma patients who have shown significantly larger mean anterior lamina cribrosa surface depths (ALCSDs) compared to normal eyes (Furlanetto et al, 2013; Lee et al, 2012). Increases in mean ALCSD have also been measured *in vivo* prior to a reduction in RNFLT in non-human primates with early experimental glaucoma (Strouthidis et al, 2011b). Furthermore, significant decreases in mean minimum rim width (MRW), an ONH parameter that may potentially act as a surrogate for detecting RNFL loss, and significant increases in mean ALCSD have been shown to precede a significant loss in RNFLT in glaucoma (Chauhan et al, 2013; Fortune et al, 2013; He et al, 2014).

In addition to examining global ONH structure and laminar shape, it is important to understand global and local changes in lamina cribrosa microarchitecture with disease (Downs et al, 2011; Fontana et al, 1998; Inoue et al, 2009; Lee et al, 2012; Park et al, 2012; Tezel et al, 2004). Early histological studies in normal human eyes showed decreased connective tissue density and larger pore areas in the superior and inferior sectors of the lamina cribrosa and suggested this laminar geometry could potentially be responsible for the regional susceptibility of RGC axons to early damage in glaucoma (Dandona et al, 1990; Quigley & Addicks, 1981). More recent histological work by Roberts et al. in normal non-human primate eyes found laminar connective tissue to be most dense in the central and superior regions of the ONH (Roberts et al, 2009). However, despite an increase in the number of laminar beams that were measured throughout the thickness of the lamina in early experimental glaucoma eyes, the connective tissue volume fraction (the relative amount of laminar beams within the lamina cribrosa volume) remained relatively unchanged (Roberts et al, 2009). In light of

this work, *in vivo* studies are necessary to validate *ex vivo* results and examine longitudinal changes in laminar microarchitecture during glaucoma.

High-resolution, *in vivo* measurements of the lamina cribrosa microarchitecture have been carried out in normal and glaucomatous eyes using a variety of imaging techniques (e.g., adaptive optics scanning laser ophthalmoscopy and optical coherence tomography) (Akagi et al, 2012; Ivers et al, 2011; Nadler et al, 2013; Sredar et al, 2013; Vilupuru et al, 2007; Wang et al, 2013). Larger ALCS pore areas have been measured at a single time-point in human glaucoma patients (Akagi et al, 2012) and non-human primate eyes with experimental glaucoma (Sredar et al, 2013; Vilupuru et al, 2007) (compared to normal human subjects and fellow control eyes, respectively) via adaptive optics scanning laser ophthalmoscope (AOSLO) imaging. Three-dimensional images of the lamina cribrosa acquired using swept source optical coherence tomography (SSOCT) imaging have shown significant increases in beam thickness and significant decreases in pore diameter with increasingly worse visual field performance (i.e., worse mean deviation) in human glaucoma patients at a single time-points (Wang et al, 2013). These and other cross-sectional studies support the need to longitudinally examine the structural changes that occur in laminar microarchitecture on global and local scales in concert with the structural changes that occur in the ONH and RNFL during the progression of glaucoma.

We have longitudinally examined global and local changes in ALCS pores along with structural changes in the ONH and RNFL to determine whether *in vivo* changes in laminar pore and ONH structure precede changes in RNFLT in non-human primates with unilateral experimental glaucoma. Statistical tests were performed to determine the initial onset of change in global and local lamina cribrosa pore parameters, ONH parameters, and RNFLT. This paper provides a better understanding of the time-course of structural

changes in the ONH, lamina cribrosa microarchitecture, and RNFL in early stages of glaucoma.

### 4.2 Methods

All animal care experimental procedures were approved by the University of Houston's Institutional Animal Care and Use Committee and adhered to the ARVO Statement for the Use of Animals in Ophthalmic and Vision Research. Longitudinal examination of the anterior lamina cribrosa and ONH was performed *in vivo* in fellow eyes of 7 rhesus monkeys (*Macaca mulatta*) induced with unilateral experimental glaucoma. Argon laser treatment of the trabecular meshwork was used to elevate the intraocular pressure of each monkey's right eye, while fellow eyes served as controls (Gaasterland & Kupfer, 1974; Harwerth et al, 1997; Pederson & Gaasterland, 1984; Quigley & Hohman, 1983). The mean (± SD) age of the 7 monkeys at the time-point of the first laser treatment was 3.7 ± 0.5 years (Table 1). Monkeys were anesthetized with 20-25 mg/kg ketamine, 0.8-0.9 mg/kg xylazine, and 0.04 mg/kg atropine sulfate to minimize eye movements during *in vivo* imaging (Frishman et al, 1996), and pupils were dilated with 2.5% phenylephrine and 1% tropicamide. A pharmacological agent (IOPIDINE, Alcon Laboratories, Inc., Fort Worth, TX, USA or COMBIGAN, Allergan, Inc., Irvine, CA, USA) was used at the start of each imaging experiment to reduce IOPs to levels at or near baseline and ensure that the structural changes measured during the experiment were due to chronic changes resulting from a sustained elevation in IOP (and not a transient pressure spike). Maximum IOP and cumulative IOP difference were monitored in control and EG eyes after the first laser procedure. Cumulative IOP difference was calculated at each time point by successively integrating IOP up to the given time-point in the EG eye and subtracting the corresponding cumulative IOP from the fellow control eye (Yang et al, 2011). A head mount was used to stabilize the monkey's head during spectral domain

optical coherence tomography (SDOCT) and AOSLO imaging. A lid speculum was used to keep the eyelids open and a contact lens was placed on the monkey eye to prevent corneal dehydration during imaging. Each monkey had at least one baseline imaging session prior to the first laser procedure and was subsequently imaged approximately every 2 weeks following the first laser session.

### *4.2.1 Biometric measurements and image scaling*

An ocular biometer (IOLMaster; Carl Zeiss Meditec, AG, Jena, Germany) was used to measure axial length, anterior chamber depth, and anterior corneal curvature in all eyes at every time-point. These biometric measurements were used to laterally scale SDOCT and AOSLO images using previously defined methods (Ivers et al, 2011).

### *4.2.2 Spectral domain optical coherence tomography (SDOCT) imaging and analysis*

Scanning laser ophthalmoscope (SLO) images of the ONH (30° x 30°) were acquired (Spectralis HRA+OCT; Heidelberg Engineering, Heidelberg, Germany) at all time-points. Mean peripapillary RNFL thickness (RNFLT) was measured in each eye from 12° circular scans centered on the ONH at every time-point. Cross-sectional radial scans (20° field, 48 B-scans) centered on the ONH were acquired in each eye using the same SDOCT instrument at every time-point. Scans from follow-up time-points were registered to the baseline time-point using the SDOCT instrument's software to ensure the same region was imaged every time. Bruch's membrane opening (BMO) and the anterior lamina cribrosa surface (ALCS) were marked in as many B-scans as possible using a custom program (MATLAB; The MathWorks, Inc., Natick, MA). Mean anterior lamina cribrosa surface depth (ALCSD) was computed as the mean distance between a plane best-fit to the marked BMO points and a thin-plate spline surface that was fit to the

marked ALCS points to model the ALCS in three dimensions (Sredar et al, 2013). The ALCS was further characterized by computing its mean radius of curvature (RoC) within the projection of the BMO ellipse (an ellipse best-fit to the marked BMO points) onto the thin-plate spline model of the ALCS (Sredar et al, 2013). In addition, the internal limiting membrane (ILM) was automatically segmented using the SDOCT instrument's software and manually corrected to determine mean minimum rim width (MRW), the minimum distance between each BMO point and the ILM averaged across all B-scans (Chapter 3). Mean ALCSD, RoC, MRW, and RNFLT were quantified at every time-point for control and EG eyes. SDOCT images were not acquired and ONH parameters were not quantified in the control eye of monkey OHT-65 at any time-point due to the eye's poor optical quality. However, SDOCT images of the EG eye of monkey OHT-65 were acquired at every time-point.

### *4.2.3 Adaptive optics scanning laser ophthalmoscope (AOSLO) imaging and analysis*

The methods for imaging the ALCS microarchitecture using an AOSLO have been described previously (Ivers et al, 2011). Briefly, adaptive optics reflectance imaging of the plane of best-focus was performed throughout as much of the optic nerve head as possible. Videos were acquired over a 1.5° field at a rate of 25 Hz using an 840 nm superluminescent diode (S-Series Broadlighter, Superlum, Carrigtwohill, Ireland) (Ivers et al, 2011; Li et al, 2010a; Sredar et al, 2013). Registered images were created from AOSLO videos using a custom program (MATLAB; The MathWorks, Inc., Natick, MA) and combined to generate a montage of the ALCS microarchitecture in the control and EG eyes of each monkey (Adobe Photoshop; Adobe Systems, San Jose, CA) at each time-point.

Image contrast in each ALCS montage was further improved using a contrast

limiting adaptive histogram equalization (CLAHE) algorithm (ImageJ; developed by Wayne Rasband, National Institutes of Health, Bethesda, MD; available at http://rsb.info.nih.gov/ij/index.html) and pore boundaries were manually marked (Adobe Photoshop) using previously described methods found to have excellent repeatability and reproducibility (Ivers et al, 2011). AOSLO images of the ALCS represent a projected view of the 3D laminar surface. Therefore, 2D AOSLO images were transformed into their approximate 3D configuration by registering and projecting the AOSLO image onto the thin-plate spline representation of the ALCS (Sredar et al, 2013). Following 3D transformation, the area, elongation, and nearest neighbor distance of all marked pores were quantified in each montage and analyzed globally, regionally (centrally vs. peripherally) and within 60° sectors. Pores were separated into central and peripheral regions by dividing the area contained within the BMO ellipse into 2 regions of equal area. Meridians were also constructed at 60° intervals from the major axis of the same BMO ellipse in order to locally examine pores in superotemporal, temporal, and inferotemporal sectors. Pore parameters were compared longitudinally throughout the progression of experimental glaucoma. Again, due to its poor optical quality, AOSLO images were not acquired and pore geometry was not quantified in the control eye of monkey OHT-65 at any time-point. However, AOSLO images of its EG eye were acquired at every time-point.

### *4.2.4 Statistical analysis*

The coefficients of variation [(SD/mean) **x** 100] and repeatability [1.96 **x** SD **x** $\sqrt{2}$] were calculated for mean ALCSD, mean RoC, mean MRW, and RNFLT across all time-points in each control eye. The 95% confidence intervals were subsequently calculated for each ONH parameter in each control eye. The first time-point of significant change for each ONH parameter in each EG eye was determined as the first time-point that fell

outside the 95% confidence interval (established from the control eyes) and had no subsequent time-points with values that fell back within the confidence interval. To determine the first significant time-point of change in each ONH parameter in monkey OHT-65 (i.e., the monkey without control eye data), data from the EG eye of OHT-65 was compared to the 95% confidence interval generated from all control eye data in the other 6 monkeys. The first time-point that fell outside the 95% confidence interval that was generated from all other control eyes (and had no later time-points with values within the confidence interval) represented the first significant time-point of change for ONH parameters in the EG eye of OHT-65.

Mean pore area, elongation, and NND were compared globally, regionally (centrally and peripherally) and by sector (superotemporally, temporally and inferotemporally) across all time-points within each EG eye. 95% confidence intervals were calculated for pore area, elongation, and NND in all EG eyes across early time-points that showed no statistically significant differences in all pore parameters as determined using a Mann-Whitney rank sum test. *P* values >.05 were taken to represent no statistically significant differences from baseline. The first significant time-point of change in a pore parameter was determined to be the first time-point that fell outside the 95% confidence interval. If it was not possible to image and mark any pores within a given region or sector at a particular time point, statistical comparisons were not conducted for that region or sector in the given EG eye at that time.

**Table 4-1.** IOP data for control and EG eyes throughout duration of the study.

| Animal ID | Age (yrs) | Mean IOP (± SD) | | Maximum IOP | | Reduced IOP in EG Eye (mmHg) | Cumulative IOP Difference (mmHg-days) |
|---|---|---|---|---|---|---|---|
| | | Control Eye (mmHg) | EG Eye (mmHg) | Control Eye (mmHg) | EG Eye (mmHg) | | |
| OHT-63 | 3.9 | 14.1 ± 1.1 | 24.1 ± 12.1 | 16 | 49 | 18.4 ± 5.0 | 3,880 |
| OHT-64 | 4.2 | 14.5 ± 2.1 | 25.5 ± 12.7 | 21 | 47 | 18.3 ± 6.4 | 5,280 |
| OHT-65 | 3.0 | 10.6 ± 2.6 | 25.4 ± 14.6 | 17 | 51 | 17.2 ± 9.0 | 8,720 |
| OHT-66 | 3.2 | 14.5 ± 2.0 | 33.3 ± 15.5 | 19 | 60 | 18.2 ± 7.8 | 9,824 |
| OHT-67 | 3.3 | 12.7 ± 2.6 | 26.8 ± 12.4 | 18 | 51 | 18.1 ± 7.7 | 10,441 |
| OHT-68 | 3.9 | 13.1 ± 2.5 | 25.9 ± 9.9 | 17 | 45 | 20.0 ± 9.6 | 6,461 |
| OHT-69 | 4.2 | 13.2 ± 1.7 | 34.5 ± 11.3 | 17 | 50 | 24.7 ± 10.4 | 8,975 |
| **Mean ± SD** | 3.7 ± 0.5 | 13.2 ± 1.4 | 27.9 ± 4.2 | 17.9 ± 1.7 | 50.4 ± 4.8 | 19.3 ± 2.5 | 7,654 ± 2,472 |

### 4.3 Results

IOP measurement data for all control and EG eyes are shown in Table 4-1. Mean values of unaltered IOP (± SD) across all time-points were 13.2 ± 1.4 mmHg in control eyes and 27.9 ± 4.2 mmHg in EG eyes. On average, the maximum unaltered IOP was 17.9 ± 1.7 mmHg across control eyes and 50.4 ± 4.8 mmHg across EG eyes. IOP was pharmacologically lowered to near baseline levels at the start of each imaging experiment. Across all EG eyes, the mean pharmacologically-reduced IOP was 19.3 ± 2.5 mmHg, which was 6.0 mmHg larger than the mean unaltered IOP in the fellow control eyes. Over a mean experiment duration of 528 ± 107 days, the mean cumulative IOP difference was 7,654 ± 2,472 mmHg-days across all 7 monkeys. A steady increase in cumulative IOP difference was observed for each monkey (Fig. 4-1a).

Retinal nerve fiber layer thickness and ONH parameters remained stable in control eyes for the duration of the study. Mean (± SD) RNFLT, ALCSD, RoC, and MRW values calculated across all control eyes were 105.6 ± 6.8 µm, 214.0 ± 25.3 µm, 3.6 ± 1.0 mm, and 308.7 ± 55.1 µm, respectively (Table 4-2). Coefficients of variation and repeatability were small for RNFLT, ALCSD, RoC, and MRW in all control eyes (Table 4-2), indicating low variability and high precision in measured values over time.

Significant longitudinal changes were measured in RNFLT and ONH parameters (mean ALCSD, mean RoC, and mean MRW) in all EG eyes except for monkey OHT-67, who had no significant changes in mean RoC (3.7 mm at baseline and 2.3 mm at the final time-point) and RNFLT (111 µm at baseline and 103 µm at the final time-point). A progressive increase in mean ALCSD was measured in all EG eyes, whereas RNFLT, mean RoC, and mean MRW tended to decrease throughout the study (Fig. 4-1b-e). Magnified versions of the plots in Fig. 4-1 are shown in Fig. 4-2 for the first 300 days following the initial laser treatment and illustrate the time-points at which the first statistically significant changes occurred for each parameter in the experimental

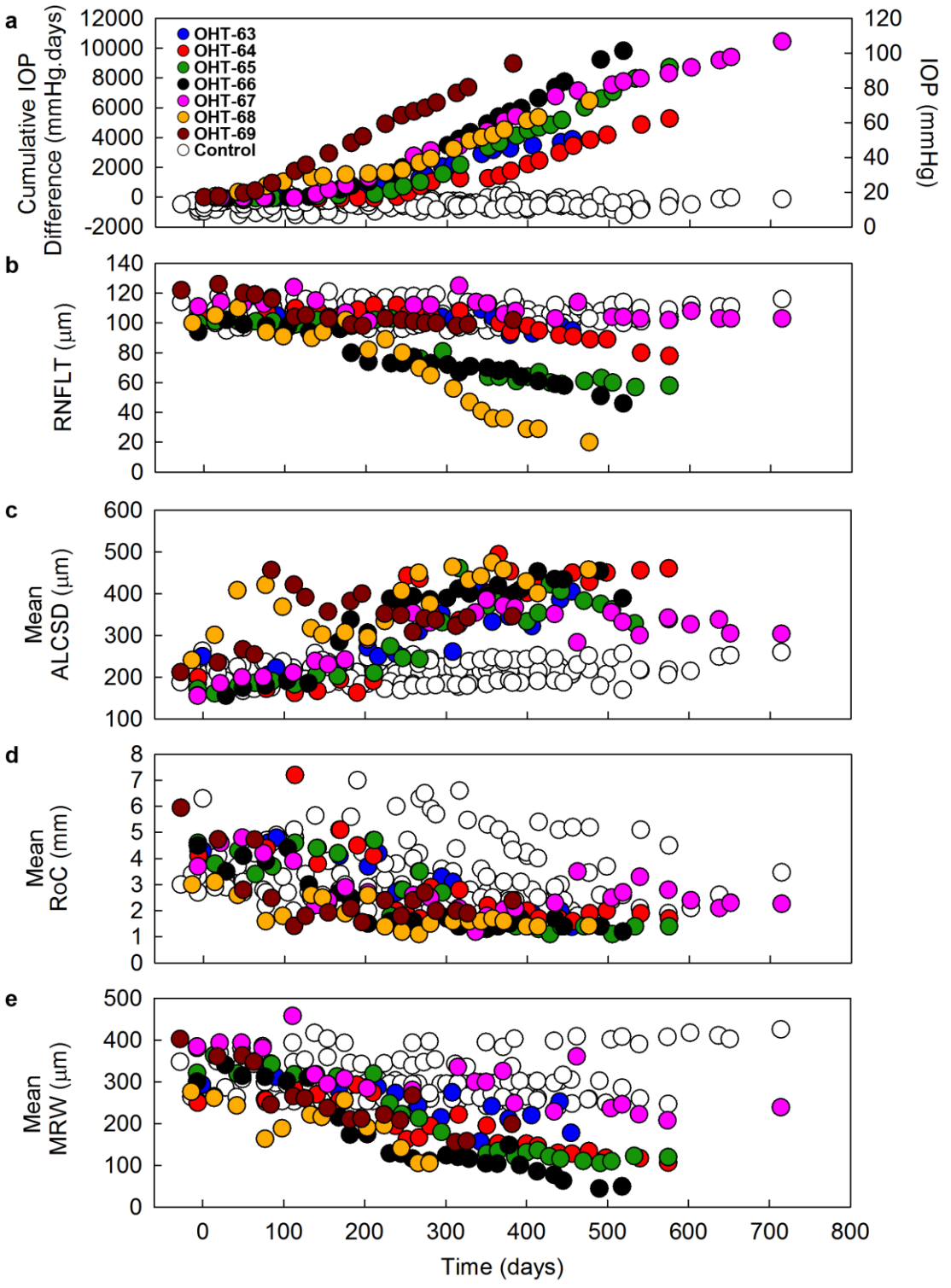


**Figure 4-1.** Longitudinal changes in IOP, RNFLT, and ONH parameters in control eyes and eyes with experimental glaucoma. Plots of (a) cumulative IOP difference, (b) RNFLT, (c) mean ALCSD, (d) mean RoC, and (e) mean MRW as a function of study

time for all monkeys. Filled colored circles represent EG eyes. Open white circles represent control eyes. (In [a], open white circles represent to control IOP data corresponding to far right axis). Progressive increases were measured in cumulative IOP difference and mean ALCSD with increasing study duration, whereas progressive decreases were measured for RNFLT, mean RoC, and mean MRW in nearly all EG eyes.

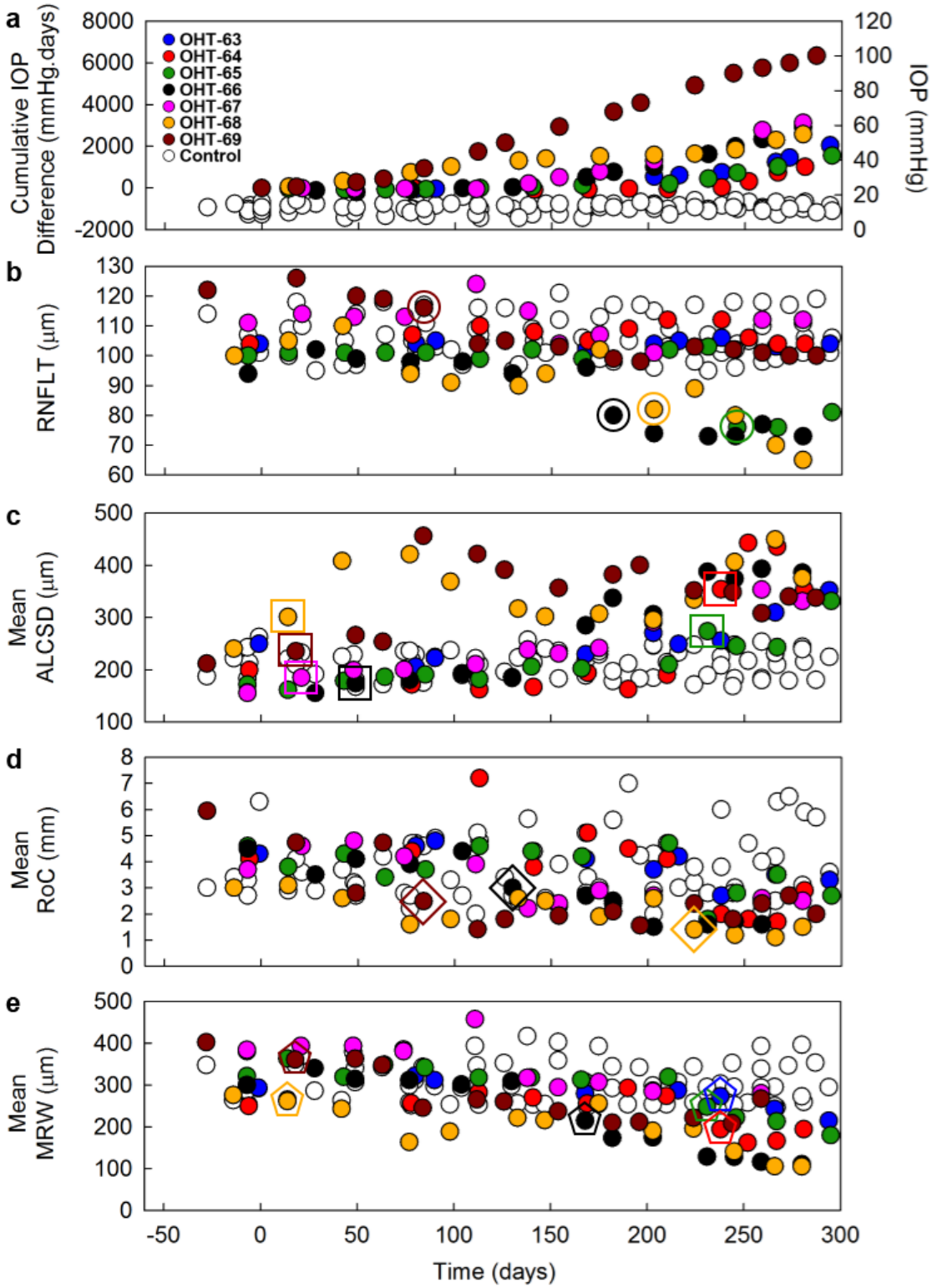


**Figure 4-2.** Longitudinal changes in (a) cumulative IOP difference, (b) RNFLT, (c) mean ALCSD, (d) mean RoC, and (e) mean MRW in control eyes (open white circles)

and eyes with experimental glaucoma (filled color circles) for the first 300 days after the initial laser treatment (truncated from Fig. 4-1). Time-points of first statistically significant change in each parameter are illustrated by large circle (RNFLT), square (mean ALCSD), diamond (mean RoC) and pentagon (mean MRW) symbols. Symbols are not shown for all EG eyes as some parameters significantly changed later than 300 days after the initial treatment and are not plotted in this abbreviated figure. For example, OHT-63, OHT-64, and OHT-67 did not show a significant decrease in RNFLT (Fig. 4-2b) until after the first 300 days of the study (378 days, 365 days, and no change, respectively).

**Table 4-2.** RNFLT and mean ONH parameters averaged across all study time-points for each control eye.

| | RNFLT | | | ALCSD | | | RoC | | | MRW | | |
|---|---|---|---|---|---|---|---|---|---|---|---|---|
| **Animal ID** | **Mean ± SD (µm)** | **Coeff. of Repeat. (µm)** | **Coeff. of Variation (%)** | **Mean ± SD (µm)** | **Coeff. of Repeat. (µm)** | **Coeff. of Variation (%)** | **Mean ± SD (mm)** | **Coeff. of Repeat. (mm)** | **Coeff. of Variation (%)** | **Mean ± SD (µm)** | **Coeff. of Repeat. (µm)** | **Coeff. of Variation (%)** |
| OHT-63 | 101.9±1.3 | 3.5 | 1.3 | 225.9±14.5 | 40.1 | 6.4 | 3.9±1.1 | 3.2 | 29.5 | 299.7±5.8 | 15.9 | 1.9 |
| OHT-64 | 104.0±1.5 | 4.1 | 1.4 | 215.1±3.9 | 10.8 | 1.8 | 5.1±0.9 | 2.4 | 17.4 | 252.1±5.3 | 14.7 | 2.1 |
| OHT-65 | 106.8±1.9 | 5.2 | 1.7 | -- | -- | -- | -- | -- | -- | -- | -- | -- |
| OHT-66 | 97.3±1.9 | 5.4 | 2.0 | 184.5±5.9 | 16.5 | 3.2 | 2.6±0.3 | 0.9 | 11.9 | 297.3±6.5 | 18.1 | 2.2 |
| OHT-67 | 111.8±2.0 | 5.5 | 1.8 | 237.8±14.3 | 39.6 | 6.0 | 2.7±0.8 | 2.3 | 31.3 | 398.2±13.5 | 37.4 | 3.4 |
| OHT-68 | 100.5±2.0 | 5.7 | 2.0 | 238.7±9.5 | 26.4 | 4.0 | 3.0±0.5 | 1.4 | 17.1 | 259.7±6.1 | 17.0 | 2.4 |
| OHT-69 | 116.9±1.8 | 4.9 | 1.5 | 182.1±10.5 | 29.2 | 5.8 | 4.3±1.0 | 2.8 | 23.2 | 345.4±6.2 | 17.0 | 1.8 |
| **Mean ± SD** | 105.6±6.8 | 4.9±0.8 | 1.7±0.3 | 214.0±25.3 | 27.1±11.9 | 4.5±1.8 | 3.6±1.0 | 2.2±0.9 | 21.7±7.6 | 308.7±55.1 | 20.0±8.6 | 2.3±0.6 |

'--' indicates SDOCT images were not acquired and ONH parameters were not quantified.

**Table 4-3.** RNFLT and mean ONH parameters averaged across all study time-points for each EG eye.

| Animal ID | RNFLT | | ALCSD | | RoC | | MRW | |
|---|---|---|---|---|---|---|---|---|
| | Mean ± SD (µm) | Minimum (µm) | Mean ± SD (µm) | Maximum (µm) | Mean ± SD (mm) | Minimum (mm) | Mean ± SD (mm) | Minimum (mm) |
| OHT-63 | 102.4±4.8 | 92 | 293.5±66.4 | 409.6 | 3.1±1.2 | 1.3 | 257.6±47.0 | 156.9 |
| OHT-64 | 100.3±10.1 | 78 | 348.3±121.0 | 494.5 | 2.8±1.5 | 1.5 | 188.7±61.1 | 106.1 |
| OHT-65 | 78.8±18.7 | 57 | 296.6±94.2 | 460.7 | 2.6±1.4 | 1.1 | 208.6±96.5 | 105.2 |
| OHT-66 | 75.5±15.9 | 46 | 340.2±102.9 | 454.6 | 2.2±1.1 | 1.2 | 162.2±94.2 | 44.2 |
| OHT-67 | 109.2±6.5 | 101 | 295.5±66.1 | 385.7 | 2.8±0.9 | 1.2 | 306.4±67.2 | 207.5 |
| OHT-68 | 69.8±29.3 | 20 | 385.1±69.1 | 475.0 | 1.9±0.6 | 1.1 | 196.9±56.5 | 104.8 |
| OHT-69 | 106.5±9.4 | 98 | 337.6±64.4 | 456.7 | 2.6±1.2 | 1.4 | 256.8±74.6 | 155.1 |
| **Mean ± SD** | 91.8±16.4 | 70.3±30.4 | 328.1±34.5 | 448.1±37.7 | 2.6±0.4 | 1.3±0.2 | 225.3±50.0 | 125.7±52.3 |

glaucoma eyes [denoted by large circle (RNFLT), square (mean ALCSD), diamond (mean RoC) and pentagon (mean MRW) symbols]. On average across all EG eyes, maximum ALCSD was 448.1 ± 37.7 µm, while minimum RNFLT, RoC, and MRW were 70.3 ± 30.4 µm, 1.3 ± 0.2 mm, and 125.7 ± 52.3 mm, respectively (Table 4-3). These values represent a +133%, -34%, -70%, and -61% average change from baseline values in mean ALCSD, RNFLT, RoC, and MRW, respectively, across all EG eyes.

Similar to our control eye results for ONH parameters, mean ALCS pore geometry did not significantly change over time in any control eye. For example, no statistically significant differences in global pore parameters were measured between representative time-points separated by 4 months (2.8%, 2.5%, and 0.1% differences in mean pore area, elongation, and NND, respectively; $P>.05$) in the control eye of monkey OHT-64 (Fig. 4-3). On a local level, there were no statistically significant differences in pore parameters in all sectors and regions between time-points except for pore area in the inferotemporal sector ($P<.05$). These results agree with earlier findings from our previous study that revealed small intersession variability in pore geometry in normal rhesus monkeys (Ivers et al, 2011).

Distinct structural changes in laminar beams and pores were observed over time in all EG eyes but one (OHT-67). In addition to measuring no significant changes in mean RoC and RNFLT throughout the study in the EG eye of OHT-67, this eye also exhibited no significant changes in ALCS pore geometry at any time-point. Figure 4-4 shows AOSLO montages of ALCS microarchitecture at baseline time-points (columns 1 and 3) and time-points corresponding to the first statistically significantly measured change in ALCS pore geometry (columns 2 and 4) in each EG eye. Each baseline montage represents an image averaged from baseline time-points and time-points that had no measured differences in ALCS pore geometry compared to baseline. Each “first

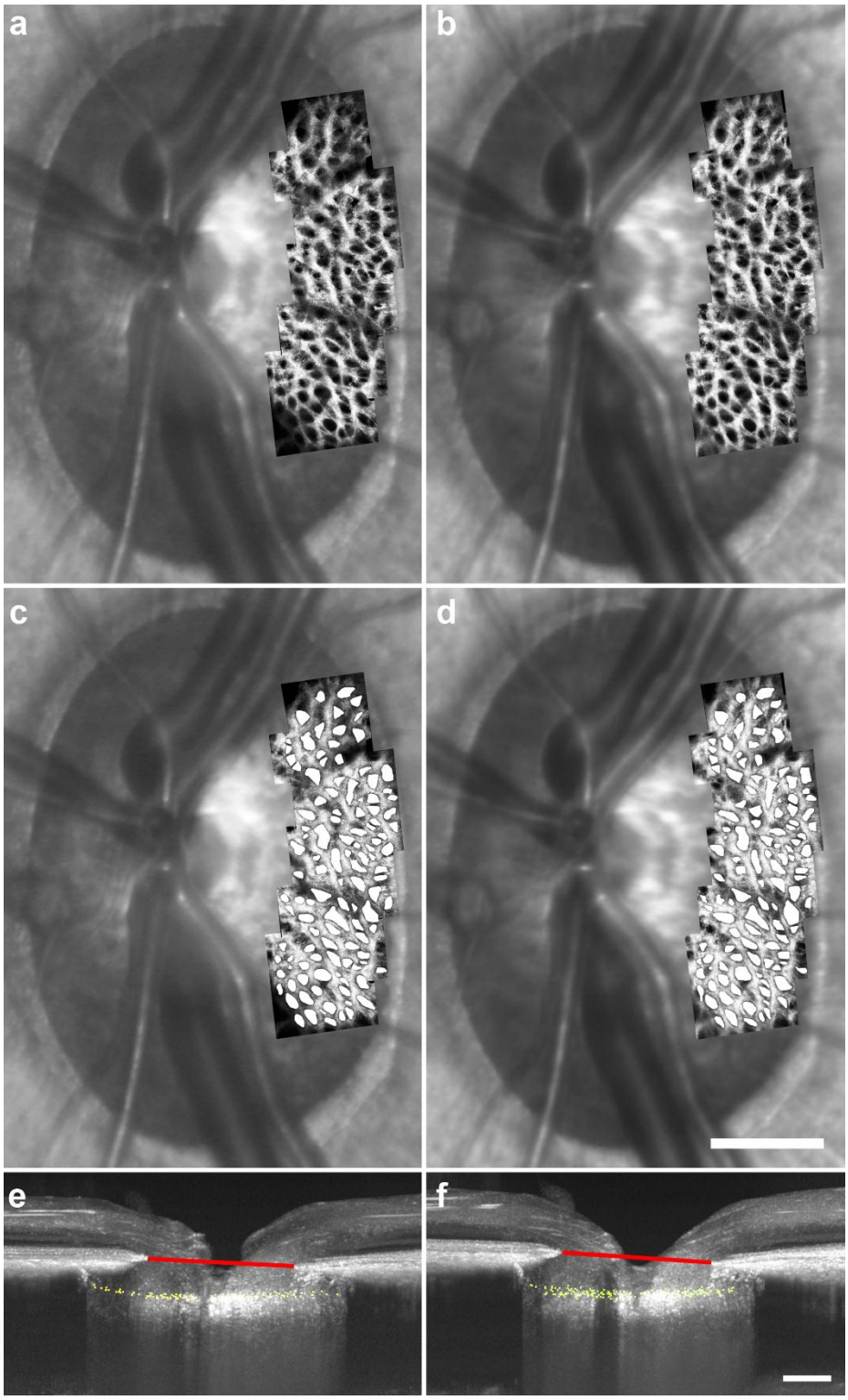


**Figure 4-3.** Anterior lamina cribrosa surface structure from a representative control eye at different time-points. (a-b) AOSLO montages of the ALCS overlaid on the corresponding SLO images in the control eye of monkey OHT-64 at two time-points

separated by 90 days. Laminar structure appears subjectively similar between imaging sessions. (c-d) Pores were manually marked in each AOSLO montage (white filled shapes). No statistically significant differences in ALCS pore geometry were measured between time-points on global and local levels (*P*>.05). (E-F) SDOCT maximum intensity projection images from all B-scans acquired at the same time-points as the AOSLO images in (a,b). The ALCS (yellow dots) and BMO reference plane (red lines) were manually marked in each SDOCT B-scan. No statistically significant difference in mean ALCSD was measured between the two time-points [215.2 µm (e) vs. 220.6 µm (f)]. Scale bar: 350 µm.

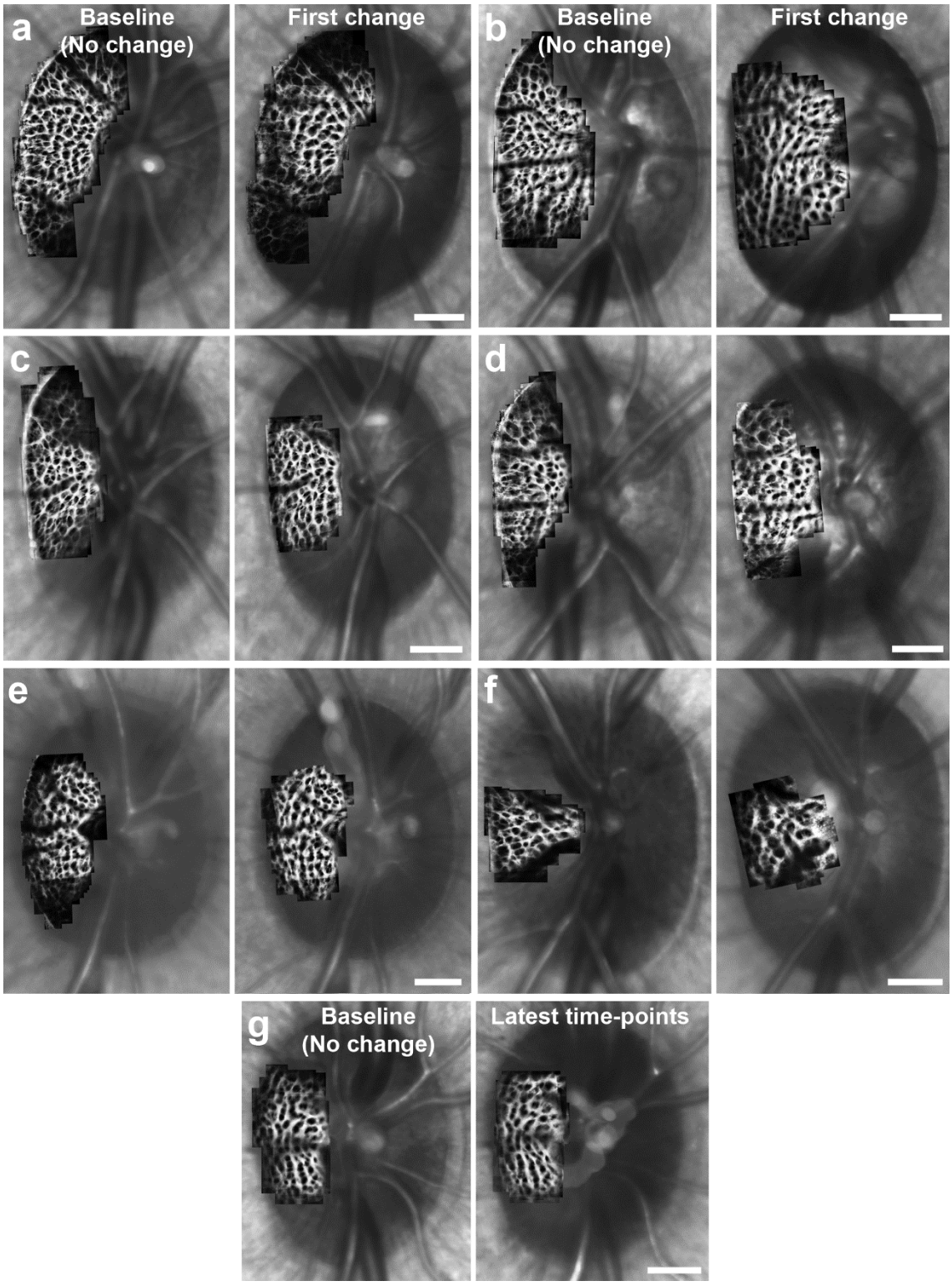


**Figure 4-4.** Distinct changes in laminar beam and pore structure were observed in EG eyes. (a-f) AOSLO montages of the ALCS were constructed, registered, and averaged across multiple time-points in the same EG eye for each monkey and overlaid on the

corresponding SLO images to show the lamina cribrosa before (left) and after (right) changes were seen in experimental glaucoma. Large differences in beam and pore structure can be seen in 6 of 7 EG eyes over time. (a: OHT-63; b: OHT-64; c: OHT-65; d: OHT-66; e: OHT-68; f: OHT-69.) (g) ALCS pore structure did not change significantly over time in the EG eye of monkey OHT-67. Scale bar: 300 μm.

**Table 4-4.** Values of mean (± SD) pore parameters measured at baseline (No change) and at the first time-point of statistically significant change in laminar pore geometry (First change) on global, regional (central, peripheral), and sector scales.

| | Area (μm²) | | Elongation | | NND (μm) | |
|---|---|---|---|---|---|---|
| | **Baseline (No Change)** | **First change** | **Baseline (No change)** | **First change** | **Baseline (No change)** | **First change** |
| **Global** | 869.5±109.4 | 1079.1±176.3* | 1.75±0.10 | 1.76±0.08 | 37.2±2.9 | 42.2±5.4* |
| **Central** | 801.9±89.0 | 982.4±146.4* | 1.72±0.08 | 1.71±0.09 | 36.1±2.6 | 40.3±6.2* |
| **Peripheral** | 920.6±277.9 | 1301.8±252.4* | 1.77±0.16 | 1.93±0.46 | 39.5±3.5 | 47.8±7.3* |
| **Superotemporal** | 919.2±171.0 | 1141.1±264.4 | 1.69±0.12 | 1.72±0.08 | 42.0±10.1 | 43.3±5.8* |
| **Temporal** | 823.3±83.4 | 1115.0±162.1* | 1.81±0.13 | 1.83±0.12 | 36.6±2.6 | 42.9±6.3* |
| **Inferotemporal** | 961.9±280.9 | 1049.6±454.7 | 1.63±0.08 | 1.70±0.23 | 40.4±3.8 | 40.5±7.9 |

'*' indicates a statistically significant difference in a laminar pore parameter compared to previous baseline time-points with no change (P<.05).

change" montage represents an image averaged from the time-point of first significant change in ALCS pore geometry and any subsequent time-points that showed no statistically significant change in ALCS pore geometry from the first time of measured change. Table 4-4 summarizes mean ALCS pore geometry at the first time-point of global and/or local change in laminar pores compared to baseline and earlier time-points of no change across all EG eyes. Mean ALCS pore area statistically significantly increased globally, regionally (centrally and peripherally), and in the temporal sector at the time of first change. Correspondingly, mean ALCS pore NND significantly increased globally and in all regions and sectors (except inferotemporally) at the same time. However, mean ALCS pore elongation did not significantly change on global or local scales across all EG eyes at the time of first change in pore area and NND ($P>.05$). In addition, global and/or local changes in one or more ALCS pore parameters were measured in 3 EG eyes (OHT-63, OHT-65, and OHT-68) prior to a globally measured change in the same parameter.

The time-points corresponding to the first significant changes in ALCS pore geometry, ONH parameters, and RNFLT were compared in each EG eye. In two EG eyes (OHT-64 and OHT-65), the first structural parameters that significantly changed from baseline were ALCS pore geometry, mean ALCSD, and mean MRW. Images of the ALCS microarchitecture and ONH acquired at baseline time-points and the time-point of first significant change in ALCS pore geometry and mean ALCSD for the EG eye of OHT-64 are shown in Fig. 4-5. Mean ALCS pore geometry (when measured globally and locally) and mean ALCSD were not significantly different between baseline (Fig. 4-5a,d,g) and a subsequent time-point of no change (Fig. 4-5b,e,h) ($P>.05$). The first statistically significant change in ALCS pore geometry and mean ALCSD occurred simultaneously in this EG eye (Fig. 4-5c,f,i). Globally, mean ALCS pore area significantly increased relative to baseline time-points (1,192.4 ± 781.0 $\mu m^2$ vs. 961.9 ± 892.9 $\mu m^2$,

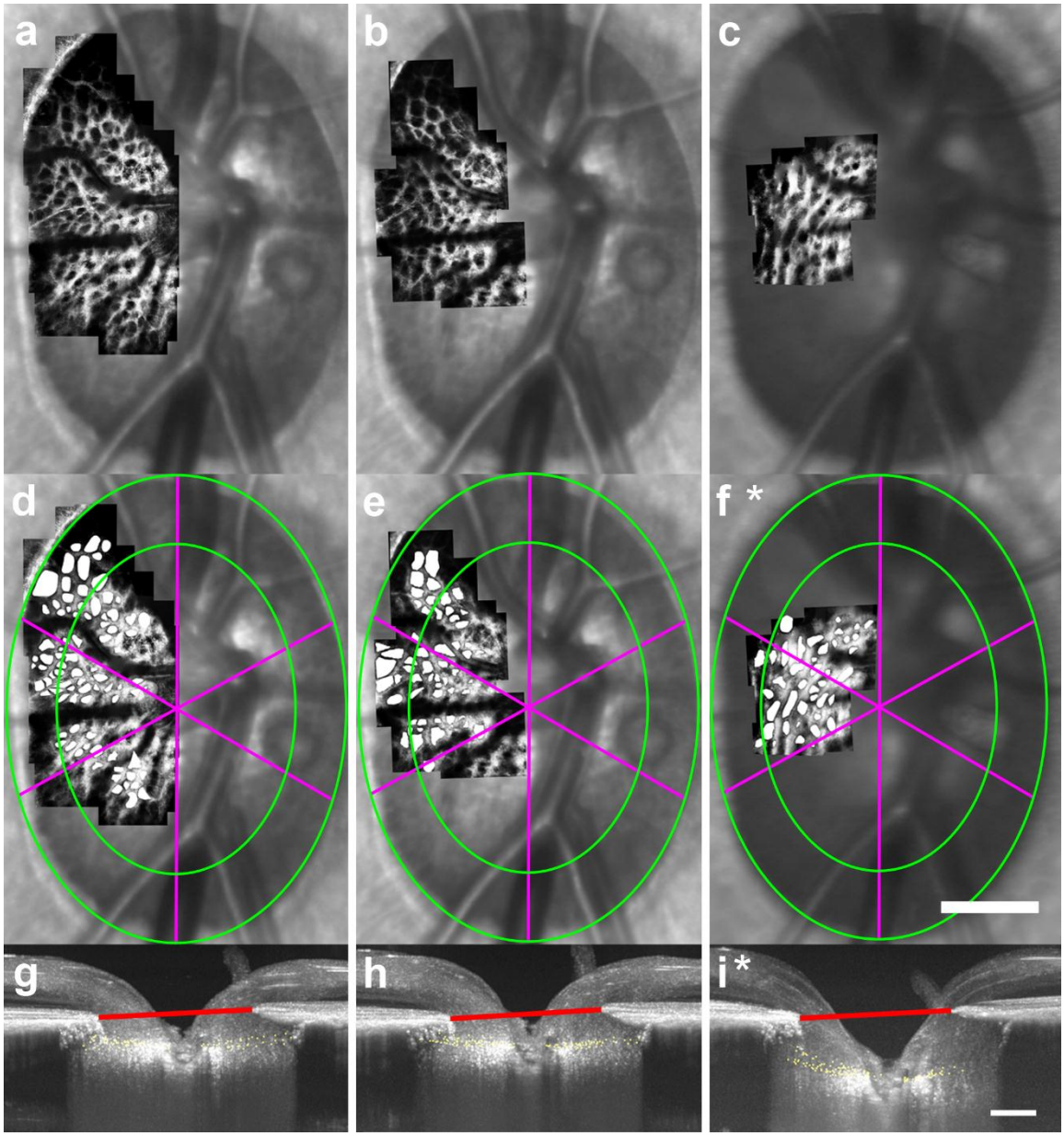


**Figure 4-5.** The first statistically significant measured changes in global and/or local ALCS pore geometry (relative to baseline time-points) occurred simultaneous to the first significant changes measured in mean ALCSD in the EG eye of monkey OHT-64. Images of the (a-c) ALCS microarchitecture and (g-i) ONH were each acquired at baseline (left column), a representative follow-up time-point (middle column, 210 days after the initial laser treatment) that showed no significant change in ALCS pore geometry, and the time-point corresponding to the first significant change (*) in ALCS pore geometry and depth (right-most column, 238 days after the initial laser treatment). (It should be noted that this figure does not include all imaging time-points for this eye.)

(d-f) After marking ALCS pores, mean ALCS pore geometry was quantified globally and locally in central and peripheral regions (green boundaries) and in 60° sectors (fuchsia meridians). Significant increases in ALCS pore geometry were first seen in the central region and superotemporal and temporal sectors at 238 days after the initial laser treatment. (g-i) SDOCT maximum intensity projection images of the ONH showing marked ALCS points (yellow dots) from all B-scans and the BMO reference plane (red line) for the corresponding time-points in (a-c). (i) A significant increase in mean ALCSD was measured simultaneously with (f) the first significant increase in pore geometry. A white asterisk (*) indicates the first significantly measured change in pore or ONH geometry. Scale bar: 350 μm.

respectively), as did mean pore elongation (1.80 ± 0.61 vs. 1.65 ± 0.46), and mean pore NND (52.3 ± 14.5 µm vs. 40.6 ± 12.1 µm). On a local level, mean pore area was significantly larger relative to baseline time-points in the central region (1,174.7 ± 783.2 $\mu m^2$ vs. 716.7 ± 440.1 $\mu m^2$) and in the temporal sector (1,276.2 ± 859.4 $\mu m^2$ vs. 812.4 ± 635.6 $\mu m^2$). Corresponding local increases in mean pore NND were measured relative to baseline time-points in the central region (52.0 ± 14.8 µm vs. 39.3 ± 10.3 µm) and the superotemporal and temporal sectors (50.5 ± 16.8 µm vs. 43.0 ± 11.1 µm and 54.8 ± 10.2 µm vs. 38.4 ± 11.7 µm, respectively), while mean pore elongation significantly increased relative to baseline in the superotemporal sector (1.79 ± 0.59 vs. 1.55 ± 0.34). Similarly, the first statistically significant increase in mean ALCSD relative to baseline (354.3 µm vs. 199.5 µm, respectively) (Fig. 4-5i) occurred simultaneously with the first significant change in pore geometry (Fig. 4-5c,f).

Longitudinal changes in ONH parameters and RNFLT are shown in Fig. 4-6 for all measured time-points in the same EG eye of monkey OHT-64. The first time-point of significant change in ALCS pore geometry (vertical red line) was compared to time-points of first significant change in all ONH parameters and RNFLT (yellow dots). Mean ALCSD (Fig. 4-6a), mean MRW (Fig. 4-6c) and ALCS pore geometry all exhibited their first statistically significant change from baseline values at the same time-point (238 days after the initial laser treatment at day 0). The next parameter to significantly change from baseline was mean RoC (Fig. 4-6b), while RNFLT (Fig. 4-6d) was the last measured parameter to show an initial significant change relative to baseline.

In contrast to the EG eyes of monkeys OHT-64 and OHT-65 in which three structural parameters simultaneously had an initial, significant change in early experimental glaucoma, three EG eyes (OHT-63, OHT-66, and OHT-67) had an initial, significant change in only a single parameter. For example, the first parameter to significantly change from baseline in two EG eyes (OHT-66 and OHT-67) was mean

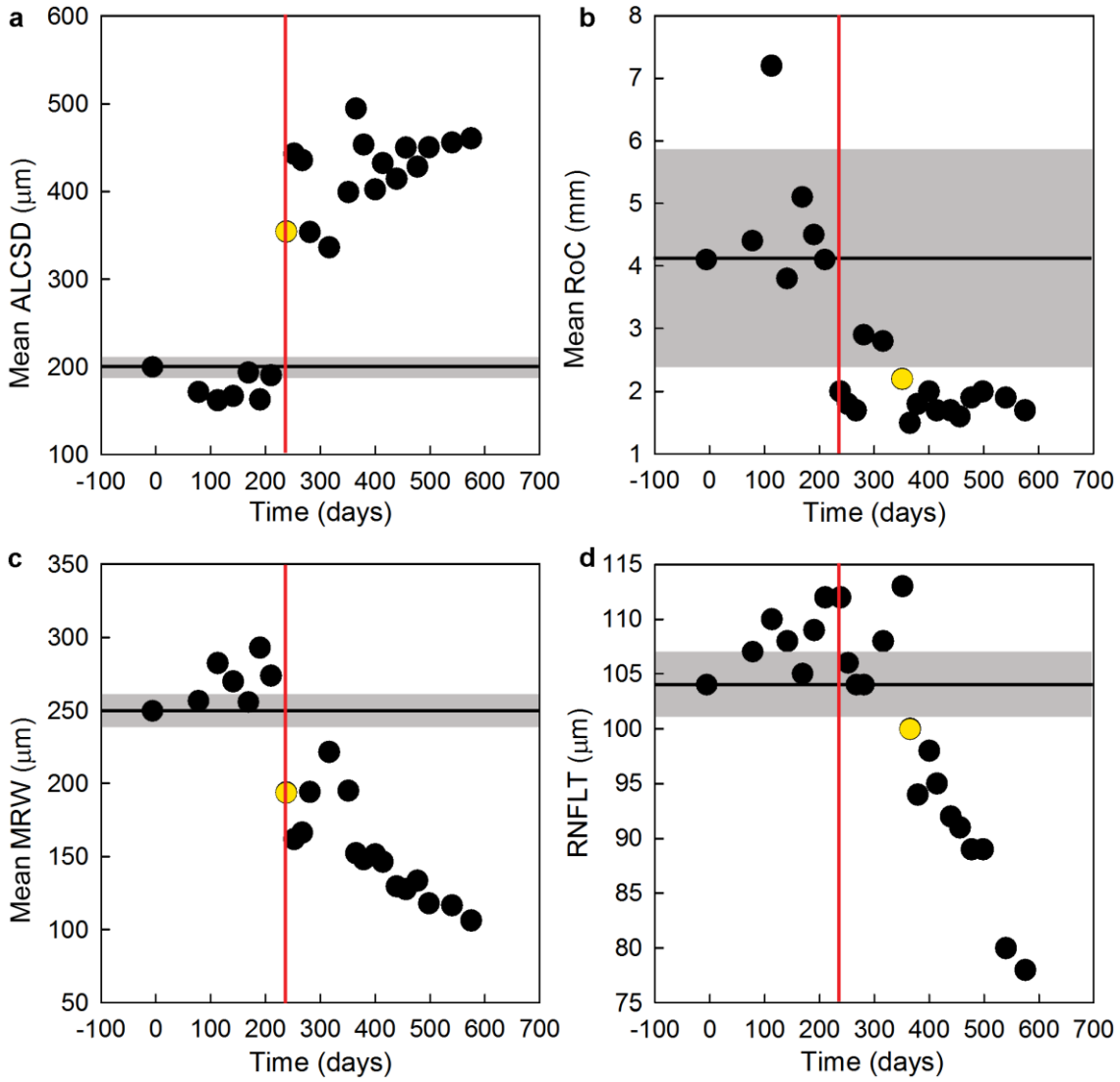


**Figure 4-6.** Early changes in ONH parameters, RNFLT, and ALCS pore geometry in the EG eye of monkey OHT-64. Values for (a) mean ALCSD, (b) mean RoC, (c) mean MRW and (d) RNFLT are shown as a function of study time for all measured time-points (black circles) before and after the initial laser treatment (day 0). The black horizontal line in each plot indicates the baseline value for each parameter while the gray shaded region represents the 95% confidence interval for each parameter calculated from data measured in the fellow control eye. Yellow circles represent the time-point of first significant change in each ONH parameter and RNFLT, while vertical red lines represent the time-point of first significant change in ALCS pore geometry. The first parameters to significantly change from baseline values were (a) mean ALCSD, (c) mean MRW, and ALCS pore geometry (238 days after the initial laser treatment), followed by a significant

change in (b) mean RoC (351 days after the initial laser treatment). (d) RNFLT was the last parameter to show a significant change (365 days after the initial laser treatment**).**

ALCSD. Figure 4-7 shows images of the ALCS microarchitecture and ONH acquired at baseline (left column), the time-point of first significant change in mean ALCSD (middle column), and the time-point of first significant change in ALCS pore geometry (right column) for the EG eye of monkey OHT-66. At 49 days following the initial laser treatment in this EG eye (Fig. 4-7, middle column), a statistically significant increase in mean ALCSD (Fig. 4-7h) was measured relative to baseline (Fig. 4-7g) (174.3 µm vs. 156.3 µm), while no statistically significant differences were measured in any ALCS pore parameter (Fig. 4-7e) on global or local scales relative to baseline (Fig. 4-7d) at the same time-point ($P$>.05). At 168 days following the initial laser treatment (Fig. 4-7, right column), mean ALCSD further increased to 285.1 µm (Fig. 4-7i) while the first significant change in ALCS pore geometry (Fig. 4-7f) was measured relative to baseline. Globally, mean ALCS pore area significantly increased at this time-point relative to baseline (1,169.3 ± 756.4 µm$^2$ vs. 746.8 ± 487.1 µm$^2$, respectively), as did mean pore NND (41.3 ± 11.4 µm vs. 34.2 ± 9.9 µm, respectively). However, mean pore elongation significantly decreased relative to baseline (1.70 ± 0.50 vs. 1.78 ± 0.73, respectively), On a local level, mean ALCS pore area significantly increased relative to baseline time-points in the central (917.3 ± 545.4 µm$^2$ vs. 703.0 ± 382.5 µm$^2$, respectively) and peripheral (1,456.1 ± 864.1 µm$^2$ vs. 865.7 ± 561.0 µm$^2$, respectively) regions and in the superotemporal (1,548.8 ± 1029.2 µm$^2$ vs. 890.7 ± 470.9 µm$^2$, respectively) and temporal (1,020.0 ± 591.3 µm$^2$ vs. 712.4 ± 482.5 µm$^2$, respectively) sectors. Corresponding local increases in mean pore NND were measured relative to baseline time-points in central (37.1 ± 9.8 µm vs. 33.7 ± 9.6 µm, respectively) and peripheral (46.0 ± 11.4 µm vs. 36.3 ± 8.8 µm, respectively) regions and in the superotemporal (44.9 ± 9.7 µm vs. 35.7 ± 9.3 µm, respectively) and temporal (38.6 ± 11.9 µm vs. 34.0 ± 9.6 µm, respectively) sectors, while mean pore elongation was significantly decreased

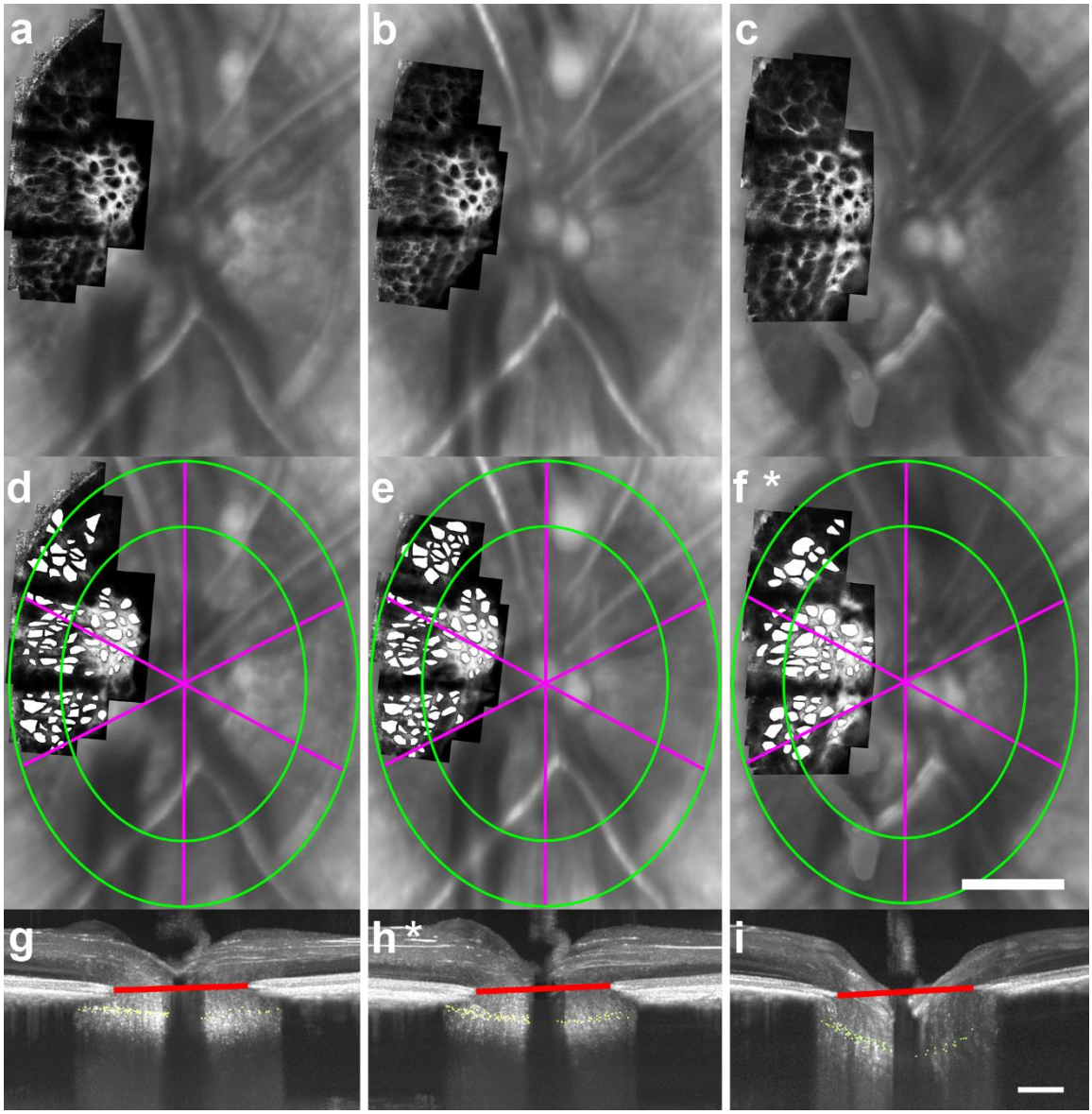


**Figure 4-7.** The first statistically significant measured change in mean ALCSD (relative to baseline time-points) occurred prior to the first significant change in global and/or local ALCS pore geometry in the EG eye of monkey OHT-66. Images of the (a-c) ALCS microarchitecture and (g-i) ONH were each acquired at baseline (left column), a later time-point (middle column, 49 days after the initial laser treatment) that showed the first statistically significant change (*) in mean ALCSD, and a later time-point corresponding to the first significant change (*) in ALCS pore geometry (right-most column, 168 days after the initial laser treatment). (It should be noted that this figure does not include all imaging time-points for this eye.) (d-f) After marking ALCS pores, mean ALCS pore geometry was quantified globally and locally in central

and peripheral regions (green boundaries) and in 60° sectors (fuchsia meridians). Significant increases in ALCS pore geometry were first seen in central and peripheral regions and superotemporal, temporal, and inferotemporal sectors at 168 days after the initial laser treatment. (g-i) SDOCT maximum intensity projection images of the ONH showing marked ALCS points (yellow dots) from all B-scans and the BMO reference plane (red line) for the corresponding time-points in (a-c). (h) A significant increase in mean ALCSD was measured prior to (f) the first significant change in ALCS pore geometry. A white asterisk (*) indicates the first significantly measured change in pore or ONH geometry. Scale bar: 350 μm.

relative to baseline values in the temporal (1.80 ± 0.49 vs. 1.86 ± 0.79, respectively) and inferotemporal (1.36 ± 0.17 vs. 1.60 ± 0.45, respectively) sectors.

Longitudinal changes in ONH parameters and RNFLT measured in the same EG eye of monkey OHT-66 are shown in Fig. 4-8 for all time-points. The first structural parameter to significantly change relative to baseline values was mean ALCSD (Fig. 4-8a), followed by an initial, statistically significant change in mean RoC (Fig. 4-8b). ALCSpore geometry and mean MRW (Fig. 4-8c) next exhibited their first significant changes relative to baseline values at the same time-point. Again, similar to results presented in the EG eye of OHT-64, RNFLT (Fig. 4-8d) was the last measured parameter to show its first significant change from baseline.

The time-course of the first significant changes measured in ALCS pore geometry, ONH parameters, and RNFLT relative to baseline is summarized in Fig. 4-9 for all 7 EG eyes. A sole change in MRW occurred first in one EG eye (OHT-63) while a sole change in mean ALCSD occurred first in two EG eyes (OHT-66 and OHT-67). Simultaneously changes in mean ALCSD and mean MRW occurred first in two EG eyes (OHT-68 and OHT-69) while simultaneous increases in mean ALCSD, mean MRW, and ALCS pore geometry occurred first in the remaining two EG eyes (OHT-64 and OHT-65). Based on these results, mean ALCSD increased first in 6 out of 7 EG eyes, with 4 eyes showing a simultaneous decrease in MRW and 2 eyes showing a simultaneous change in ALCS pore geometry. For EG eyes in which statistically significant changes were measured in all ONH parameters, ALCS microarchitecture, and RNFLT by the end of the study, RNFLT was the last parameter to change in 3 EG eyes while mean RoC was the last parameter to significantly change in 2 EG eyes. Simultaneously significant changes in mean RNFLT and mean RoC were the last changes to occur in 1 EG eye.

The time-points of first significant change in mean ALCSD and ALCS pore microarchitecture are overlaid on a plot illustrating the difference in IOP between the EG

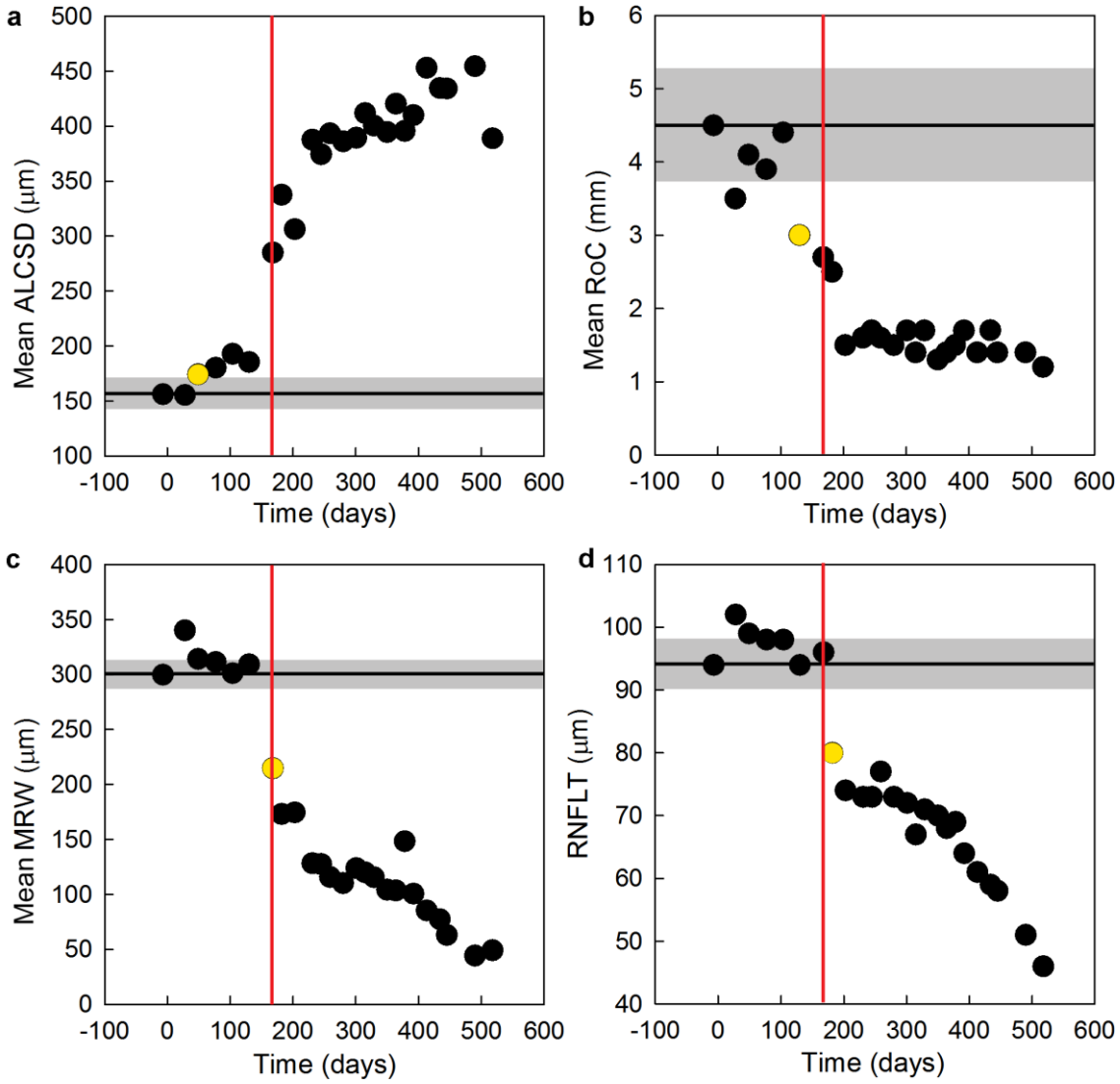


**Figure 4-8.** Early changes in ONH parameters, RNFLT, and ALCS pore geometry in the EG eye of monkey OHT-66. Values for (a) mean ALCSD, (b) mean RoC, (c) mean MRW, and (d) RNFLT are shown as a function of study time for all measured time-points (black circles) before and after the initial laser treatment (day 0). The black horizontal line in each plot indicates the baseline value for each parameter while the gray shaded region represents the 95% confidence interval for each parameter calculated from data measured in the fellow control eye. Yellow circles represent the time-point of first significant change in each ONH parameter and RNFLT, while vertical red lines represent the time-point of first significant change in ALCS pore geometry. The first parameter to significantly change from baseline values was (a) mean ALCSD (49 days after the initial laser treatment). The next parameter to significantly change from baseline was (b) mean

RoC (130 days after the initial laser treatment), followed by simultaneous significant changes in ALCS pore geometry and mean MRW (168 days after the initial laser treatment). RNFLT was again the last measured parameter to significantly change (182 after the initial laser treatment).

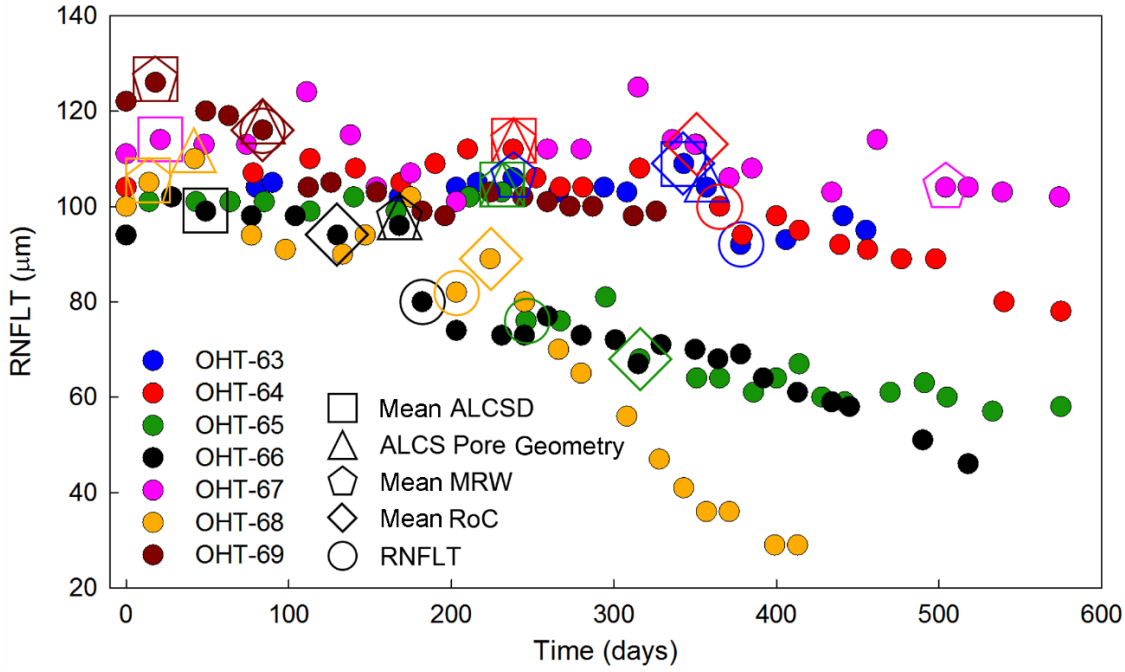


**Figure 4-9.** Summary of the time-course for when the first significant change was measured (relative to baseline values) for ONH parameters, ALCS pore geometry, and RNFLT in all EG eyes. RNFLT values are plotted as a function of study time for all measured time-points (filled circles with each color representing a different EG eye). A progressive decrease in RNFLT was measured throughout the course of the study for all EG eyes except OHT-67 (which also showed no significant change in ALCS pore geometry, mean RoC, and RNFLT). One of the first significant structural changes to be measured in EG eyes was an increase in mean ALCSD (square symbol, 6 of 7 EG eyes). A significant decrease in mean MRW (pentagon symbol) simultaneously accompanied this early change in 4 eyes and was the first, sole significant structural change in 1 of 7 EG eyes. A significant change in mean ALCS pore geometry (triangle symbol) occurred first in 2 of 7 EG eyes.

eye (after being lowered pharmacologically) and fellow control eye in all monkeys at each imaging time-point in the study (Fig. 4-10). The mean difference in IOP across all monkeys at the first time-point of significant change in mean ALCSD was 5.0 ± 7.7 mmHg and ranged from -1 to 9 mmHg in all monkeys except for OHT-63 (20 mmHg). Mean ALCSD in OHT-63 increased from a baseline value of 249.9 μm to 409.6 μm at the first time-point of change when the IOP difference was 20 mmHg. However, mean ALCSD remained significantly high and different from baseline at the next two imaging time-points (332.8 μm and 345.2 μm) when the differences in IOP between the EG and control eyes were small (6 mmHg and 5 mmHg, respectively), indicating that the change in mean ALCSD measured at the time-point of first significant change was largely due to a chronic change in pressure and not a temporary spike in IOP. Similarly, the mean difference in IOP across all monkeys at the first time-point of significant change in ALCS pore geometry was 7.2 ± 6.9 mmHg and ranged from 0 to 9 mmHg in all monkeys except for OHT-69 (20 mmHg). Substantial alterations in ALCS beam and pore structure were observed at the time-point of first significant change relative to baseline in OHT-69 (Fig. 4-11a,b). Despite the fact that the IOP difference between the EG and control eyes was high (20 mmHg), we believe the changes in ALCS microarchitecture measured at this time of first significant change were largely chronic and permanent as a similar beam and pore structure was observed in the EG eye at a subsequent imaging time-point (Fig. 4-11c) when the IOP difference was low (4 mmHg). In addition, the fact that the ALCS microarchitecture did not revert back to its normal, baseline structure at subsequent time-points when the IOP difference was low further supports the idea that the alterations measured at the first time-point of significant change were primarily due to a permanent remodeling of beams and pores.

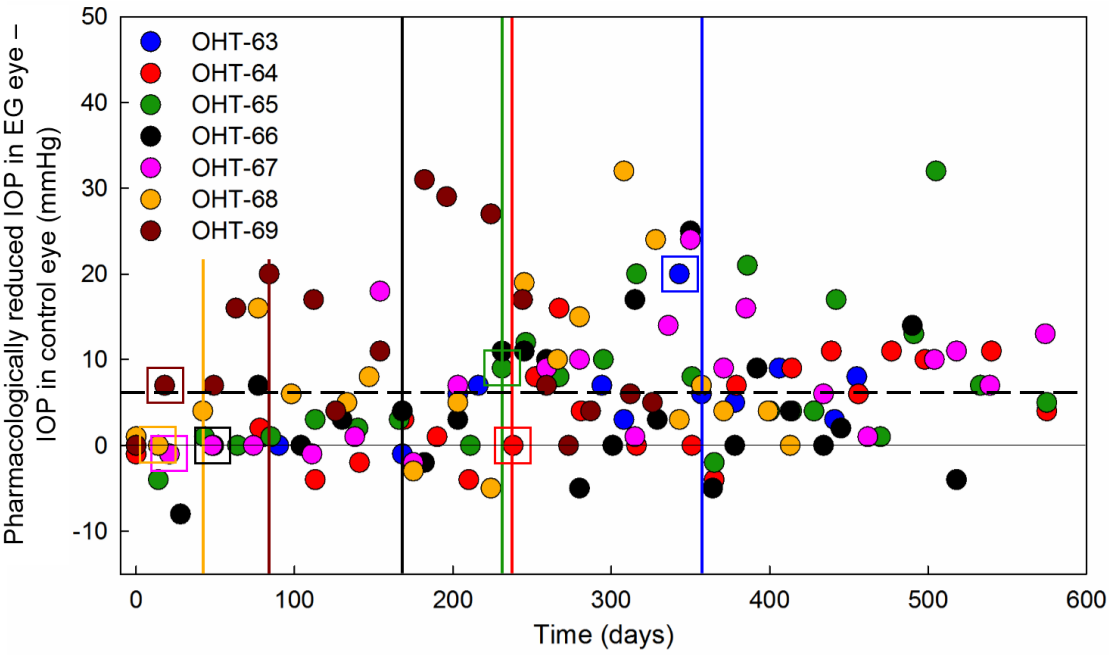


**Figure 4-10.** Summary of the time-course for when the first significant change was measured (relative to baseline) for mean ALCSD (square symbols) and ALCS pore geometry (vertical lines) in all EG eyes. Differences in IOP between the EG eye (following pharmacological reduction) and the control eye are plotted as a function of study time (filled circles with each color representing a different monkey) to illustrate the pressure difference between the EG and control eyes when the first significant changes were measured in mean ALCSD and pore geometry for each monkey. The dashed horizontal black line represents the mean IOP difference across all monkeys and the solid horizontal black line represents an IOP difference of 0 mmHg. (OHT-67 showed no significant change in ALCS pore geometry throughout the duration of the experiment.)

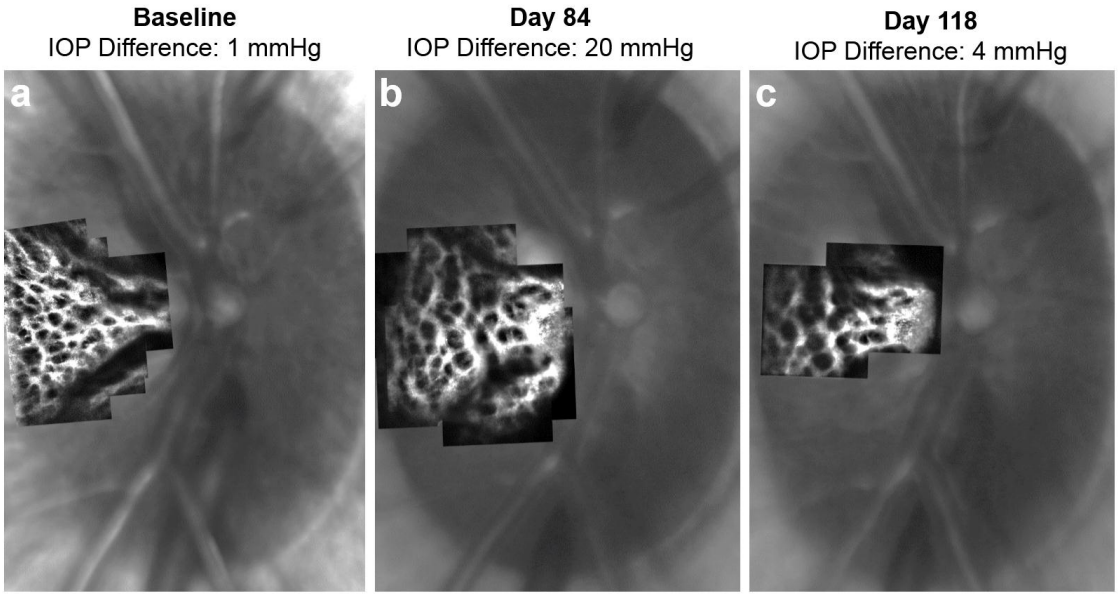


**Figure 4-11.** Images of ALCS microarchitecture in the EG eye of OHT-69 at (a) baseline, (b) the time-point of first significant change in ALCS pore geometry (day 84) and (c) a subsequent time-point 34 days later. (b) Substantial alterations in ALCS beam and pore structure were observed at the time-point of first significant change relative to baseline (a). (c) A similar beam and pore structure was observed 34 days after (b) when the difference in IOP between the control and EG eyes (after being reduced by a pharmacological agent) was small (4 mmHg), indicating the changes in ALCS microarchitecture first observed at (b) when the IOP difference was very large (20 mmHg) were chronic and not due to an acute elevation in IOP (or an insufficient reduction in IOP) in the EG eye at the time-point of first significant change.

## 4.4 Discussion

This study characterizes the time-course of microarchitectural changes in anterior lamina cribrosa surface pore geometry concurrent with structural changes in the ONH and RNFL during early experimental glaucoma. In this monkey model, IOP was elevated unilaterally (with the fellow eye serving as a control) via a gradual laser ablation of the trabecular meshwork. The maximum IOP when averaged across all EG eyes was 50.4 ± 4.8 mmHg (Table 4-1). When compared to the mean IOP averaged across all control eyes (13.2 ± 1.4 mmHg), there was a +282% mean difference in the maximum IOP experienced by our EG eyes relative to mean values in control eyes. The relative increases in maximum IOP measured in our EG eyes are comparable to those reported in other studies. For example, Fortune et al. reported an average peak IOP of 41.0 ± 10.7 mmHg in EG monkey eyes compared to a mean IOP of 10.8 ± 1.7 mmHg in control eyes, reflecting a +280% mean difference in maximum IOP values relative to mean values in controls (Fortune et al, 2013a). Similarly, Downs et al. measured a +241% mean difference between maximum IOP values in monkeys eyes with unilateral EG and mean IOP values in the fellow control eyes (Downs et al, 2001). Due to the fact that IOP levels can become high in the monkey model of experimental glaucoma, it is important to lower IOPs in EG eyes to “normal” levels when imaging the ONH to examine chronic changes in ONH and laminar structure that result from sustained elevations in IOP. Prior to *in vivo* imaging in our EG eyes, IOPs were pharmacologically reduced to levels that were, on average, only 6 mmHg higher than mean IOP values in fellow control eyes (Table 4-1). Imaging ONH and laminar parameters in EG eyes with pressures that were reduced nearly to normal values better ensured that the structural changes measured in the ONH and lamina cribrosa were the result of a chronic elevation in IOP and not a temporary or acute spike in pressure.

*In vivo* measurements of mean ALCSD and lamina cribrosa microarchitecture made in our normal control eyes and EG eyes at baseline are similar to values reported in previous studies. The average value of mean ALCSD calculated across all control eyes was 214.0 ± 25.3 µm and is comparable to earlier *in vivo* measurements of mean ALCSD made in normal monkey eyes (~ 220 - 230 µm) (Strouthidis et al, 2011a; Strouthidis et al, 2011b; Yang et al, 2012). Average values of mean ALCS pore geometry measured at baseline in this study across all control eyes except for monkey OHT-65 (mean pore area = 871.9 ± 181.8 $\mu m^2$; mean pore elongation = 1.69 ± 0.05; mean pore NND = 37.7 ± 6.5 µm) and across all EG eyes (mean pore area = 838.0 ± 130.1 $\mu m^2$; mean pore elongation = 1.71 ± 0.13; mean pore NND = 37.2 ± 2.6 µm) are similar to previous *in vivo* measurements of laminar pore geometry made in normal non-human primate eyes (Ivers et al, 2011; Vilupuru et al, 2007). To our knowledge, we report the first values of mean MRW and mean RoC (average values of 308.7 ± 55.1 µm and 3.6 ± 1.0 mm, respectively) in normal (control) monkey eyes. While the coefficients of variation in RNFLT, mean ALCSD, and mean MRW were small in all control eyes throughout the entire experiment (<6.5%), the average coefficient of variation in mean RoC across all control eyes was larger (21.7 ± 7.6%) (Table 4-1). One potential reason for the increased variability observed in mean RoC in control (i.e., normal) eyes is that the ALCS tends to be relatively flat in normal monkey eyes (Sredar et al, 2013) and RoC measurements are likely prone to higher variability when assessed on flatter surfaces. For example, values of mean RoC can be rather large for flat surfaces (approaching infinity for a perfectly flat surface). Therefore, small variations in the degree of laminar "flatness" could have a large impact in the mean value of RoC measured at a given time-point and potentially result in a high variability in this parameter when measured over time in normal eyes. Additionally, the amount of prelaminar tissue in the ONH is typically thickest at the edge of the neuroretinal rim,

making it more challenging to visualize and quantify the surface curvature of the ALCS toward the periphery of the ONH in normal eyes and potentially increasing measurement variability when examining the same normal eyes longitudinally at multiple time-points. Despite the relatively higher variability in mean RoC in control eyes, we believe it is still important to examine changes in mean RoC in combination with changes in mean ALCSD to better characterize the shape of the ALCS, especially in EG eyes. The use of a single parameter (such as mean ALCSD) provides only a partial characterization of the ALCS as it is possible to have 2 anterior laminar surfaces with very different mean RoCs (indicating different curved surfaces) but the same mean ALCSD (Sredar et al, 2013).

Significant changes in ONH parameters (mean ALCSD, mean RoC, and mean MRW) and RNFLT were measured throughout the duration of the study in EG eyes. At time-points corresponding to the first significantly measured change in each parameter relative to baseline values, there was a +38% average increase in mean ALCSD (i.e., a more posteriorly displaced ALCS), -55% average decrease in mean RoC (i.e., a more steeply curved ALCS), and -19% and -13% average decreases in mean MRW and RNFLT (i.e., a loss of RNFL axons), respectively, across all EG eyes. These initial changes further increased during the progression of experimental glaucoma. At the final imaging time-points for each monkey, we measured a 133% average increase in mean ALCSD (i.e., an even more posteriorly-displaced ALCS), -70% average decrease in mean RoC (i.e., an even more steeply curved ALCS), and -61% and -34% average reductions in mean MRW and RNFLT (i.e., an increased loss of RNFL axons), respectively, across all EG eyes.

In addition to measuring longitudinal changes in ONH and RNFL structure, we report the first *in vivo* longitudinal changes in lamina cribrosa microarchitecture in non-human primates with experimental glaucoma. When examining laminar pore parameters on a global scale, mean ALCS pore area and NND significantly increased across all EG

eyes (*P*<.05). Statistically significant increases were also measured in mean ALCS pore area on a local scale at the first time-point of change (relative to baseline) in the temporal sector (+35.5%) and in central (+23.6%) and peripheral (+29.9%) regions (Table 4-4). Corresponding increases in mean ALCS pore NND were also measured at the first time-point of significant change in the superotemporal (+13.2%) and temporal (+17.1%) sectors, as well as in central (+11.6%) and peripheral (+22.4%) regions, while no statistically significant changes were measured in pore elongation for any regions or sectors. These findings indicate that ALCS pores become larger and further separated globally, temporally, centrally, and peripherally at the time-point of first significant change in ALCS pore microarchitecture in early EG.

The first statistically significant changes in ALCS pore geometry measured in our study (i.e., increased pore area and NND) are similar to differences in ALCS pore geometry described in glaucomatous eyes in recent cross-sectional studies. Vilupuru et al. acquired *in vivo* images of ALCS pores at a single time-point in 3 monkey eyes with moderate to advanced stages of experimental glaucoma (i.e., mean deviations > -6.5 dB) and found statistically significantly increased values of mean ALCS pore area in all EG eyes, pore elongation in 1 EG eye, and NND in 2 EG eyes (relative to fellow control eye values) (Vilupuru et al, 2007). Similar to our finding of no significant change in pore elongation at the first time-point of significant change in overall pore geometry, Wang et al. reported no significant differences in laminar pore aspect ratio (or elongation) between healthy and glaucomatous human patients imaged using swept-source OCT at a single time-point (Wang et al, 2013).

When characterizing the time-course of first significant change in RNFLT, ONH parameters and ALCS microarchitecture, mean ALCSD, mean MRW, and mean ALCS pore geometry (quantified globally and locally) were always among the first 3 parameters to change in our EG eyes. Mean ALCSD was the first parameter (or one of the first

parameters) to statistically significantly change from baseline in 6 of 7 EG eyes. Mean MRW simultaneously decreased in 4 of these 6 eyes and was the sole parameter to first change in the 7$^{th}$ EG eye. Conversely, RNFLT was the last or second to last parameter to change in 6 EG eyes. (No significant change in RNFLT was measured in the 7$^{th}$ EG eye, OHT-67, throughout the entire study duration.) These results agree with previous studies that have also found mean ALCSD and mean MRW to change prior to a change in RNFLT. For example, Strouthidis et al. measured an increase in mean ALCSD prior to a reduction in RNFLT in 9 monkey eyes with unilateral experimental glaucoma (Strouthidis et al, 2011b). In addition, He et al. found that changes in mean ALCSD and MRW occurred prior to the first detectable loss in RNFLT or loss in multifocal electroretinogram (mfERG) measures of visual function in 8 monkey eyes with unilateral experimental glaucoma (He et al, 2014). In combination with our study, these works collectively suggest that mean MRW could potentially represent an improved and more sensitive surrogate marker for axonal integrity compared to RNFLT. Moreover, the results of our study build on the aforementioned studies by providing the first characterization of the onset of changes in ALCS microarchitecture in combination with changes in ONH parameters and RNFLT. We found that ALCS pore geometry was one of the first or second structural changes to be measured in 4 of 6 early EG eyes.

The first significant change in ALCS pore geometry (on global or local scales) was measured *after* the time-point of first significant change in mean ALCSD in 4 of 6 EG eyes. (No significant change in ALCS pore geometry was measured relative to baseline values in one EG eye throughout the entire duration of the study.) Several reasons could potentially account for the fact that simultaneous changes in mean ALCSD and mean ALCS pore parameters did not occur in more EG eyes. First, as previously discussed, a uniform posterior displacement of the laminar surface (i.e., an increase in mean ALCSD with minimal change in mean RoC) could result in an anterior

laminar surface shape that is relatively unaltered from baseline conditions and a negligible change in ALCS pore geometry. Second, overlying vasculature and the neuroretinal rim cast shadows onto the ALCS microarchitecture and mask our ability to image the most superior, inferior, and peripheral portions of the laminar surface. Consequently, laminar pores were typically visualized over more central/mid-peripheral regions of the ALCS, resulting in an increased number of pores that were imaged along the flatter, more central portion of the ALCS compared to the more steeply sloped portions of the ALCS at the periphery of the lamina. Therefore, we likely did not observe changes in the most peripherally located ALCS pores within the ONH where one might expect to see even larger changes in pore geometry associated with a posterior movement in the ALCS in early EG. Third, it is possible that laminar pore geometry did not significantly change at the anterior laminar surface, but was potentially altered at a greater depth than was visualized in this study. In future studies, it will be important to image and examine laminar pore microarchitecture at various laminar depths at baseline and follow-up time points in order to fully characterize changes in laminar beams and pores throughout the entire depth of the lamina in early experimental glaucoma.

Finally, some EG eyes demonstrated more rapid changes in ONH and laminar parameters compared to other EG eyes. For example, early changes in ONH and laminar structure occurred very quickly in the EG eye of monkey OHT-69, as the first statistically significant changes in ONH parameters (mean ALCSD, RoC, and MRW), mean ALCS pore parameters, and RNFLT relative to baseline values occurred within 84 days of the initial laser treatment (Fig. 4-9). Conversely, early changes in ONH and laminar structure occurred very slowly (or not at all) in the EG eye of monkey OHT-67. While an initial significant change in mean ALCSD was measured 21 days after the initial laser treatment, this EG eye showed an initial significant change in mean MRW 504 days after the initial laser treatment with no statistically significant changes in RNFLT,

mean RoC, and ALCS pore microarchitecture for the entire study (Figure 4-9). A possible reason for this discrepancy in progression rates could be due to different compliance levels in the lamina cribrosa between eyes. The fact that the EG eye of monkey OHT-67 had a significant initial increase in mean ALCSD but no significant change in mean RoC or ALCS pore geometry suggests that the lamina migrated posteriorly in the neural canal without significantly changing its surface shape (i.e., a more uniform posterior displacement), potentially as a result of an increased compliance (or decreased resistance) of the lamina after chronic exposure to elevated IOP. The resistance to change demonstrated by the lamina exhibited in the EG eye of monkey OHT-67 was not observed in the EG eye of monkey OHT-69, in which significant initial increases were measured soon after the initial laser treatment in all laminar-related parameters (mean ALCSD, mean RoC, and mean ALCS pore parameters).

In conclusion, significant structural changes in mean ALCSD, mean MRW, and ALCS pore geometry occurred prior to significant losses in RNFLT in early EG eyes. Moreover, the fact that local changes in ALCS pore geometry were measured before a global change in the same parameter in 3 EG eyes suggests that local analyses can play an important role in detecting earlier changes in laminar microarchitecture while also providing insights on biomechanical remodeling of the lamina on a local level during the progression of experimental glaucoma.

### 4.5 Acknowledgements

The authors thank Harold Bedell, Claude Burgoyne, Crawford Downs, and Michael Twa for their helpful discussions.

# CHAPTER 5

## Comparison of structural changes in the optic nerve head and lamina cribrosa microarchitecture with functional measures of vision loss in non-human primates with experimental glaucoma

**Contributing authors:**

Lakshmi Rajagopalan, Nimesh B. Patel, OD, PhD, Ronald S. Harwerth, OD, PhD, Laura J. Frishman, PhD, and Jason Porter, PhD

**Abstract**

**Purpose:** To characterize the onset and time-course of structural and functional changes in non-human primates with early experimental glaucoma (EG).

**Methods:** Adaptive optics scanning laser ophthalmoscope (AOSLO) images of anterior lamina cribrosa surface (ALCS) microarchitecture and spectral domain optical coherence tomography (SDOCT) images of the optic nerve head (ONH) and the peripapillary retinal nerve fiber layer (RNFL) were acquired in fellow eyes before and approximately every 2 weeks after inducing unilateral EG in 3 rhesus monkeys. In parallel, multifocal electroretinograms (mfERGs) and standard automated perimetry (SAP) tests were recorded in fellow eyes to measure reductions in the amplitude of the multifocal photopic negative response (mfPhNR) and in visual field sensitivity, respectively. Control eye and/or baseline EG eye data were used to assess the onset of change in ONH structure [mean ALCS depth (ALCSD) and mean minimum rim width (MRW)], along with ALCS pore microarchitecture, RNFL thickness (RNFLT), mfPhNR amplitude, and visual field sensitivity on a sector level in all monkeys.

**Results:** Mean ALCSD was the first structural or functional parameter to have a statistically significant change in 2 of 3 EG eyes, while a reduction in the mfPhNR amplitude was measured first in the third EG eye. A change in the mfPhNR amplitude occurred prior to a change in laminar pore microarchitecture in 2 of 3 monkeys with unilateral EG, while one monkey had simultaneous changes in mfPhNR amplitude and pore geometry. In all monkeys, sectoral RNFLT and visual field sensitivity were the last parameters to show an initial change.

**Conclusions:** Significant increases in anterior laminar surface position (mean ALCSD), laminar pore microarchitecture, and mfPhNR amplitude were measured prior to significant losses in RNFLT and visual field sensitivity. A larger number of EG eyes will need to be examined to reinforce these preliminary findings. AOSLO and SDOCT structural imaging and mfERG functional recording provide the opportunity to earlier detect glaucomatous damage.

## 5.1 Introduction

Glaucoma, the second leading cause of blindness worldwide (Quigley & Broman, 2006), is a disease that results in the death of retinal ganglion cells (RGCs) and causes a slowly progressive, irreversible loss of visual function. While a large body of work suggests that the location of initial insult to RGC axons in glaucoma occurs in the optic nerve head (ONH) at the level of the lamina cribrosa, the mechanisms underlying this damage are not fully understood (Bellezza et al, 2003; Burgoyne et al, 2004; Gaasterland et al, 1978; Minckler et al, 1977; Quigley et al, 1981; Quigley & Green, 1979). Conventional measures used clinically to detect and assess the progression of glaucoma focus primarily on changes in ONH cupping and losses in retinal nerve fiber layer thickness (RNFLT) and visual function. However, it is estimated that 40-50% of retinal ganglion cells (RGCs) are non-functional by the time current clinical tests, such as visual field testing measured via standard automated perimetry (SAP), reliably detect vision loss (Harwerth et al, 1999). Similarly, recent work has shown that 10-15% of RGC axons are already lost when a first change in RNFLT is reliably detected with spectral domain optical coherence tomography (SDOCT) (Cull et al, 2012). It is crucial to develop earlier markers for detecting glaucomatous damage that allow for more informed clinical decision-making about treatment.

Recent longitudinal studies have sought to better characterize the earliest structural and functional changes that occur *in vivo* in experimental models of glaucoma. For example, an increase in the mean anterior lamina cribrosa surface depth (ALCSD) (i.e., more posterior displacement of the surface in the ONH) has been shown to precede both a measurable change in the mfERG signal (He et al, 2013) and a loss in RNFLT (Strouthidis et al, 2011b). In addition, a change in RNFL retardance (measured via scanning laser polarimetry [SLP]) and a change in the mfERG signal have been shown to occur before a change in ONH surface topography (i.e., a change in the mean

position of the disc and/or a subjectively-noted change in the topographic change analysis [TCA] map) and a decrease in RNFLT (Fortune et al, 2013; Fortune et al, 2012). These and other studies (Harwerth et al, 2002; Rangaswamy et al, 2006; Viswanathan et al, 1999; Viswanathan et al, 2001) provide evidence for structural and functional measures that occur earlier than RNFLT loss in glaucoma and suggest the need to examine global and local changes in lamina cribrosa geometry in concert with multiple structural and functional measures of vision in early glaucoma.

We sought to build on the aforementioned studies by longitudinally examining and comparing early *in vivo* structural changes in the ONH, anterior lamina cribrosa surface pore microarchitecture, and RNFL with functional changes in SAP (to measure visual field sensitivity) and the mfERG (to measure the light-adapted multi-focal photopic negative response [mfPhNR]) in 3 non-human primates with unilateral experimental glaucoma. Statistical tests were performed to determine the onset of change in all structural and functional parameters measured. The results provide preliminary evidence that changes in lamina cribrosa geometry occur prior to other structural or functional changes in most eyes. This chapter provides improved understanding of the time-course of structural and functional changes that occur in early experimental glaucoma.

**5.2 Methods**

All animal care experimental procedures were approved by the University of Houston's Institutional Animal Care and Use Committee and adhered to the ARVO Statement for the Use of Animals in Ophthalmic and Vision Research.

Structural and functional examinations of the lamina cribrosa, ONH, RNFL, and visual field sensitivity were performed *in vivo* in fellow eyes of 3 rhesus monkeys (*Macaca mulatta*; OHT-64, OHT-66, OHT-69) induced with unilateral experimental glaucoma (EG). Intraocular pressure was elevated by argon laser treatment of the

trabecular meshwork in right eyes (Gaasterland & Kupfer, 1974; Harwerth et al, 1997; Pederson & Gaasterland, 1984; Quigley & Hohman, 1983), while left eyes were used as controls. Mean age (± SD) of the 3 monkeys at the time-point of first-laser treatment was 3.9 ± 0.5 years.

### *5.2.1 Structural parameters: Spectral domain optical coherence tomography (SDOCT) and adaptive optics scanning laser ophthalmoscope (AOSLO) imaging and analysis*

Monkeys were anesthetized with 20-25 mg/kg ketamine, 0.8-0.9 mg/kg xylazine, and 0.04 mg/kg atropine sulfate to minimize eye movements during *in vivo* imaging (Frishman et al, 1996). Pupils were dilated with 2.5% phenylephrine and 1% tropicamide. Before each imaging session, a pharmacological agent (IOPIDINE; Alcon Laboratories, Inc., Fort Worth, TX, USA or COMBIGAN; Allergan, Inc., Irvine, CA, USA) was used to reduce intraocular pressures (IOPs) in EG eyes to levels at or near baseline values. The methods used to support the monkey head and align monkey pupils during SDOCT and AOSLO imaging have been previously described (Chapter 3). Structural imaging was performed once before the first laser session (baseline) and approximately every 2 weeks thereafter. Biometric measurements (axial length, anterior chamber depth, and anterior corneal curvature) were recorded at every time-point (IOLMaster; Carl Zeiss Meditec, AG, Jena, Germany) and incorporated into a three-surface schematic eye with published measures of lens thicknesses and curvatures corresponding to each monkey's age (Qiao-Grider et al, 2007) to laterally scale SDOCT and AOSLO images in each eye (Ivers et al, 2011).

At all time-pointes, SDOCT (Spectralis HRA+OCT; Heidelberg Engineering, Heidelberg, Germany) was used to acquire 30° x 30° scanning laser ophthalmoscope (SLO) images (for AOSLO and SDOCT image registration), along with 12° circular scans

and forty-eight 20° radial B-scans centered on the ONH (to calculate RNFLT and ONH parameters, respectively) in control and EG eyes as previously described (Chapter 4). SDOCT circular scans of the RNFL were divided into 10 sectors of equal length (Fig. 5-1d) to match the sector locations developed by Harwerth et al. (Harwerth et al, 2007) for mapping visual field testing locations (Fig. 5-1a,b) onto the corresponding sector their RGC axons are believed to project to in the ONH (Fig. 5-1c) and contribute to RNFLT measures. Mean values of RNFLT were calculated for each of the 10 sectors. (RNFLT sector calculations were performed by Dr. Laura Frishman's laboratory.) The anterior lamina cribrosa surface (ALCS) and Bruch's membrane opening (BMO) were manually marked in as many radial B-scans as possible using a custom program (MATLAB; The MathWorks, Inc., Natick, MA). A thin-plate spline surface was fit to the marked ALCS point cloud (Sredar et al, 2013) and used to calculate mean ALCSD, the mean distance between a plane best-fit to the marked BMO points and the thin-plate spline surface. In addition, the internal limiting membrane (ILM) was automatically segmented using the SDOCT instrument's software and manually corrected to determine mean minimum rim width (MRW), the minimum distance between each BMO point and the ILM averaged across all radial B-scans.

The methods used for AOSLO imaging have been previously described (Ivers et al, 2011) (Chapter 4). In brief, 840 nm reflectance videos of the ALCS were acquired using an AOSLO over a 1.5° field at a rate of 25 Hz in fellow eyes of all monkeys (Ivers et al, 2011; Li et al, 2010a; Sredar et al, 2013). Registered images from AOSLO videos were combined to generate montages of the ALCS (Adobe Photoshop; Adobe Systems, San Jose, CA). Equivalent ALCS locations were imaged in fellow eyes at every time-point. Pore area, elongation, and nearest neighbor distance (NND) were quantified globally and within sectors following 3D-transformation of AOSLO montages of the ALCS on the thin-plate spline surface (Chapter 3) in all EG eyes (Sredar et al, 2013). For

sector analyses of ALCS pore parameters, the ONH was divided into ten, 36° sectors defined by the minor axis of the BMO ellipse (Fig. 5-1e) to again match the sector mapping scheme developed by Harwerth et al. (Harwerth et al, 2007) and enable comparisons between pore geometry, RNFLT, visual field sensitivity, and mfERG signals from comparable regions. Pore parameters were compared in temporal sectors numbered 1, 2, 9, and 10 at baseline and all subsequent time-points during the progression of experimental glaucoma.

### *5.2.2 Functional tests: Multifocal electroretinography (mfERG) and standard automated perimetry (SAP)*

Functional measures of vision (mfERG and SAP) were recorded in parallel with SDOCT and AOSLO structural imaging in all 3 monkeys. mfERGs were first recorded approximately 100 days after the initial laser session and approximately every 2-3 weeks thereafter by Lakshmi Rajagopalan and Dr. Laura Frishman using the Visual Evoked Response Imaging System 4.1 (VERIS, Electro-Diagnostic Imaging, Inc., Redwood City, CA) (Rajagopalan et al, 2013). The mfERG stimulus array consisted of 19 unstretched black and white hexagons (each 7° in width) displayed on a CRT monitor with 75 Hz frame rate. The stimulus pattern subtended 35° x 34° on the retina and was positioned 46 cm from the monkey eye. Each of the 19 hexagons was flashed during the stimulus presentation based on a pseudo-random m-sequence of contrast-reversals in which the first 5 of 30 frames were bright (luminance of focal flash: 3.3 cd-s/$m^2$) and the last 25 frames were dark (luminance of dark frames: 0.18 cd-s/$m^2$). The duration of the 30 frames lasted 400 ms and the stimulus was repeated consecutively for 7 minutes. Responses to the stimulus were sampled at 1200 Hz and low pass filtered between 1

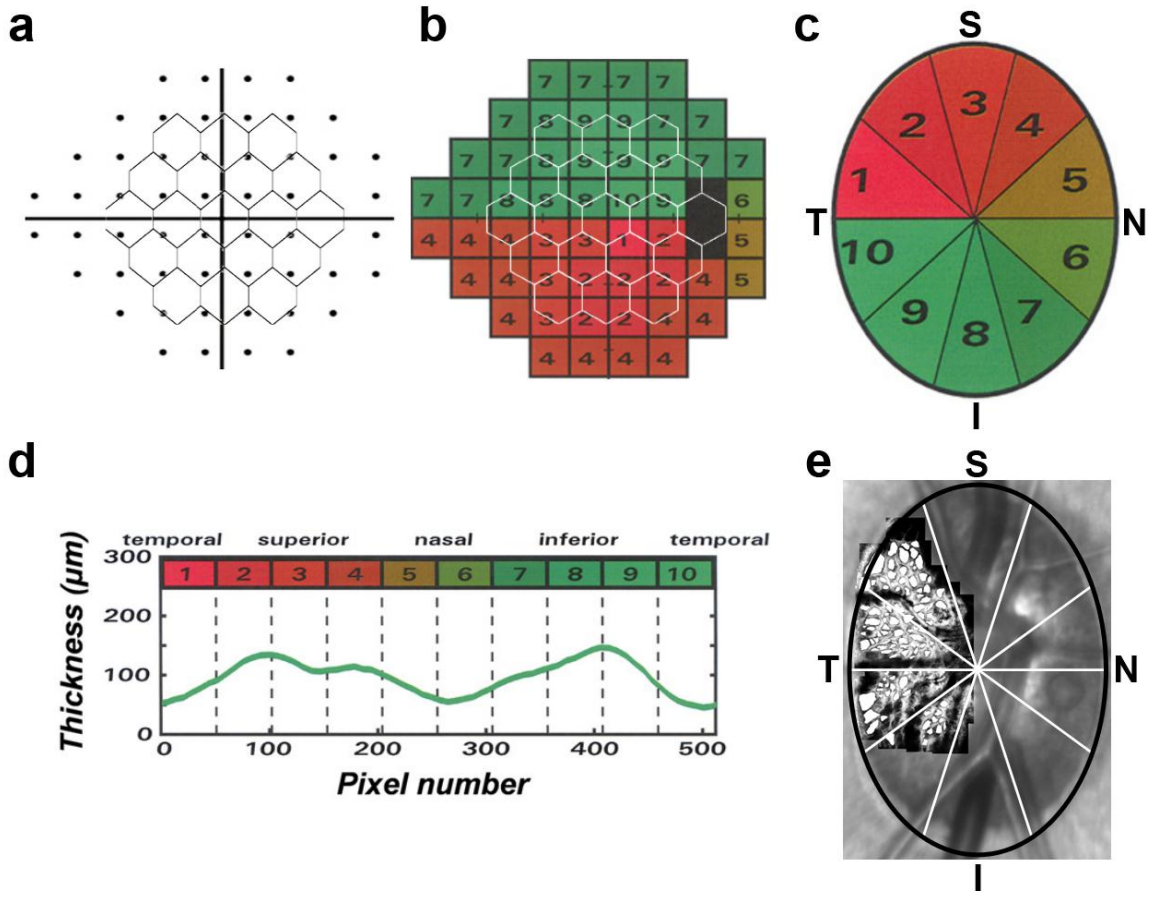


**Figure 5-1.** (a) Map of mfERG stimulus consisting of 19 hexagons overlaid and registered on SAP visual field testing locations (black dots). (b) The same mfERG stimulus (white hexagons) as shown in (a) overlaid on visual field testing locations. Testing locations are numbered and color coded corresponding to (c) the sector location that their axons are believed to project to in the ONH and (d) the spatial location the axons contribute to in RNFLT measurements using SDOCT (Harwerth et al, 2007). Square testing locations that are black in (b) coincide with the location of the optic disc. (e) AOSLO montage of anterior lamina cribrosa surface (pores marked in white) in which the area within the BMO ellipse (black line) has been correspondingly divided in ten, 36° sectors (white lines) to match the sectors in the ONH (c) and SDOCT-defined RNFLT maps (d).

and 300 Hz to remove oscillations. A Hanning window was applied offline to remove high frequency components above 55 Hz from the signal. Three 7-minute mfERG recordings were averaged. The mfPhNR, a signal that originates from RGCs in primates, was measured as the amplitude of the trough that immediately followed the b-wave (Fig. 5-2).

Visual field sensitivity was measured over the central 54° x 48° using a 24-2 full threshold test (Humphrey Field Analyzer model 630; Carl Zeiss Meditec, Dublin, CA) with a 0.43°-diameter Goldmann size III target. (Visual field tests were administered by Drs. Nimesh Patel and Ronald Harwerth to monkeys OHT-64 and OHT-66 approximately three to four times per week.) The testing areas for SAP and mfERG were not congruent (Fig. 5-1a). Therefore, a bilinear interpolation was used to align the SAP and mfERG testing areas (Hood & Zhang, 2000; Luo et al, 2011). In order to represent the mfERG contribution at each visual field location, the mfERG signal was divided among all visual field locations that it overlapped. For example, in Fig. 5-1b, the center hexagon overlapped visual field regions 1, 3, 8, and 10 equally. Consequently, 25% of the mfERG signal from the center hexagon contributed to each of the 4 visual field regions. mfERG signal contributions were proportionally divided among each overlapping visual field location and summed across the 10 individual regions. The same 10 visual field regions and 10 ONH sectors (Fig. 5-1b,c) were mapped to the aforementioned 12° RNFLT SDOCT circular scans (Fig. 5-1d) (Harwerth et al, 2007).

### *5.2.3 Statistical analysis*

A 95% confidence interval was constructed for each pore parameter (area, elongation, and NND) in sectors 1, 2, 9, and 10 for the baseline time-point and subsequent time-points that showed no statistically significant change (as determined by a Mann-Whitney rank sum test, $P>.05$) in EG eyes. The first time-point of significant change in pore

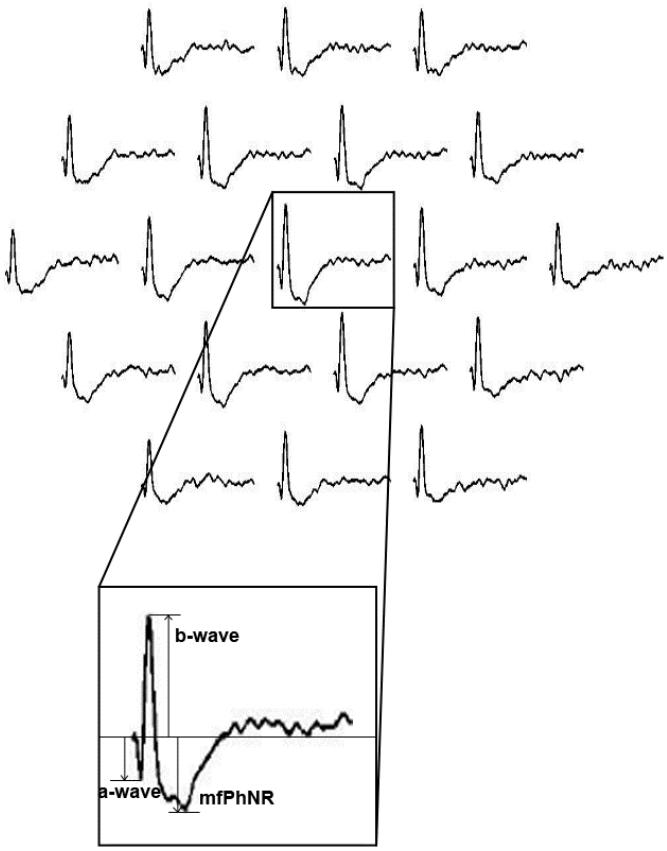


**Figure 5-2.** Array of typical mfERG responses in each of 19 hexagons from a normal monkey eye. Inset shows a magnified waveform of a mfERG response from the center hexagon. The mfPhNR is calculated as the amplitude of the trough immediately following the b-wave.

parameters was determined to be the first time-point that fell outside the aforementioned 95% confidence interval. Similarly, 95% confidence intervals were constructed for mfPhNR amplitude and RNFLT in sectors 1, 2, 9, and 10 from control eyes at all measured time-points. The first time-point in the EG eye that fell outside of the 95% confidence interval denoted the first significant change in either mfPhNR amplitude or sectoral RNFLT. 95% confidence intervals were also constructed for mean ALCSD, mean MRW, and visual field sensitivity from control eyes in each monkey. The first significant change in both parameters was assessed in each EG eye as the first time-point that fell outside the 95% confidence interval with no subsequent time-points having values that fell back within the confidence interval. Time-points of the first significant change in global or sectoral pore geometry, sectoral RNFLT, sectoral mfPhNR amplitude, mean ALCSD, and mean MRW were compared. Linear regression was used to correlate reductions in mfPhNR amplitude vs. reductions in sectoral RNFLT and losses in visual field sensitivity for all monkeys.

### 5.3 Results

ONH parameters (mean ALCSD and mean MRW) and RNFLT significantly changed longitudinally in all EG eyes (Table 5-1). On average across EG eyes, the first significant change in mean ALCSD, mean MRW, and RNFLT represented a +33%, -20%, and -8% change from baseline, respectively.

Values of ALCS pore geometry at the first significant time-points of change are shown in Table 5-2 on global and sector scales for all 3 monkeys relative to baseline and earlier time-points with no statistically significant change. Images of ALCS pore geometry at baseline and the first time-point of change are shown in Fig. 5-3 for all 3 EG eyes in the temporal sectors. At the first time of change in ALCS pore geometry, global pore area, elongation, and NND significantly increased in 2 of 3 EG eyes (OHT-64 and

**Table 5-1.** Mean ALCSD, mean MRW, and RNFLT at baseline and the first time-point of statistically significant change for EG eyes of monkeys OHT-64, OHT-66, and OHT-69.

| | Mean ALCSD (μm) | | Mean MRW (μm) | | RNFLT (μm) | |
|---|---|---|---|---|---|---|
| | **Baseline** | **First change** | **Baseline** | **First change** | **Baseline** | **First change** |
| **OHT-64** | 199.5 | 354.3 | 249.4 | 193.8 | 104 | 100 |
| **OHT-66** | 156.3 | 174.3 | 299.8 | 214.7 | 94 | 80 |
| **OHT-69** | 211.6 | 235.3 | 402.1 | 360.4 | 122 | 116 |

**Table 5-2.** Mean (± SD) pore parameters for EG eyes of OHT-64, OHT-66, and OHT-69 on global and sector scales at the first time-point of change (First change) relative to baseline and previous time-points of no statistically significant change (No change).

| | Area (μm²) | | Elongation | | NND (μm) | |
|---|---|---|---|---|---|---|
| | **No change** | **First change** | **No change** | **First change** | **No change** | **First change** |
| **OHT-64** | | | | | | |
| **Global** | 961.9±111.2 | 1192.4* | 1.65±0.10 | 1.80* | 40.6±3.1 | 52.3* |
| **2** | 1,213.2±106.9 | 1366.5 | 1.54±0.02 | 1.93* | 43.0±1.5 | 55.7* |
| **1** | 785.8±133.1 | 1423.8* | 1.77±0.13 | 1.90 | 37.2±4.0 | 51.4* |
| **10** | 915.9±342.9 | 720.9 | 1.65±0.11 | 1.48* | 43.5±4.0 | 56.7* |
| **9** | 821.1±189.9 | -- | 1.58±0.01 | -- | 39.5±1.3 | -- |
| **OHT-66** | | | | | | |
| **Global** | 746.8±61.0 | 1169.3* | 1.78±0.30 | 1.84* | 34.2±2.9 | 41.3* |
| **2** | 831.7±93.7 | 1660.0* | 1.59±0.33 | 1.59 | 36.2±3.4 | 44.6* |
| **1** | 710.1±128.1 | 994.2* | 1.92±0.37 | 1.82 | 33.6±2.5 | 39.3* |
| **10** | 677.7±36.1 | 1210.2* | 1.63±0.16 | 1.63 | 33.4±0.8 | 42.5* |
| **9†** | 829.7 | 1512.7 | 2.00 | 1.37 | 34.3 | 46.1 |
| **OHT-69** | | | | | | |
| **Global** | 832.7±230.3 | 1089.7* | 1.73±0.05 | 1.63* | 38.5±10.1 | 43.6 |
| **2** | -- | -- | -- | -- | -- | -- |
| **1** | 860.5±200.6 | 1062.5 | 1.75±0.10 | 1.64 | 39.8±6.0 | 42.0 |
| **10** | 917.5±221.3 | 1131.7 | 1.75±0.09 | 1.63 | 37.1±1.5 | 43.0* |
| **9** | -- | -- | -- | -- | -- | -- |

'*' pore parameter fell outside the 95% confidence interval constructed for the given pore parameter quantified from previous time-points of no change.

'--' no pores quantified in this sector.

'**' because pores quantified in this sector were from one time-point, a 95% confidence interval was not constructed and statistical significance was not determined at the time-point of first change.

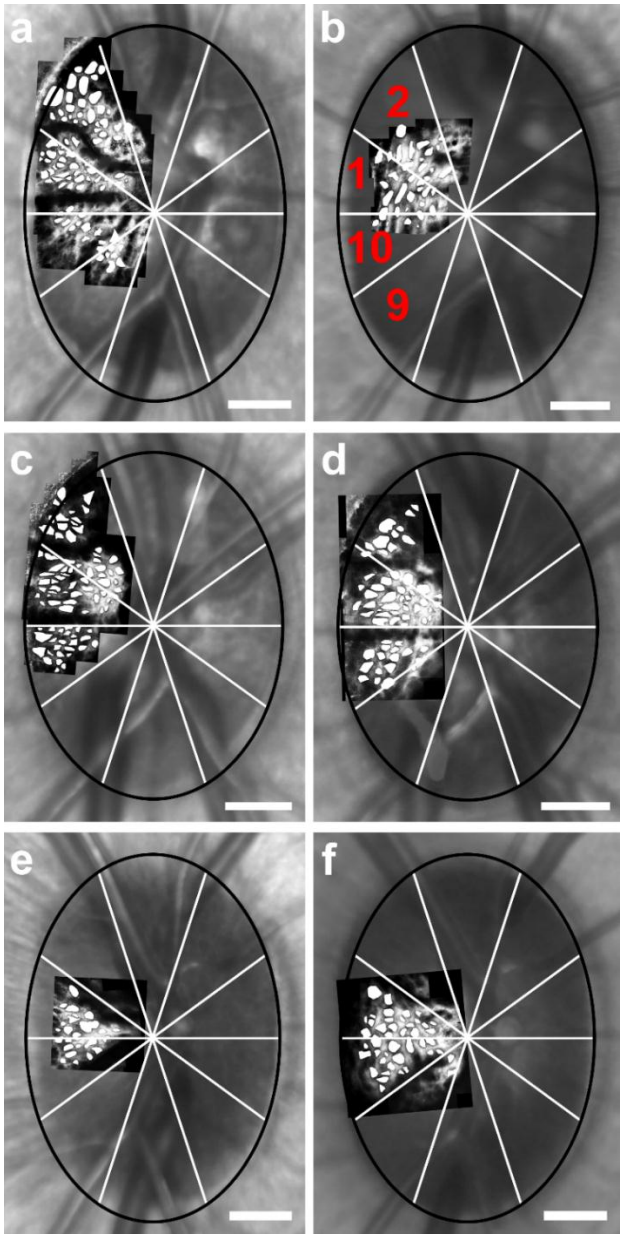


**Figure 5-3**. Images of ALCS microarchitecture acquired in all EG eyes at baseline (left column) and the first statistically significant change in laminar pore geometry (right column) in temporal sectors 1, 2, 9, and 10 of (a,b) OHT-64, (c,d) OHT-66 and (e,f) OHT-69. AOSLO montages of the ALCS were scaled, registered, and overlaid on the corresponding SLO images. After manually marking laminar pores (shown in white) in each montage, pores were examined globally and in 36° sectors (white meridians) within the BMO ellipse (black line). Significant changes in pore geometry were seen in sectors 1, 2, and 10. Scale bar: 300 μm.

OHT-66) while pore area significantly increased and pore elongation significantly decreased (i.e., more circularly-shaped pores) in the third EG eye (OHT-69). On a local level, there were statistically significant increases in ALCS pore area and NND within temporal sector 1 in 2 of 3 EG eyes (OHT-64 and OHT-66) that occurred simultaneously with the first changes measured in global ALCS pore geometry. Within superotemporal sector 2 and temporal sector 10, pore NND significantly increased at the first time-point of change in all EG eyes. Pore area showed a corresponding significant increase in sectors 2 and 10 at the first time-point of change in OHT-66 while pore elongation simultaneously increased in superotemporal sector 2 (i.e., more elliptically-shaped pores) and decreased in temporal sector 10 (i.e., more circularly-shaped pores) in OHT-64.

Figures 5-4 through 5-6 show the longitudinal change in mfPhNR amplitude within sectors 1, 2, 9, and 10 in each EG eye. The first time-point with a statistically significant change in local mfPhNR amplitude (blue triangle) was also plotted relative to the time points of the first statistically significant change measured in mean ALCSD (black triangle) and local ALCS pore geometry (red line) in each sector. A significant decrease in local mfPhNR amplitude occurred prior to the first significant (and simultaneous) change in mean ALCSD and local ALCS pore geometry in sectors 1 and 2 for monkey OHT-64 (Fig. 5-4). Conversely, a simultaneous change in mean ALCSD and local ALCS pore geometry occurred prior to the first significant change in local mfPhNR amplitude in temporal sector 10, while the first significant change in mean ALCSD also occurred prior to the first significant change in mfPhNR amplitude in inferotemporal sector 9. In monkeys OHT-66 (Fig. 5-5) and OHT-69 (Fig. 5-6), however, an increase in mean ALCSD always preceded the first measured change in local mfPhNR amplitude and local ALCS pore geometry. A change in mean ALCSD occurred prior to a simultaneous first change in local mfPhNR amplitude and local ALCS pore

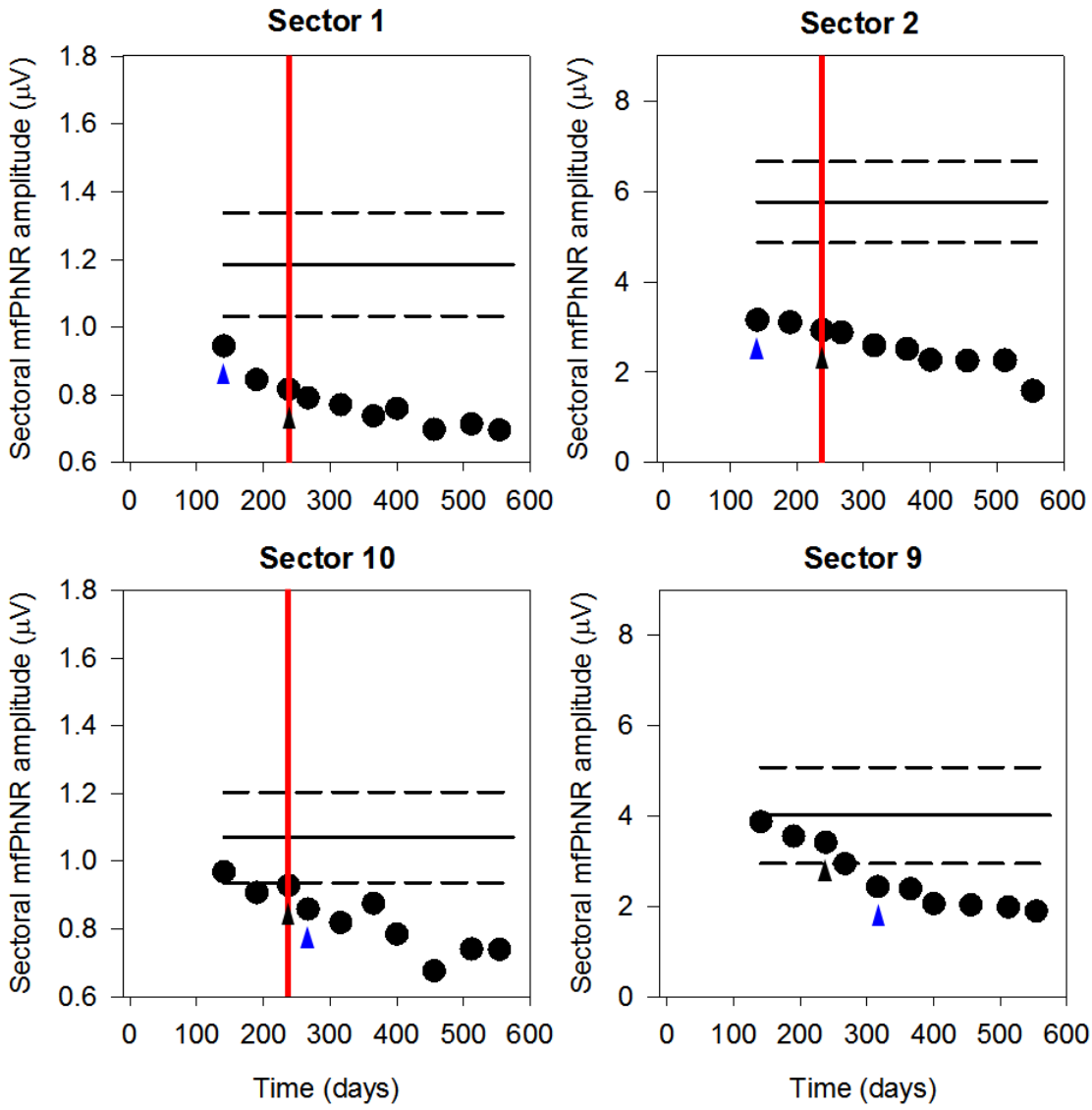


**Figure 5-4.** mfPhNR amplitudes (filled black circles) from 10 time-points in sectors 1, 2, 9, and 10 in the EG eye of monkey OHT-64. 95% confidence intervals were constructed from mfPhNR amplitudes measured in the fellow control eye. (Dashed black lines represent the upper and lower limits of the confidence interval about the mean value [solid black line]). Time-points representing the first statistically significant change in the amplitude of the mfPhNR relative to the control eye are indicated by blue triangles in each sector. Time-points representing the first statistically significant change in mean ALCSD are indicated by a black triangle. mfPhNR amplitudes were significantly reduced in the EG eye (blue triangles) compared to the control eye by the first time-point of mfERG recording in sectors 1 and 2. These time-points also preceded the first significant change in local ALCS pore geometry (red lines) and mean ALCSD (black

triangle). Pore geometry and mean ALCSD significantly changed prior to a significant reduction in mfPhNR amplitude in sector 10. There were no pore data in sector 9 at the first time-point of change (Fig. 5-3b). (Initial plots were created by Lakshmi Rajagopalan and subsequently modified by Kevin Ivers.)

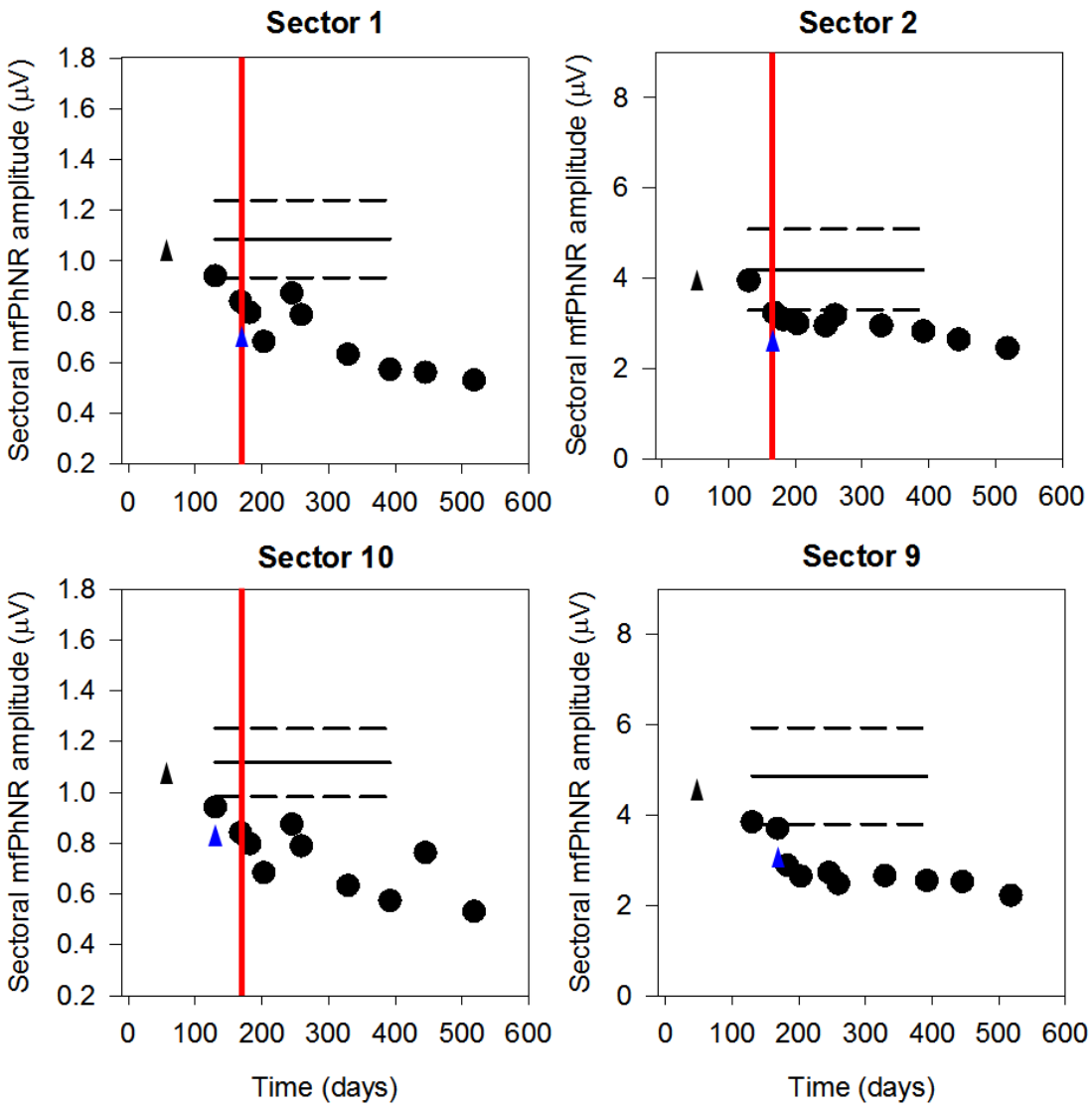


**Figure 5-5.** mfPhNR amplitudes (filled black circles) from 10 time-points in sectors 1, 2, 9, and 10 in the EG eye of monkey OHT-66. An increase in mean ALCSD (black triangle) always preceded the first measured change in local mfPhNR amplitude (blue triangle) and local ALCS pore geometry (red line). The first significant change in pore geometry (red line) and the first significant reduction in the mfPhNR amplitude (blue triangle) occurred simultaneously in sectors 1 and 2. The mfPhNR amplitude was significantly reduced compared to the control eye by the first time-point of mfERG recording in sector 10 and occurred one imaging session prior to the first significant change in pore geometry. There were no pore data in sector 9 at baseline (Fig. 5-3c). (Initial plots were created by Lakshmi Rajagopalan and subsequently modified by Kevin Ivers.)

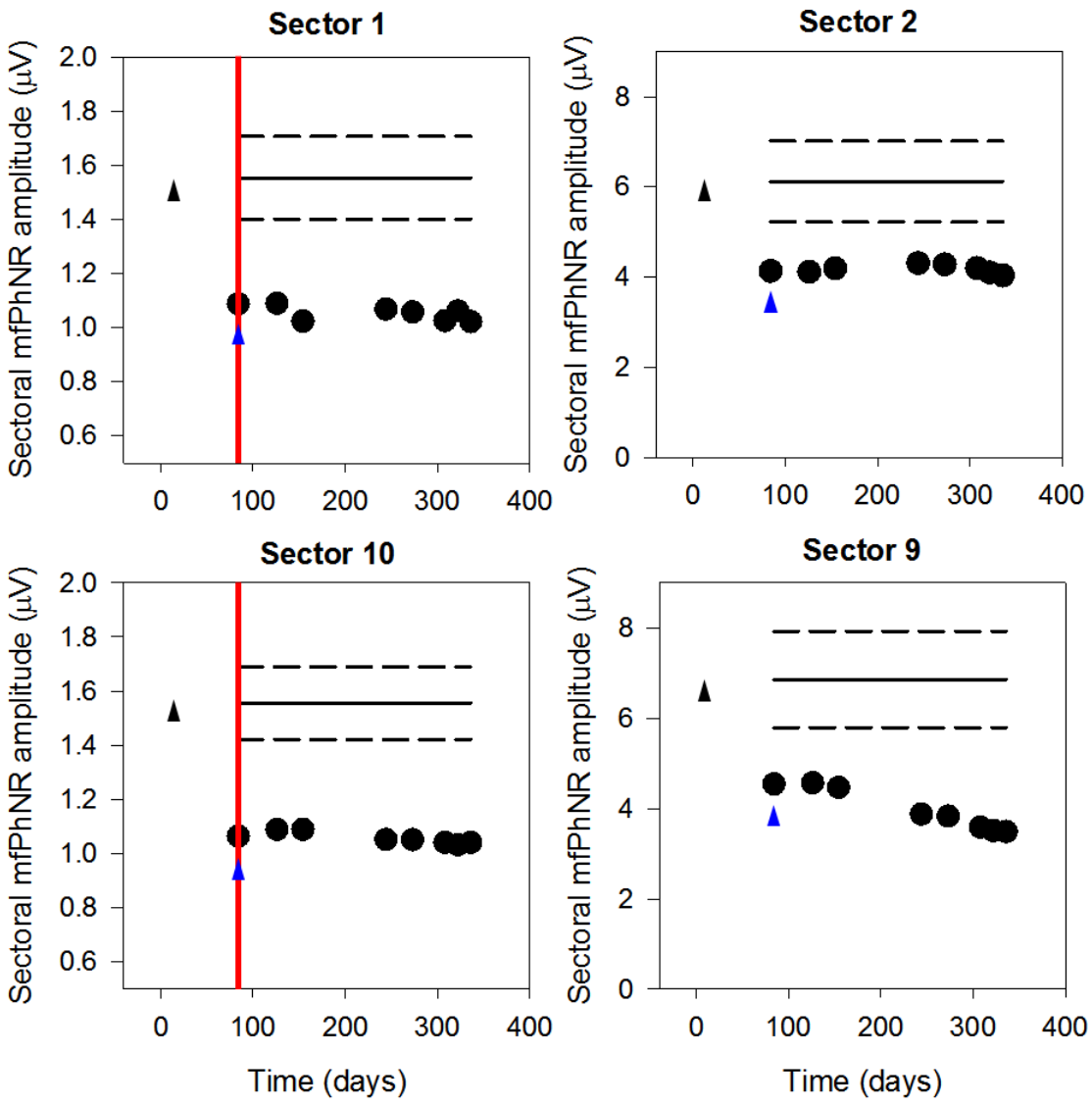


**Figure 5-6.** mfPhNR amplitudes (filled black circles) from 8 time-points in sectors 1, 2, 9, and 10 in the EG eye of monkey OHT-69. An increase in mean ALCSD (black triangle) always preceded the first measured change in local mfPhNR amplitude (blue triangle) and local ALCS pore geometry (red line). The first time-point of significant change in pore geometry (red line) coincided with the first time-point of significant mfPhNR amplitude reduction (blue triangle) in sectors 1 and 10. Pore data were not present in sectors 2 and 9 at all time-points of imaging (Fig. 5-3e,f). (Initial plots were created by Lakshmi Rajagopalan and subsequently modified by Kevin Ivers.)

geometry in sectors 1 and 2 of OHT-66 and in temporal sectors 1 and 10 of OHT-69, while a local change in mfPhNR amplitude occurred one imaging session prior to the first local change in ALCS pore geometry in sector 10 of OHT-66.

The longitudinal changes in visual field sensitivity measured in EG eyes of monkeys OHT-64 and OHT-66 are shown in Fig. 5-7. The first time-point of change in which visual field sensitivity (assessed as the mean deviation) exceeded the 95% confidence interval calculated from fellow control eye data (blue triangles) occurred after the first significant changes in pore geometry for both EG eyes. For monkey OHT-64, the mean deviation in visual field sensitivity at the time of first significant change was -3.95 dB at 511 days post-laser treatment, whereas the first significant change in ALCS pore geometry occurred 233 days after the initial laser procedure. For monkey OHT-66, the mean deviation in visual field sensitivity at the time of first significant change was -2.28 dB at 244 days post-laser treatment, whereas ALCS pore geometry first changed at 168 days after the initial laser procedure.

Linear regression analyses were performed by Dr. Frishman's laboratory to assess the correlation of the local mfPhNR amplitude with sectoral RNFLT and local visual field sensitivity. Reductions in local mfPhNR amplitudes were strongly correlated with decreases in sectoral RNFLT across all monkeys. The Pearson correlation coefficient was 0.78 ($P<.0001$) in EG eyes and 0.86 ($P<.0001$) in control eyes. Reductions in local mfPhNR amplitudes were moderately (but statistically significantly) correlated with losses in visual field sensitivity across all monkeys. The Pearson correlation coefficient was 0.41 ($P<.0001$) in EG eyes and 0.42 ($P<.0001$) in control eyes.

Finally, Table 5-3 summarizes the time-course of the first statistically significant changes measured in all structural and functional parameters in our 3 EG eyes. Mean ALCSD was the first structural or functional parameter to have a statistically significant

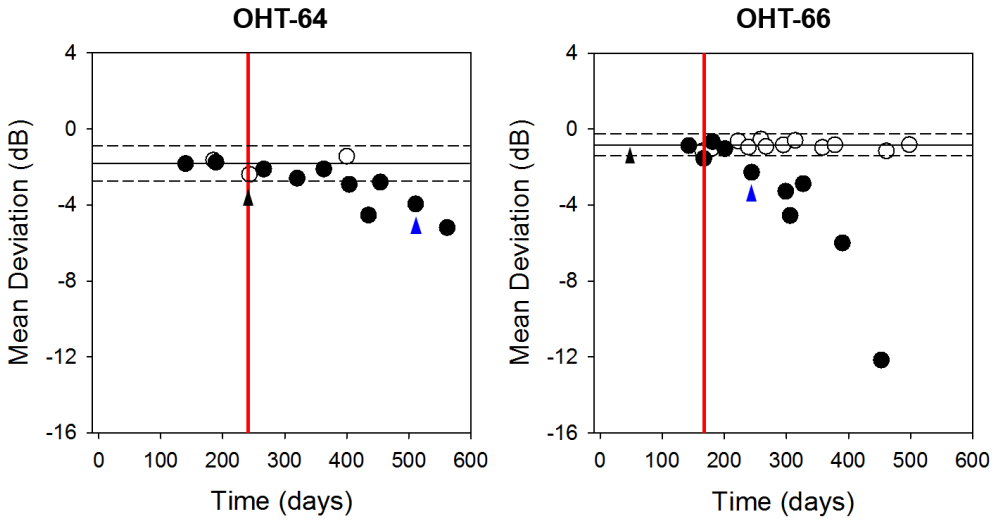


**Figure 5-7.** Change in mean deviation in visual sensitivity plotted longitudinally as a function of time for control eyes (open circles) and EG eyes (filled circles) in monkeys OHT-64 and OHT-66. 95% confidence intervals were constructed from mean deviation values measured in the fellow control eye. (Dashed black lines represent the upper and lower limits of the confidence interval about the mean value [solid black line]). The first time-point of significant loss in visual field sensitivity (blue triangle) occurred after the first time-point of significant change in pore geometry (red line) for both monkeys.

**Table 5-3.** Number of days after the first laser treatment in which a significant change was first measured in ALCS pore geometry, mfPhNR amplitude, and RNFLT in any sector (1, 2, 9, or 10), as well as the first time-points of change in mean ALCSD, mean MRW, and visual field sensitivity in all EG eyes.

| Animal ID | Sectoral mfPhNR Amplitude | Sectoral Pore Geometry | Sectoral RNFLT | Mean ALCSD | Mean MRW | Visual Field Sensitivity |
|---|---|---|---|---|---|---|
| OHT-64 | 141 (1,2) | 238 (1,2,10) | 267 (2) | 238 | 238 | 511 |
| OHT-66 | 130 (10) | 168 (1,2,10) | 182 (1,2) | 49 | 168 | 244 |
| OHT-69 | 84 (1,2,9,10) | 84 (10) | 84 (2,9) | 18 | 18 | -- |

* Values in parentheses indicate sectors that demonstrated statistically significant changes in the given parameter.

change in 2 of 3 EG eyes (OHT-66 and OHT-69), while a reduction in the mfPhNR amplitude was measured first in the third EG eye (OHT-64). Mean MRW also significantly decreased concurrently with the first significantly measured change in mean ALCSD in OHT-69, and was the second and third parameter to change in OHT-64 and OHT-66, respectively. Local ALCS pore geometry was the second parameter to change in 2 eyes (OHT-64 and OHT-69) and the third parameter to change in OHT-66, while local RNFLT was the second-to-last parameter to change in all EG eyes. Visual field sensitivity was the final parameter to significantly change relative to baseline in early EG eyes.

### 5.4 Discussion

In this study, we provide an initial characterization of the time-course of structural changes (i.e., local ALCS pore microarchitecture, mean ALCSD, mean MRW, and local RNFLT) and functional changes (i.e., local mfPhNR amplitude and visual field sensitivity) in early experimental glaucoma. Our study is the first to compare structural changes in local laminar pore geometry and ONH geometry with functional measures of vision loss as assessed with the mfERG and SAP in experimental glaucoma.

The first statistically significant change in ALCS pore geometry on a sector level occurred at the same time as the first significant change in global ALCS pore geometry in all EG eyes (Table 5-2). However, the first time-points of significant change in a posterior deformation of the laminar surface (or mean ALCSD) and ALCS pore geometry occurred simultaneously in only one of three EG eyes (OHT-64, Table 5-3). A few reasons could potentially account for the fact that an increase in mean ALCSD occurred prior to the first significant change in ALCS pore geometry in two of three EG eyes (OHT-66 and OHT-69). First, overlying vasculature and the neuroretinal rim cast shadows onto the ALCS microarchitecture and mask our ability to image the most

superior, inferior, and peripheral portions of the laminar surface. Therefore, it is possible that changes in the laminar microarchitecture could occur earlier in these regions than we are capable of imaging with our AOSLO. Second, depending on the stiffness of a given lamina, it is possible for the ALCS to uniformly move posteriorly without significant amounts of bowing (Sredar et al, 2013). In such a scenario, ALCS beams and pores may not undergo substantial modification at this initial time of change in ALCSD. Third, it is possible that small, non-statistically significant amounts of laminar remodeling may take place on the anterior surface while larger modifications in laminar microarchitecture take place in more posterior layers that are not imaged with our AOSLO. Improved visualization of the posterior laminar microarchitecture could be achieved using swept source or adaptive optics OCT (Nadler et al, 2013; Wang et al, 2013) and used to better understand early, longitudinal changes in laminar microarchitecture throughout a region of increased laminar depth.

Consistent with a hypothesis that structural alterations in the lamina cribrosa result in axonal degeneration and retinal ganglion cell death in glaucoma, we found that significant changes in global and local ALCS pore geometry occurred prior to the first significant change in local RNFLT in 2 of 3 EG eyes (OHT-64 and OHT-66) (Table 5-3). Moreover, some ONH sectors that showed a significant local change in ALCS pore geometry also showed a decrease in local RNFLT at a subsequent time point. For example, the first time-point of significant change in local ALCS pore geometry in OHT-64 occurred 238 days following the initial laser treatment in ONH sectors 1, 2, and 10 (Table 5-3). Twenty-nine days later, RNFLT showed its first corresponding change that also occurred in sector 2. Similarly, the first time-point of significant change in local ALCS pore geometry in OHT-66 occurred 168 days following the initial laser treatment in ONH sectors 1, 2, and 10 (Table 5-3). Fourteen days later, RNFLT showed its first corresponding change that also occurred in sectors 1 and 2. And, while the first time-

point of change in ALCS pore geometry occurred concurrently with the first change in RNFLT in one EG eye (OHT-69) (Table 5-3), we were not able to image and quantify ALCS pores in the ONH sectors that showed the first significant change in RNFLT, namely sectors 2 and 9 (Fig. 5-3f). Therefore, it is unknown whether ALCS pores significantly changed prior to an initial RNFLT change in these regions.

When examining functional changes in vision in experimental glaucoma, the first time-point of significant change in the mfPhNR amplitude occurred well before the first time-point of significant change in visual field sensitivity (Table 5-3). The mfPhNR amplitude was one of the first or second structural or functional parameters to show a significant change in all EG eyes. However, visual field sensitivity was the last analyzed parameter to significantly change in early stages of experimental glaucoma in both monkeys that performed SAP (OHT-64 and OHT-66). These preliminary results support the idea that mfERG measures may be more sensitive than perimetry in early detection of functional changes. Specifically, the PhNR of the light-adapted full-field flash ERG is known to originate from ganglion cells in primates and has been shown to be significantly reduced in early experimental glaucoma when perimetry-based visual field losses are mild or marginal, perhaps due to early changes in astrocyte function in the ONH (Viswanathan et al, 1999). The use of the mfERG stimulus to improve regional objective evaluation of glaucomatous damage through measurement of the mfPhNR amplitude could serve as a useful tool for detecting functional changes in early glaucoma.

One potential limitation of the functional measurements is that mfERG data were not recorded in control or EG eyes until approximately 100 days after the initial laser treatment used to induce experimental glaucoma. Because baseline mfERG data were not collected, determination of the first time-point that had a statistically significant reduction in the mfPhNR amplitude could only be made by comparing mfERG

waveforms from EG eyes with those from fellow control eyes. An implicit assumption in this type of analysis is that the mfPhNR amplitude was similar (or within the normal variability of the measurement) between fellow eyes of the same monkey prior to induction of experimental glaucoma. While no published studies have reported inter-eye differences in the mfPhNR amplitude in normal eyes, previous studies have examined inter-eye differences in the full-field PhNR amplitude in rhesus monkeys. Fortune et al. measured the coefficient of variation (COV) in PhNR amplitude between fellow eyes in 29 normal monkeys to vary between 9.0% and 13.4% depending on the intensity of the photopic ERG stimulus (Fortune et al, 2004). Viswanathan et al. also measured the difference in PhNR amplitude between left and right eyes of 7 monkeys before inducing unilateral experimental glaucoma and found baseline PhNR amplitudes to be within approximately ±30% of PhNR amplitudes in fellow control eyes (Viswanathan et al, 1999). Based on these previous results, it may be likely that there is low variability in mfPhNR amplitude between fellow eyes. In addition, a consequence of not recording mfERG data until ~100 post-initial laser treatment is that it is unknown whether changes in the mfPhNR amplitude occurred earlier than the initial recording time-point, particularly given that a statistically significant change in the mfPhNR was measured in at least 1 sector in all EG eyes (relative to control eye data) at the initial mfERG recording time-point.

In our longitudinal analysis of the first time-point of significant change in structural and functional parameters, we found that the first parameter to change in early experimental glaucoma was mean ALCSD (two of three EG eyes) or mfPhNR amplitude (one of three EG eyes). Conversely, RNFLT and visual field sensitivity, two of the primary measurements used to clinically detect the onset of glaucomatous damage, were the last structural or functional parameters to have a statistically significant change in early experimental glaucoma. These results support the notion that changes in the

lamina cribrosa result in subsequent changes in axonal function and structure in glaucoma, and are consistent with previous studies that reported an increase in mean ALCSD prior to a decrease in RNFLT (Strouthidis et al, 2011b) or a change in mfERG signals (He et al, 2014) in experimental glaucoma. In addition, the fact that we found a statistically significant change in the mfPhNR amplitude to occur prior to the first significant loss in RNFLT (in all EG eyes) and the first significant reduction in mean MRW (in 2 of 3 EG eyes) potentially indicates that it is possible to measure a functional change in axonal integrity prior to measuring a structural loss in RNFL axons. This observation is also in agreement with Fortune et al. who found a significant reduction in the mfERG signal prior to a reduction in RNFLT in monkeys with experimental glaucoma (Fortune et al, 2012).

In conclusion, we have measured changes in anterior laminar surface position (mean ALCSD), laminar pore microarchitecture, and mfPhNR amplitude prior to the first time-point of significant loss in RNFLT and visual field sensitivity in a non-human primate model of experimental glaucoma. The fact that mean ALCSD was the first structural or functional parameter to change in 2 of 3 EG eyes lends support to the idea that RGC axons are initially damaged at the level of the lamina cribrosa in early experimental glaucoma. An increased number of EG eyes will need to be examined to elaborate on these initial findings. Finally, AOSLO and SDOCT imaging and mfERG recording offer the potential to prevent vision loss via earlier detection of glaucomatous damage. These sensitive *in vivo* imaging techniques could also provide improved evaluation and tracking of therapeutic treatments as they are developed.

### 5.5 Acknowledgements

Research supported by NIH grants K23 EY021761 (Patel), R01 EY01139 (Harwerth), P30 EY07551 (Frishman), and R01 EY021783 (Porter).

# CHAPTER 6

## General Conclusions

## 6.1 General Conclusions

The lamina cribrosa likely plays an important role in the onset and progression of glaucoma (Bellezza et al, 2003; Burgoyne et al, 2004; Gaasterland et al, 1978; Minckler et al, 1977; Quigley et al, 1981; Quigley & Green, 1979). The mechanisms responsible for retinal ganglion cell (RGC) axon degeneration and RGC death are controversial and not well understood. However, several published studies (and the work described in this dissertation) further implicate the lamina cribrosa as the site of initial injury to RGC axons in glaucoma. The experiments carried out in this work were designed to contribute to a more detailed understanding of the structural properties of the physiologically normal anterior lamina cribrosa and ONH in humans and non-human primates (Chapters 2 and 3) and how these structures change in a non-human primate model of experimental glaucoma (Chapter 4). The last experiment presented in Chapter 5 provides a broader understanding of the time course of structural changes measured in the ONH and lamina cribrosa compared to functional measures of vision loss.

### *6.1.1 Experiment 1 (Chapter 2):* Quantify reproducibility of measuring lamina cribrosa pore geometry *in vivo* in normal human and non-human primates using an AOSLO.

Anterior lamina cribrosa surface microarchitecture can be quantified *in vivo* with high repeatability in normal human and non-human primate eyes using adaptive optics scanning laser ophthalmoscope (AOSLO) imaging. This study established imaging methodologies and strategies subsequently used to assess the feasibility in repeatedly and reliably imaging the same laminar structure in human and monkey eyes over time. ALCS pore geometry was found to be similar to previous studies, with pore areas ranging from 90 to 4,365 $\mu m^2$ in monkeys and 154 to 6,637 $\mu m^2$ in humans. Small variability was found in measuring laminar pore area (6.1%, 8.3%), elongation (6.7 %,

7.7%), and nearest neighbor distance (NND) (5.2%, 4.1%) in normal monkey and human eyes, respectively, over time (*P*>.05). Results from this experiment suggest the same laminar structures can be consistently imaged over long periods of time in normal human and monkey eyes, and were a necessary and important first step in establishing the viability for using the same techniques to examine a changing laminar structure in animal models of experimental glaucoma.

### *6.1.2 Experiment 2 (Chapter 3):* Characterize inter-eye differences in lamina cribrosa and ONH structure *in vivo* in normal non-human primates.

Inter-eye differences in ONH structure and anterior lamina cribrosa surface microarchitecture were found to be small in normal eyes of non-human primates. An increasing number of studies have reported cross-sectional differences in ONH and ALCS structural parameters between normal and glaucomatous human eyes and between fellow control and EG eyes in animal models. Given that these studies implicitly assume that the parameters being examined are similar between fellow eyes of the same subject and that knowledge of the natural variability in ONH and laminar structure between normal fellow eyes is limited, it is important to better understand the natural variability inherent in ONH and laminar parameters between fellow eyes, particularly when examining early changes in glaucoma. To this end, we characterized inter-eye differences in ONH parameters and ALCS microarchitecture in normal monkey eyes. Inter-eye differences in ONH parameters (including Bruch's Membrane Opening [BMO] area, mean ALCSD, and mean MRW) were small (*P*>.05). Similarly, inter-eye differences in anterior laminar surface pore geometry were small on global, regional, and sector levels (*P*>.05). However, regional differences in mean ALCS pore area and NND existed between fellow normal eyes in the superotemporal and temporal sectors of the ONH (*P*<.05). By examining inter-eye differences in normal ONH and laminar pore

parameters on global and local levels, we gained a more thorough understanding of the normal variability present in these structures between fellow eyes. Moreover, this variability data was useful in establishing bounds for differences expected in these structures between fellow eyes when trying to characterize subtle changes to ONH and laminar structure that occur at the earliest stages of unilateral experimental glaucoma.

### *6.1.3 Experiment 3 (Chapter 4):* Determine whether changes in anterior lamina cribrosa pore microarchitecture and ONH structure precede changes in retinal nerve fiber layer thickness *in vivo* in non-human primates with experimental glaucoma.

Early structural changes in the ONH and lamina cribrosa occurred prior to a significant loss in retinal nerve fiber layer thickness (RNFLT). It is estimated that 10 to 15% of RGCs are already lost by the first time-point of detectable RNFLT loss in eyes with glaucoma (Cull et al, 2012). Spectral domain optical coherence tomography (SDOCT) and AOSLO imaging were used to detect early changes in ONH structure and anterior laminar pore microarchitecture at time-points that preceded the time of first significant change in RNFLT in nearly all EG eyes. The earliest time-points of change in pore geometry were marked by significant global and local increases in mean pore area and NND. Laminar beams and pores appeared to “remodel” in a circumferentially oriented pattern concentric with the ONH in later stages of disease. Furthermore, the first significant structural changes in mean ALCSD occurred before or simultaneous with the first measured significant change in ALCS pore microarchitecture in all EG eyes. The variability measured in ALCS pore geometry across animals is likely influenced by the underlying biomechanical tissue properties of each lamina cribrosa. As a result, eye-specific laminar tissue properties might be responsible for the varying degree of axonal damage due to chronic elevations in intraocular pressure (IOP). The fact that structural

changes in ONH parameters (e.g., mean ALCSD and mean MRW) and ALCS pore geometry occur prior to a change in RNFLT, a common parameter used in the assessment of the onset and progression of glaucoma, could have implications for how glaucoma is diagnosed clinically in the future.

### *6.1.4 Experiment 4 (Chapter 5):* Determine whether structural changes in the ONH and lamina cribrosa microarchitecture observed *in vivo* in experimental glaucoma in non-human primates precede changes in visual function.

Significant increases in anterior laminar surface position (mean ALCSD), anterior laminar surface microarchitecture, and mfPhNR amplitude were measured prior to the first significant losses in RNFLT and visual field sensitivity in early EG eyes. To better characterize the onset and time-course of structural and functional changes in early experimental glaucoma (EG), we longitudinally measured ONH and ALCS pore parameters (using aforementioned techniques) as well as functional changes in vision measured using the mfERG (to assess local reductions in mfPhNR amplitude) and standard automated perimetry (to assess visual sensitivity) on global and local levels during the progression of experimental glaucoma in monkey eyes. In each EG eye, the first significant change in sectoral RNFLT and visual sensitivity occurred following the first measured structural changes in ONH parameters, ALCS pore geometry, and functional losses in mfPhNR amplitude. Similar to the results from Experiment 3 (Chapter 4), these findings suggest that AOSLO and SDOCT structural imaging of the lamina cribrosa and ONH and mfERG functional imaging of inner retinal activity can detect glaucomatous changes earlier than current clinical tools used to assess the onset of glaucoma (i.e., decreases in RNFLT and visual sensitivity).

### 6.2 Summary and future directions

*In vivo* high-resolution structural imaging of the lamina cribrosa in non-human primates can provide a deeper understanding of the early structural changes occurring in glaucoma. However, parallel structural examinations of the ONH and functional examinations of inner retinal activity and visual sensitivity are equally important to fully realize the time-course of events that shape the onset and progression of glaucoma. Future studies which examine lamina cribrosa pore geometry and connective tissue structure *ex vivo* via histology for comparison with our *in vivo* results and for examining changes that potentially occur at deeper levels of the lamina than we have currently imaged in the aforementioned experiments will further enhance the characterization of biomechanical changes that occur at different stages of glaucoma. Studies that measure laminar beam and pore microarchitecture on a more automated (i.e., more objective) level will be necessary to achieve these objectives on a more rapid time-scale. Results from these studies could yield a better understanding of the disease mechanisms responsible for the onset and progression of glaucoma and allow for earlier diagnosis and treatment strategies in patients worldwide.

# REFERENCES

Akagi T, Hangai M, Takayama K, et al. (2012). In vivo imaging of lamina cribrosa pores by adaptive optics scanning laser ophthalmoscopy. *Invest Ophthalmol Vis Sci* 53(7): 4111-4119.

Anderson DR (1969). Ultrastructure of human and monkey lamina cribrosa and optic nerve head. *Arch Ophthalmol* 82(6): 800-814.

Anderson DR, Hendrickson A (1974). Effect of intraocular pressure on rapid axoplasmic transport in monkey optic nerve. *Invest Ophthalmol* 13(10): 771-783.

Anderson DR, Hendrickson AE (1977). Failure of increased intracranial pressure to affect rapid axonal transport at the optic nerve head. *Invest Ophthalmol Vis Sci* 16(5): 423-426.

ANSI (2000). American National Standard for safe use of lasers (ANSI 136.1). *The Laser Institute of America ANSI* 136.1-2000.

Anton A, Moreno-Montanes J, Blazquez F, et al. (2007). Usefulness of optical coherence tomography parameters of the optic disc and the retinal nerve fiber layer to differentiate glaucomatous, ocular hypertensive, and normal eyes. *J Glaucoma* 16(1): 1-8.

Aulhorn E (1978). Visual field defects in chronic glaucoma. *In: Heilmann K, Richardson KT editor. Glaucoma. Conceptions of a Disease. Pathogenesis, Diagnoses, Therapy*: 157-168.

Balazsi AG, Rootman J, Drance SM, Schulzer M, Douglas GR (1984). The effect of age on the nerve fiber population of the human optic nerve. *Am J Ophthalmol* 97(6): 760-766.

Bellezza AJ, Hart RT, Burgoyne CF (2000). The optic nerve head as a biomechanical structure: initial finite element modeling. *Invest Ophthalmol Vis Sci* 2000(41): 2991-3000.

Bellezza AJ, Rintalan CJ, Thompson HW, et al. (2003). Deformation of the lamina cribrosa and anterior scleral canal wall in early experimental glaucoma. *Invest Ophthalmol Vis Sci* 44(2): 623-637.

Bhandari A, Fontana L, Fitzke FW, et al. (1997). Quantitative analysis of the lamina cribrosa in vivo using a scanning laser ophthalmoscope. *Curr Eye Res* 16(1): 1-8.

Budenz DL, Michael A, Chang RT, McSoley J, Katz J (2005). Sensitivity and specificity of the Stratus OCT for perimetric glaucoma. *Ophthalmology* 112(1): 3-9.

Burgoyne CF, Downs JC, Bellezza AJ, et al. (2004). Three-dimensional reconstruction of normal and early glaucoma monkey optic nerve head connective tissues. *Invest Ophthalmol Vis Sci* 45(12): 4388-4399.

Burgoyne CF, Downs JC, Bellezza AJ, Suh JK, Hart RT (2005). The optic nerve head as a biomechanical structure: a new paradigm for understanding the role of IOP-related stress and strain in the pathophysiology of glaucomatous optic nerve head damage. *Prog Retin Eye Res* 24(1): 39-73.

Burgoyne CF, Downs JC (2008). Premise and prediction-how optic nerve head biomechanics underlies the susceptibility and clinical behavior of the aged optic nerve head. *J Glaucoma* 17(4): 318-328.

Cepurna WO, Kayton RJ, Johnson EC, et al. (2005). Age related optic nerve axonal loss in adult Brown Norway rats. *Exp Eye Res* 80(6): 877-884.

Chauhan BC, Burgoyne CF (2013). From clinical examination of the optic disc to clinical assessment of the optic nerve head: a paradigm change. *Am J Ophthalmol* 156(2): 218-227 e212.

Chauhan BC, O'Leary N, Almobarak FA, et al. (2013). Enhanced detection of open-angle glaucoma with an anatomically accurate optical coherence tomography-derived neuroretinal rim parameter. *Ophthalmology* 120(3): 535-543.

Cull GA, Reynaud J, Wang L, et al. (2012). Relationship between orbital optic nerve axon counts and retinal nerve fiber layer thickness measured by spectral domain optical coherence tomography. *Invest Ophthalmol Vis Sci* 53(12): 7766-7773.

Dandona L, Quigley HA, Brown AE, et al. (1990). Quantitative regional structure of the normal human lamina cribrosa. A racial comparison. *Arch Ophthalmol* 108(3): 393-398.

Danias J, Lee KC, Zamora MF, et al. (2003). Quantitative analysis of retinal ganglion cell (RGC) loss in aging DBA/2NNia glaucomatous mice: comparison with RGC loss in aging C57/BL6 mice. *Invest Ophthalmol Vis Sci* 44(12): 5151-5162.

Delori FC, Webb RH, Sliney DH (2007). Maximum permissible exposures for ocular safety (ANSI 2000), with emphasis on ophthalmic devices. *J Opt Soc Am A Opt Image Sci Vis* 24(5): 1250-1265.

Demsar J, Curk T, Erjavec A, et al. (2013). Orange: Data Mining Toolbox in Python. *Journal of Machine Learning Research* 14(Aug): 2349-2353.

Downs JC, Ensor ME, Bellezza AJ, et al. (2001). Posterior scleral thickness in perfusion-fixed normal and early-glaucoma monkey eyes. *Invest Ophthalmol Vis Sci* 42(13): 3202-3208.

Downs JC, Suh JK, Thomas KA, et al. (2005). Viscoelastic material properties of the peripapillary sclera in normal and early-glaucoma monkey eyes. *Invest Ophthalmol Vis Sci* 46(2): 540-546.

Downs JC, Yang H, Girkin C, et al. (2007). Three-dimensional histomorphometry of the normal and early glaucomatous monkey optic nerve head: neural canal and subarachnoid space architecture. *Invest Ophthalmol Vis Sci* 48(7): 3195-3208.

Downs JC, Roberts MD, Burgoyne CF (2008). Mechanical environment of the optic nerve head in glaucoma. *Optom Vis Sci* 85(6): 425-435.

Downs JC, Roberts MD, Sigal IA (2011). Glaucomatous cupping of the lamina cribrosa: a review of the evidence for active progressive remodeling as a mechanism. *Exp Eye Res* 93(2): 133-140.

Ederer F, Gaasterland DA, Dally LG, et al. (2004). The Advanced Glaucoma Intervention Study (AGIS): 13. Comparison of treatment outcomes within race: 10-year results. *Ophthalmology* 111(4): 651-664.

Emery JM, Landis D, Paton D, Boniuk M, Craig JM (1974). The lamina cribrosa in normal and glaucomatous human eyes. *Trans Am Acad Ophthalmol Otolaryngol* 78(2): OP290-297.

Farquhar M (1991). The glomerular basement membrane. A selective macromolecular filter. *Cell Biology of Extracellular Matrix*. E. Hay, Springer US: 365-418.

Fechtner RD, Weinreb RN (1994). Mechanisms of optic nerve damage in primary open angle glaucoma. *Surv Ophthalmol* 39(1): 23-42.

Filippopoulos T, Danias J, Chen B, Podos SM, Mittag TW (2006). Topographic and morphologic analyses of retinal ganglion cell loss in old DBA/2NNia mice. *Invest Ophthalmol Vis Sci* 47(5): 1968-1974.

Fontana L, Bhandari A, Fitzke FW, et al. (1998). In vivo morphometry of the lamina cribrosa and its relation to visual field loss in glaucoma. *Curr Eye Res* 17(4): 363-369.

Fortune B, Bui BV, Cull G, Wang L, Cioffi GA (2004). Inter-ocular and inter-session reliability of the electroretinogram photopic negative response (PhNR) in non-human primates. *Exp Eye Res* 78(1): 83-93.

Fortune B, Burgoyne CF, Cull GA, Reynaud J, Wang L (2012). Structural and functional abnormalities of retinal ganglion cells measured in vivo at the onset of optic nerve head surface change in experimental glaucoma. *Invest Ophthalmol Vis Sci* 53(7): 3939-3950.

Fortune B, Burgoyne CF, Cull G, Reynaud J, Wang L (2013). Onset and progression of peripapillary retinal nerve fiber layer (RNFL) retardance changes occur earlier than RNFL thickness changes in experimental glaucoma. *Invest Ophthalmol Vis Sci* 54(8): 5653-5661.

Fortune B, Reynaud J, Wang L, et al. (2013). Does optic nerve head surface topography change prior to loss of retinal nerve fiber layer thickness: a test of the site of injury hypothesis in experimental glaucoma. *PLoS ONE* 8(10): e77831.

Frishman LJ, Shen FF, Du L, et al. (1996). The scotopic electroretinogram of macaque after retinal ganglion cell loss from experimental glaucoma. *Invest Ophthalmol Vis Sci* 37(1): 125-141.

Fujiwara T, Imamura Y, Margolis R, Slakter JS, Spaide RF (2009). Enhanced depth imaging optical coherence tomography of the choroid in highly myopic eyes. *Am J Ophthalmol* 148(3): 445-450.

Furlanetto RL, Park SC, Damle UJ, et al. (2013). Posterior displacement of the lamina cribrosa in glaucoma: in vivo interindividual and intereye comparisons. *Invest Ophthalmol Vis Sci* 54(7): 4836-4842.

Gaasterland D, Kupfer C (1974). Experimental glaucoma in the rhesus monkey. *Invest Ophthalmol* 13(6): 455-457.

Gaasterland D, Tanishima T, Kuwabara T (1978). Axoplasmic flow during chronic experimental glaucoma. 1. Light and electron microscopic studies of the monkey optic nervehead during development of glaucomatous cupping. *Invest Ophthalmol Vis Sci* 17(9): 838-846.

Giangiacomo A, Coleman A (2009). The Epidemiology of Glaucoma. *Glaucoma*. F. Grehn and R. Stamper, Springer Berlin Heidelberg: 13-21.

Girard MJ, Strouthidis NG, Ethier CR, et al. (2011). Shadow removal and contrast enhancement in optical coherence tomography images of the human optic nerve head. *Invest Ophthalmol Vis Sci* 52(10): 7738-7748.

Harwerth RS, Smith EL, 3rd, DeSantis L (1993). Behavioral perimetry in monkeys. *Invest Ophthalmol Vis Sci* 34(1): 31-40.

Harwerth RS, Smith EL, 3rd, DeSantis L (1997). Experimental glaucoma: perimetric field defects and intraocular pressure. *J Glaucoma* 6(6): 390-401.

Harwerth RS, Carter-Dawson L, Shen F, et al. (1999). Ganglion cell losses underlying visual field defects from experimental glaucoma. *Invest Ophthalmol Vis Sci* 40(10): 2242-2250.

Harwerth RS, Crawford ML, Frishman LJ, et al. (2002). Visual field defects and neural losses from experimental glaucoma. *Prog Retin Eye Res* 21(1): 91-125.

Harwerth RS, Vilupuru AS, Rangaswamy NV, et al. (2007). The relationship between nerve fiber layer and perimetry measurements. *Invest Ophthalmol Vis Sci* 48(2): 763-773.

Harwerth RS (2010). Primate Glaucoma Models. 46: 165-189.

Hayreh S (2011). Pathogenesis of classical non-arteritic anterior ischemic optic neuropathy. *Ischemic Optic Neuropathies*, Springer Berlin Heidelberg: 265-316.

He L, Yang H, Gardiner SK, et al. (2014). Longitudinal detection of optic nerve head changes by spectral domain optical coherence tomography in early experimental glaucoma. *Invest Ophthalmol Vis Sci* 55(1): 574-586.

Heijl A, Bengtsson B, Hyman L, et al. (2009). Natural history of open-angle glaucoma. *Ophthalmology* 116(12): 2271-2276.

Hernandez MR, Andrzejewska WM, Neufeld AH (1990). Changes in the Extracellular-Matrix of the Human Optic-Nerve Head in Primary Open-Angle Glaucoma. *Am J Ophthalmol* 109(2): 180-188.

Hernandez MR, Neufeld AH (1991). The biology of the connective tissue of the human optic nerve head. *Glaucoma Update IV*. G. K. Krieglstein, Springer Berlin Heidelberg: 74-79.

Hernandez MR, Gong H (1996). Extracellular matrix of the trabecular meshwork and optic nerve head*. In: Ritch, R., Shields, M.B., Krupin, T. (Eds), The Glaucomas: Basic Sciences 1*, second ed.(Mosby-Year Book, Inc.): 213-249.

Hernandez MR (2000). The optic nerve head in glaucoma: role of astrocytes in tissue remodeling. *Prog Retin Eye Res* 19(3): 297-321.

Hernandez MR, Miao H, Lukas T (2008). Astrocytes in glaucomatous optic neuropathy. *Prog Brain Res* 173: 353-373.

Hood DC, Zhang X (2000). Multifocal ERG and VEP responses and visual fields: comparing disease-related changes. *Doc Ophthalmol* 100(2-3): 115-137.

Howell GR, Libby RT, Jakobs TC, et al. (2007). Axons of retinal ganglion cells are insulted in the optic nerve early in DBA/2J glaucoma. *J Cell Biol* 179(7): 1523-1537.

Imamura Y, Iida T, Maruko I, Zweifel SA, Spaide RF (2011). Enhanced depth imaging optical coherence tomography of the sclera in dome-shaped macula. *Am J Ophthalmol* 151(2): 297-302.

Inoue R, Hangai M, Kotera Y, et al. (2009). Three-dimensional high-speed optical coherence tomography imaging of lamina cribrosa in glaucoma. *Ophthalmology* 116(2): 214-222.

Ivers KM, Li C, Patel N, et al. (2011). Reproducibility of measuring lamina cribrosa pore geometry in human and nonhuman primates with in vivo adaptive optics imaging. *Invest Ophthalmol Vis Sci* 52(8): 5473-5480.

Jakobs TC, Libby RT, Ben Y, John SW, Masland RH (2005). Retinal ganglion cell degeneration is topological but not cell type specific in DBA/2J mice. *J Cell Biol* 171(2): 313-325.

Johnson EC, Morrison JC, Farrell S, et al. (1996). The effect of chronically elevated intraocular pressure on the rat optic nerve head extracellular matrix. *Exp Eye Res* 62(6): 663-674.

Johnson EC, Deppmeier LM, Wentzien SK, Hsu I, Morrison JC (2000). Chronology of optic nerve head and retinal responses to elevated intraocular pressure. *Invest Ophthalmol Vis Sci* 41(2): 431-442.

Jonas JB, Muller-Bergh JA, Schlotzer-Schrehardt UM, et al. (1990). Histomorphometry of the human optic nerve. *Invest Ophthalmol Vis Sci* 31(4): 736-744.

Jonas JB, Mardin CY, Schlotzer-Schrehardt U, et al. (1991). Morphometry of the human lamina cribrosa surface. *Invest Ophthalmol Vis Sci* 32(2): 401-405.

Jonas JB, Schmidt AM, Muller-Bergh JA, et al. (1992). Human optic nerve fiber count and optic disc size. *Invest Ophthalmol Vis Sci* 33(6): 2012-2018.

Jonas JB, Berenshtein E, Holbach L (2003). Anatomic relationship between lamina cribrosa, intraocular space, and cerebrospinal fluid space. *Invest Ophthalmol Vis Sci* 44(12): 5189-5195.

Kotecha A, Izadi S, Jeffery G (2006). Age-related changes in the thickness of the human lamina cribrosa. *Br J Ophthalmol* 90(12): 1531-1534.

Lampert PW (1967). A comparative electron microscopic study of reactive, degenerating, regenerating, and dystrophic axons. *J Neuropathol Exp Neurol* 26(3): 345-368.

Lee EJ, Kim TW, Weinreb RN, et al. (2012). Three-dimensional evaluation of the lamina cribrosa using spectral-domain optical coherence tomography in glaucoma. *Invest Ophthalmol Vis Sci* 53(1): 198-204.

Leske MC, Connell AM, Wu SY, et al. (2001). Incidence of open-angle glaucoma: the Barbados Eye Studies. The Barbados Eye Studies Group. *Arch Ophthalmol* 119(1): 89-95.

Li C, Sredar N, Ivers KM, Queener H, Porter J (2010a). A correction algorithm to simultaneously control dual deformable mirrors in a woofer-tweeter adaptive optics system. *Opt Express* 18(16): 16671-16684.

Li KY, Tiruveedhula P, Roorda A (2010b). Intersubject variability of foveal cone photoreceptor density in relation to eye length. *Invest Ophthalmol Vis Sci* 51(12): 6858-6867.

Lichter PR, Musch DC, Gillespie BW, et al. (2001). Interim clinical outcomes in the Collaborative Initial Glaucoma Treatment Study comparing initial treatment randomized to medications or surgery. *Ophthalmology* 108(11): 1943-1953.

Luo X, Patel NB, Harwerth RS, et al. (2011). Loss of the low-frequency component of the global-flash multifocal electroretinogram in primate eyes with experimental glaucoma. *Invest Ophthalmol Vis Sci* 52(6): 3792-3804.

Mikelberg FS, Drance SM, Schulzer M, Yidegiligne HM, Weis MM (1989). The normal human optic nerve. Axon count and axon diameter distribution. *Ophthalmology* 96(9): 1325-1328.

Miller KM, Quigley HA (1988). The clinical appearance of the lamina cribrosa as a function of the extent of glaucomatous optic nerve damage. *Ophthalmology* 95(1): 135-138.

Minckler DS, Tso MO, Zimmerman LE (1976). A light microscopic, autoradiographic study of axoplasmic transport in the optic nerve head during ocular hypotony, increased intraocular pressure, and papilledema. *Am J Ophthalmol* 82(5): 741-757.

Minckler DS, Bunt AH, Johanson GW (1977). Orthograde and retrograde axoplasmic transport during acute ocular hypertension in the monkey. *Invest Ophthalmol Vis Sci* 16(5): 426-441.

Minckler DS, Bunt AH, Klock IB (1978). Radioautographic and cytochemical ultrastructural studies of axoplasmic transport in the monkey optic nerve head. *Invest Ophthalmol Vis Sci* 17(1): 33-50.

Minckler DS, Spaeth GL (1981). Optic nerve damage in glaucoma. *Surv Ophthalmol* 26(3): 128-148.

Moran P (1950). Notes on continuous stochastic phenomena. *Biometrika* 37: 17-23.

Mukesh BN, McCarty CA, Rait JL, et al. (2002). Five-year incidence of open-angle glaucoma: the visual impairment project. *Ophthalmology* 109(6): 1047-1051.

Nadler Z, Wang B, Wollstein G, et al. (2013). Automated lamina cribrosa microstructural segmentation in optical coherence tomography scans of healthy and glaucomatous eyes. *Biomed Opt Express* 4(11): 2596-2608.

Neufeld AH, Hernandez MR, Gonzalez M (1997). Nitric oxide synthase in the human glaucomatous optic nerve head. *Arch Ophthalmol* 115(4): 497-503.

Neufeld AH (1999a). Microglia in the optic nerve head and the region of parapapillary chorioretinal atrophy in glaucoma. *Arch Ophthalmol* 117(8): 1050-1056.

Neufeld AH (1999b). Nitric oxide: a potential mediator of retinal ganglion cell damage in glaucoma. *Surv Ophthalmol* 43 Suppl 1: S129-135.

Neufeld AH, Sawada A, Becker B (1999). Inhibition of nitric-oxide synthase 2 by aminoguanidine provides neuroprotection of retinal ganglion cells in a rat model of chronic glaucoma. *Proc Natl Acad Sci* U S A 96(17): 9944-9948.

Nouri-Mahdavi K, Hoffman D, Tannenbaum DP, Law SK, Caprioli J (2004). Identifying early glaucoma with optical coherence tomography. *Am J Ophthalmol* 137(2): 228-235.

Ogden TE, Duggan J, Danley K, Wilcox M, Minckler DS (1988). Morphometry of nerve fiber bundle pores in the optic nerve head of the human. *Exp Eye Res* 46(4): 559-568.

Park HY, Jeon SH, Park CK (2012). Enhanced depth imaging detects lamina cribrosa thickness differences in normal tension glaucoma and primary open-angle glaucoma. *Ophthalmology* 119(1): 10-20.

Pederson JE, Gaasterland DE (1984). Laser-induced primate glaucoma. I. Progression of cupping. *Arch Ophthalmol* 102(11): 1689-1692.

Potts AM, Hodges D, Shelman CB, et al. (1972). Morphology of the primate optic nerve. I. Method and total fiber count. *Invest Ophthalmol* 11(12): 980-988.

Qiao-Grider Y, Hung LF, Kee CS, Ramamirtham R, Smith EL, 3rd (2007). A comparison of refractive development between two subspecies of infant rhesus monkeys (Macaca mulatta). *Vision Res* 47(12): 1668-1681.

Quigley HA, Anderson DR (1976). The dynamics and location of axonal transport blockade by acute intraocular pressure elevation in primate optic nerve. *Invest Ophthalmol* 15(8): 606-616.

Quigley HA, Anderson DR (1977). Distribution of axonal transport blockade by acute intraocular pressure elevation in the primate optic nerve head. *Invest Ophthalmol Vis Sci* 16(7): 640-644.

Quigley HA, Green WR (1979). The histology of human glaucoma cupping and optic nerve damage: clinicopathologic correlation in 21 eyes. *Ophthalmology* 86(10): 1803-1830.

Quigley HA, Guy J, Anderson DR (1979). Blockade of rapid axonal transport. Effect of intraocular pressure elevation in primate optic nerve. *Arch Ophthalmol* 97(3): 525-531.

Quigley HA, Addicks EM (1980). Chronic experimental glaucoma in primates. II. Effect of extended intraocular pressure elevation on optic nerve head and axonal transport. *Invest Ophthalmol Vis Sci* 19(2): 137-152.

Quigley HA, Flower RW, Addicks EM, et al. (1980). The mechanism of optic nerve damage in experimental acute intraocular pressure elevation. *Invest Ophthalmol Vis Sci* 19(5): 505-517.

Quigley HA, Addicks EM (1981). Regional differences in the structure of the lamina cribrosa and their relation to glaucomatous optic nerve damage. *Arch Ophthalmol* 99(1): 137-143.

Quigley HA, Addicks EM, Green WR, et al. (1981). Optic nerve damage in human glaucoma. II. The site of injury and susceptibility to damage. *Arch Ophthalmol* 99(4): 635-649.

Quigley HA, Addicks EM, Green WR (1982). Optic nerve damage in human glaucoma. III. Quantitative correlation of nerve fiber loss and visual field defect in glaucoma, ischemic neuropathy, papilledema, and toxic neuropathy. *Arch Ophthalmol* 100(1): 135-146.

Quigley HA, Hohman RM (1983). Laser energy levels for trabecular meshwork damage in the primate eye. *Invest Ophthalmol Vis Sci* 24(9): 1305-1307.

Quigley HA, Hohman RM, Addicks EM, Massof RW, Green WR (1983). Morphologic changes in the lamina cribrosa correlated with neural loss in open-angle glaucoma. *Am J Ophthalmol* 95(5): 673-691.

Quigley HA, Brown AE, Morrison JD, et al. (1990). The size and shape of the optic disc in normal human eyes. *Arch Ophthalmol* 108(1): 51-57.

Quigley HA, West SK, Rodriguez J, et al. (2001). The prevalence of glaucoma in a population-based study of Hispanic subjects: Proyecto VER. *Arch Ophthalmol* 119(12): 1819-1826.

Quigley HA (2005). New paradigms in the mechanisms and management of glaucoma. *Eye* (Lond) 19(12): 1241-1248.

Quigley HA, Broman AT (2006). The number of people with glaucoma worldwide in 2010 and 2020. *Br J Ophthalmol* 90(3): 262-267.

Quigley HA (2011). Glaucoma. *The Lancet* 377(9774): 1367-1377.

Rajagopalan LP, Patel NB, Harwerth RS, et al. (2013). Loss of the photopic negative response of the multifocal electroretinogram in a nonhuman primate model of experimental glaucoma. *J Vision* 13(15): P37.

Rangaswamy NV, Zhou W, Harwerth RS, et al. (2006). Effect of experimental glaucoma in primates on oscillatory potentials of the slow-sequence mfERG. *Invest Ophthalmol Vis Sci* 47(2): 753-767.

Resnikoff S, Pascolini D, Etya'ale D, et al. (2004). Global data on visual impairment in the year 2002. *Bull World Health Organ* 82(11): 844-851.

Roberts MD, Grau V, Grimm J, et al. (2009). Remodeling of the connective tissue microarchitecture of the lamina cribrosa in early experimental glaucoma. *Invest Ophthalmol Vis Sci* 50(2): 681-690.

Roberts MD, Liang Y, Sigal IA, et al. (2010). Correlation between Local Stress and Strain and Lamina Cribrosa Connective Tissue Volume Fraction in Normal Monkey Eyes. *Invest Ophthalmol Vis Sci* 51(1): 295-307.

Romero-Borja F, Venkateswaran K, Roorda A, et al. (2005). Optical slicing of human retinal tissue in vivo with the adaptive optics scanning laser ophthalmoscope. *Appl Opt* 44(19): 4032-4040.

Sanchez RM, Dunkelberger GR, Quigley HA (1986). The number and diameter distribution of axons in the monkey optic nerve. *Invest Ophthalmol Vis Sci* 27(9): 1342-1350.

Schlamp CL, Li Y, Dietz JA, Janssen KT, Nickells RW (2006). Progressive ganglion cell loss and optic nerve degeneration in DBA/2J mice is variable and asymmetric. *BMC Neurosci* 7: 66.

Schuman JS, Hee MR, Arya AV, et al. (1995). Optical coherence tomography: a new tool for glaucoma diagnosis. *Curr Opin Ophthalmol* 6(2): 89-95.

Shrout PE, Fleiss JL (1979). Intraclass correlations: uses in assessing rater reliability. *Psychol Bull* 86(2): 420-428.

Sigal IA, Flanagan JG, Tertinegg I, et al. (2004). Finite element modeling of optic nerve head biomechanics. *Invest Ophthalmol Vis Sci* 45(12): 4378-4387.

Sihota R, Sony P, Gupta V, Dada T, Singh R (2006). Diagnostic capability of optical coherence tomography in evaluating the degree of glaucomatous retinal nerve fiber damage. *Invest Ophthalmol Vis Sci* 47(5): 2006-2010.

Spaide RF, Koizumi H, Pozzoni MC (2008). Enhanced depth imaging spectral-domain optical coherence tomography. *Am J Ophthalmol* 146(4): 496-500.

Sredar N, Ivers KM, Queener HM, Zouridakis G, Porter J (2013). 3D modeling to characterize lamina cribrosa surface and pore geometries using in vivo images from normal and glaucomatous eyes. *Biomed Opt Express* 4(7): 1153-1165.

Strouthidis NG, Grimm J, Williams GA, et al. (2010). A comparison of optic nerve head morphology viewed by spectral domain optical coherence tomography and by serial histology. *Invest Ophthalmol Vis Sci* 51(3): 1464-1474.

Strouthidis NG, Fortune B, Yang H, Sigal IA, Burgoyne CF (2011a). Effect of acute intraocular pressure elevation on the monkey optic nerve head as detected by spectral domain optical coherence tomography. *Invest Ophthalmol Vis Sci* 52(13): 9431-9437.

Strouthidis NG, Fortune B, Yang H, Sigal IA, Burgoyne CF (2011b). Longitudinal change detected by spectral domain optical coherence tomography in the optic nerve head and peripapillary retina in experimental glaucoma. *Invest Ophthalmol Vis Sci* 52(3): 1206-1219.

Susanna R, Jr. (1983). The lamina cribrosa and visual field defects in open-angle glaucoma. *Can J Ophthalmol* 18(3): 124-126.

Tezel G, Trinkaus K, Wax MB (2004). Alterations in the morphology of lamina cribrosa pores in glaucomatous eyes. *Br J Ophthalmol* 88(2): 251-256.

Torti C, Povazay B, Hofer B, et al. (2009). Adaptive optics optical coherence tomography at 120,000 depth scans/s for non-invasive cellular phenotyping of the living human retina. *Opt Express* 17(22): 19382-19400.

Trivino A, Ramirez JM, Salazar JJ, Ramirez AI, Garcia-Sanchez J (1996). Immunohistochemical study of human optic nerve head astroglia. *Vision Res* 36(14): 2015-2028.

Vilupuru AS, Rangaswamy NV, Frishman LJ, et al. (2007). Adaptive optics scanning laser ophthalmoscopy for in vivo imaging of lamina cribrosa. *J Opt Soc Am A Opt Image Sci Vis* 24(5): 1417-1425.

Viswanathan S, Frishman LJ, Robson JG, Harwerth RS, Smith EL, 3rd (1999). The photopic negative response of the macaque electroretinogram: reduction by experimental glaucoma. *Invest Ophthalmol Vis Sci* 40(6): 1124-1136.

Viswanathan S, Frishman LJ, Robson JG, et al. (2001). The photopic negative response of the flash electroretinogram in primary open angle glaucoma. *Invest Ophthalmol Vis Sci* 42(2): 514-522.

Walsh MK, Quigley HA (2008). In vivo time-lapse fluorescence imaging of individual retinal ganglion cells in mice. *J Neurosci Methods* 169(1): 214-221.

Wang B, Nevins JE, Nadler Z, et al. (2013). In vivo lamina cribrosa micro-architecture in healthy and glaucomatous eyes as assessed by optical coherence tomography. *Invest Ophthalmol Vis Sci* 54(13): 8270-8274.

Wollstein G, Schuman JS, Price LL, et al. (2005). Optical coherence tomography longitudinal evaluation of retinal nerve fiber layer thickness in glaucoma. *Arch Ophthalmol* 123(4): 464-470.

Yang H, Downs JC, Bellezza A, Thompson H, Burgoyne CF (2007a). 3-D histomorphometry of the normal and early glaucomatous monkey optic nerve head: prelaminar neural tissues and cupping. *Invest Ophthalmol Vis Sci* 48(11): 5068-5084.

Yang H, Downs JC, Girkin C, et al. (2007b). 3-D histomorphometry of the normal and early glaucomatous monkey optic nerve head: lamina cribrosa and peripapillary scleral position and thickness. *Invest Ophthalmol Vis Sci* 48(10): 4597-4607.

Yang H, Downs JC, Burgoyne CF (2009). Physiologic intereye differences in monkey optic nerve head architecture and their relation to changes in early experimental glaucoma. *Invest Ophthalmol Vis Sci* 50(1): 224-234.

Yang H, Thompson H, Roberts MD, et al. (2011). Deformation of the early glaucomatous monkey optic nerve head connective tissue after acute IOP elevation in 3-D histomorphometric reconstructions. *Invest Ophthalmol Vis Sci* 52(1): 345-363.

Yang H, Qi J, Hardin C, et al. (2012). Spectral-domain optical coherence tomography enhanced depth imaging of the normal and glaucomatous nonhuman primate optic nerve head. *Invest Ophthalmol Vis Sci* 53(1): 394-405.

Zawadzki RJ, Choi SS, Fuller AR, et al. (2009). Cellular resolution volumetric in vivo retinal imaging with adaptive optics-optical coherence tomography. *Opt Express* 17(5): 4084-4094.